PHYSICAL MECHANISMS OF LASER-ACTIVATED NANOPARTICLES FOR INTRACELLULAR DRUG DELIVERY

A Dissertation
Presented to
The Academic Faculty

by

Stefany Y. Holguin

In Partial Fulfillment
of the Requirements for the Degree
Doctor of Philosophy in the
School of Materials Science and Engineering

Georgia Institute of Technology
August 2017

PHYSICAL MECHANISMS OF LASER-ACTIVATED NANOPARTICLES FOR INTRACELLULAR DRUG DELIVERY

Approved by:

Dr. Mark R. Prausnitz, Advisor
School of Chemical and Biomolecular Engineering
Georgia Institute of Technology

Dr. David Bucknall
School of Materials Science and Engineering
Georgia Institute of Technology

Dr. Naresh N. Thadhani, Advisor
School of Materials Science and Engineering
Georgia Institute of Technology

Dr. Michelle LaPlaca
Wallace H. Coulter Department of Biomedical Engineering
Georgia Institute of Technology

Dr. Valeria Milam
School of Materials Science and Engineering
Georgia Institute of Technology

Dr. Michael D. Gray
The Institute of Biomedical Engineering
University of Oxford

Date Approved: April 27, 2017

To Lita Edelfida and Lita Norma – your sacrifices made this possible

ACKNOWLEDGEMENTS

Completing a PhD is only possible with the support of family, friends, mentors, and advisors. First, I want to extend my deepest love and appreciation to my parents. Growing up as a military child taught me resilience and adaptability to change – all qualities which I had to continually revisit during my pursuit of the PhD. To my father – thanks for taking me as a child to the lab during your night shifts and letting me organize pipette tips. Your desire to help others has inspired me in numerous ways. To my mother – thank you for always instilling the value of education in Kris and I, and for being one of our biggest advocates. Thank you for pushing me to always strive for excellence. To my younger (funnier sibling), Kris – you will always be my baby brother. Thanks for the much-needed comic relief sometimes and more light-hearted approach to life.

Next, thank you to my research advisors Prof Mark Prausnitz and Prof Naresh Thadhani. Thanks for the opportunity to engage in truly interdisciplinary research. Existing in-between disciplines pushed me out of my comfort zone and stretched my intellectual capabilities far beyond what I could ever imagine. Thank you for your professionalism, feedback and latitude to develop as an independent researcher. Throughout the years, I've picked up on many leadership lessons from the both of you and will take them with me as transition from student to professional.

Thanks also to my committee members – Prof Valeria Milam, Prof Michelle LaPlaca, Prof David Bucknall and Dr. Michael Gray for your feedback. Mike – it's been great to collaborate with someone who cares as deeply about quality research as much as I do. I'm also grateful for the funding support and intangible opportunities from the NSF

Graduate Research Fellowship, the Goizueta Foundation Fellowship, the NIH BioMat training grant and the Georgia Tech UCEM & Sloan Foundation Fellowship.

Being co-advised means you have two lab 'families'. Thanks to everyone from the Drug Delivery Lab for a fun, friendly work environment. First, to the "quad". Monica, I will always appreciate your friendship and conversation. Thanks for the discussions ranging from philosophy to economics to celebrity gossip to feminism. Most of all, thanks for being one of the most genuine friends I've had and for your unconditional support. [secret code: haiku]. Pradnya – I will miss our inside jokes and labeling everything on your desk (*yes, sometimes it was me, not Josh*). Dr. Bryce Chiang, thanks for all the laughs and perspective on research and writing. The cat pictures will live on. Simple, thanks for being a kind, receptive mentee and colleague. I hope that I've taught you something worthwhile. Dr. Seonhee Park, thanks for tolerating my Spongebob SquarePants jokes and for the numerous Korean food outings and for your patience in the cell culture room. Dr. Wilmarie Medina-Ramos, thanks for being a sounding board and a good friend. Donna Bondy, thanks for all the laughs, discussion about fitness (body pump, yoga, muay thai) and all the delicious chocolate cookies. A sincere thanks to the other #PrausSquad members (including, but not limited to Dr. Jaya Arya, Dr. Matt Mistilis, Jessica Joyce, Andrew Tadros, Josh Palacios, Dr. Jae Hwan Jung). Thanks to the undergraduate students who assisted me with experiments – Princeton Joseph, Jonathan Lin, and Caleb Anderson. Thanks to the others I mentored – Giovanni King (GT SURE program) and Madison Hecht. All of you made me be a better leader and mentor.

To my other lab family, the Thadhani Lab. Thank you Dr. Jennifer Breidenich for your encouragement and guidance in the first few years of my PhD. I don't miss the random

silverfish in the office, but I do miss derping with you. Dr. Rene Diaz – thanks for your insight and perspective especially when things seemed daunting. You taught me the importance of being more kind and giving to others. Thanks to Alex Bryant and David Scripka, for your friendship, late Friday evening political discussions, Dave & Buster's outings and just general comradery. I will miss that, but we still have the Gchat group! Thanks to the other past and present members as well (Dr. Sean Kelly, Dr. Paul Specht, and many others).

To the Sloans – Dr. Michelle Collins, Dr. Daniel Largo, Dr. Yancy Diaz, Dr. Sergio Garcia, Dr. Sunni Ivy, Denise Sullivan, and Jada Selma – we did it! Thanks for all the laughs (BOP IT!) during the Teaching & Mentoring Institute, Walking Dead gatherings, dinner outings and general support and encouragement. I know we will continue to lift and support each other as we continue our paths after grad school. Denise and Jada – the J. Cole concert, the SuperBowl (I still can't believe the Falcons blew that lead), the movies, etc. there were so many fun experiences and times we've shared. Thanks for always being willing to engage in discussion about sociology, Beyoncé, intersectional feminism and the continued underrepresentation of people of color and more specifically women of color in STEM.

To my GT MSE friends – Judy Dickson, Brian Doyle, Alex Bryant, and Dan Gordon. We didn't see each other nearly as often as we should have, but every time we did it was a ball. Thanks for the quals celebrations, birthday gatherings, holiday potlucks, debate & election watch nights, brunches and other outings these past 5 years. It was a blast and I'm glad to have grown in the PhD program alongside all of you. Alex and Brian – it's crazy to think I've known you both since 2012 back when we were still choosing graduate

schools. I'm glad we all came to Georgia Tech and were involved in GSAG and other organizations. It's always reassuring to know someone else cares about improving the lives of other graduate students.

To my other close friends who made this process more bearable -- Sean Rodrigues and Dr. Lizzette Gomez-Ramos. Sean, who would have thought back in 2011 at the Northwestern REU that we'd be at Georgia Tech together for our PhDs? Thanks for listening to me rant, getting bibimbap with me, and just letting me exist. I will always cherish our friendship and I fiercely admire your dedication to outreach and love of scholarship. I know you're going to be a great professor one day. Dr. Lizzette Gomez-Ramos – you always make me laugh (unintentionally), but in all seriousness thanks for accepting this person of Puerto Rican-descent with my sometimes-tongue-tied Spanish. I deeply respect your work ethic.

I'd also like to acknowledge the numerous mentors during my PhD: Dr. Rebekah Neal, Dr. CJ Stanfill, Dr. Annie Gutsche, Prof Michele Manuel, and Prof Jenny Andrew. Thanks for all the encouragement these past 5 years and for recognizing my potential. I deeply appreciate the different perspectives and guidance as a graduate student and your investment in my development not only as a researcher, but also as a human being. Thank you to others at Georgia Tech who were also willing to take time out of their schedules to chat and muse about my life and career – Prof Ayanna Howard, Prof Stephen Ruffin, Prof Tequila Harris, Michelle Wong, Kathleen Kurre, and Dr. Michelle Lyn. Thank you also to Dr. Liz Boylan from the Sloan Foundation for meeting with me in NYC in Summer 2016. I'm very grateful for your perspective on life and your long successful career.

Thank you to the many public-school teachers who also molded me and provided opportunities that catalyzed my love for learning – Mr. Nordstorm for encouraging me to apply to the University of Washington Bioengineering Summer Camp, Mr. Nelson for providing a 6th grader with deep understanding of what it means to be a well-rounded scholar, and Mr. Schell for helping me develop critical thinking skills. Thank you to the many other teachers and educators who impacted my life.

Bot, thanks for all your love and encouragement. You were always a reassuring voice and guiding light throughout these past 5 years. There are not enough words and I'm not sure I'd even know how to begin to describe how much your support has meant to me. It's crazy to reflect on how much we've grown together, despite all the *kilometros* that separated us at times. Thanks for partaking in some of the most challenging and enriching years of my young adult life. *Te quiero.*

I'd be remiss if I didn't recognize my impact with the completion of this degree. I once attended a conference with the greatest gathering of Latinx and Black PhD students in the country. One of the speakers said something that has stuck with me – as we climb the ladder of education into the higher spheres, let us always remember to look back and extend a hand to others. I cannot ignore the impact of being a female Latina/Hispanic engineer in STEM. This PhD is as much mine as it those who are underrepresented in STEM and beyond. With each PhD, we are one step closer to tomorrow's promise of diversity and equality for all.

Finally, to my *litas* (grandmothers) Norma Gandía Rosa and Edelfida West – none of this would have been possible without your sacrifice. The immigrant story is one of the young woman who leaves Puerto Rico and works in a factory in Yonkers for $1.75 an hour. The immigrant story is one of the woman who leaves the Dominican Republic as a single mother and goes to Puerto Rico, then Miami, Florida to work as a housekeeper, and finally to NYC to provide a better life for her three children. You embody the blazing fire of resilience and determination that I carry with me every day. In many ways, your sacrifices enabled my past, present, and future successes. Your story is the American Dream embodied. "*I am my ancestors' wildest dreams."* I am the American Dream.

Forward.

TABLE OF CONTENTS

LIST OF TABLES

LIST OF FIGURES

LIST OF ABBREVIATIONS

BSA	bovine serum albumin
CB	carbon black
CMC	carboxyl methylcellulose
FBS	fetal bovine serum
IR	infrared
Jasplak	jasplakinolide
LatA	latrunculin A
LSPR	localized surface plasmon resonance
MβCD	methyl-β-cyclodextran
MWCNT	multi-walled carbon nanotubes
NIR	near-infrared
PBS	phosphate buffer saline
PI	propidium iodide
SWCNT	single-walled carbon nanotubes
TNET	transient nanoparticle energy transduction
WSC	water-soluble cholesterol

SUMMARY

Novel intracellular drug delivery techniques are needed to overcome the barrier of the cell's plasma membrane. Since the cell membrane is highly selective, it is difficult for potential therapeutics, like those for gene-based therapy and other active molecules to enter the cytosol by methods other than active transport. To bypass the membrane, physical drug delivery methods can be employed to create transient openings in the membrane that enable the passive transport of molecules. Optimizing physical methods is often challenging due to a need to balance molecular delivery and high cell viability. A novel, laser-mediated technique known as transient nanoparticle energy transduction (TNET) has been shown to successfully balance these two parameters. When carbon black (CB) nanoparticles in suspension with cells and small molecules are irradiated by nanosecond-pulsed near infrared (NIR) laser energy, efficacious delivery while maintaining high cell viability are achieved.

This novel drug delivery platform is driven by the laser-activation of CB nanoparticles and the subsequent energy transduction which induces bioeffects (i.e., uptake and viability loss). Upon NIR absorption, the CB nanoparticles rapidly heat up to hundreds of degrees Celsius and undergo thermal expansion. This rapid heating leads to vaporization of surrounding water, which creates vapor-bubbles that transfer heat and pressure to nearby cells. To gain mechanistic insight into TNET, we studied various aspects of this *in vitro* system, including cellular mechanics, cell-CB nanoparticle interaction, and the role of photoacoustics.

First, we studied the role of cellular mechanics in TNET by way of the cytoskeleton and plasma membrane fluidity. Destabilizing the cytoskeleton of DU145 cells caused greater intracellular uptake and lower viability loss compared to cells with intact cytoskeletons. Additional studies showed that altering the fluidity of the membrane had no significant effect on bioeffects. From these studies, we concluded that cytoskeletal mechanics are integral to resulting bioeffects achieved with TNET, whereas the fluidity of the plasma membrane is not.

Next, we studied the effect of energy input into the system, which was increased by increasing laser fluence, CB nanoparticle concentration and number of laser pulses. We found that at low energy, intracellular uptake increased with increasing energy input. At higher energy, cell viability loss of DU145 cells increased and viable cells with intracellular uptake decreased. At the highest energy inputs, cell fragmentation increased, while intracellular uptake and loss of viability decreased. Increasing cell concentration had the opposite effect (i.e., it reduced the intensity of bioeffects), which suggests that neighboring cells shielded each other from the effects of TNET. Increasing medium viscosity also decreased the intensity of bioeffects, suggesting a mechanical (i.e., not thermal) cause of bioeffects.

Finally, we studied the effects of three different carbon-based nanoparticles – CB, multi-walled carbon nanotubes (MWCNT) and single-walled (SWCNT) carbon nanotubes – on DU145 cellular bioeffects. As mentioned above, increasing energy input with CB nanoparticles progressed through increasing intracellular uptake, followed by increasing cell viability loss, which was followed by increasing cell fragmentation. For MWCNT, increasing energy input first increased intracellular uptake and then increased cell

fragmentation, but did not cause cell viability loss. For SWCNT, no significant bioeffects were seen, except at extreme conditions where cell viability loss was seen. The intensity of photoacoustic output in the form of a single, mostly positive-pressure pulse of ~100 ns duration varied among the different types of nanoparticles, where SWCNT had the highest peak pressure, followed by CB and then by MWCNT. Lack of a universal correlation between peak pressure and cellular bioeffects, suggested that total energy input rather than pressure output was more mechanistically relevant to TNET.

Overall, this work provides functional characterization and mechanistic understanding the cellular bioeffects cause by TNET. These studies will contribute an understanding of TNET that will enable rational design of TNET systems for future applications and possible translation into the clinic.

CHAPTER 1. INTRODUCTION

Drug delivery research seeks to address the challenges of increasing healthcare costs and a growing need for novel therapies to treat complex diseases [1], [2]. Molecules such as proteins, nanocarriers, and plasmids are potentially revolutionary forms of therapies. Yet, for these treatments to be effective, they must be delivered into the cytoplasm or the nucleus [3]–[5]. The lipophilic nature of the cell membrane, however, is a delivery barrier for these molecules. The cell membrane resists the delivery of large or polar molecules across the membrane and into the cytosol by processes other than active transport (e.g. endocytosis) [6], [7]. Endocytosis is a process in which the cell engulfs external molecules. Due to changes in pH and other degradative processes, this process can cause degradation of the drug molecule or release of the comprised drug into the cytoplasm, which can face further obstacles with cytoplasm trafficking and access to the nucleus [8].

Drug delivery researchers employ a number of techniques to overcome the cell membrane barrier. These methods can be divided broadly into biological, chemical, and physical drug delivery methods, all which have varying advantages and drawbacks. Briefly, biological and chemical methods can be disadvantageous due to issues with cytotoxicity [9]–[12] and delivery processes mediated by endocytosis [8]. In contrast, physical methods bypass the endocytic pathway by applying physical forces to the cell membrane and create transient openings which drive molecules into the cytosol.

Physical drug delivery methods include electroporation, microinjection, ultrasound, and laser-mediated methods. These methods are advantageous because they can be applied generically to different types of cells and tissue systems. Yet, a major drawback associated

with physical methods is balancing molecular delivery and cell viability. Forces applied to the cell can cause irreversible damage and result in viability loss. Thus, truly effective physical methods attain high intracellular delivery and high cell viability. This work uses a novel laser-mediated method which achieves efficacious drug delivery with laser-activated carbon nanoparticles.

When carbon black (CB) nanoparticles in suspension with cancer cells and small molecules are irradiated by nanosecond pulsed, near-infrared (NIR) laser energy, high cellular uptake and high viability can be achieved [13], [14]. This approach was inspired by Chen and Diebold's [15] studies of laser-irradiated CB nanoparticles which produced a "giant photoacoustic effect." The photoacoustic effect was caused by rapid particle heating, thermal expansion and generation of vapor bubbles due to a carbon-steam reaction with the surrounding liquid [15]. Laser-mediated delivery with CB nanoparticles was a departure from previous work with ultrasound drug delivery, where it was difficult to achieve effective delivery, while minimizing viability loss [16]–[22].

First, Chakravarty [13] used femtosecond and nanosecond laser pulses to deliver molecules such as dextran and bovine serum albumin intracellularly, and hypothesized that intracellular delivery was driven by Diebold's observed photoacoustic effect and the carbon-steam reaction [15] . Later efforts by Sengupta [23] discovered that the chemical reaction was not the primary driver for observed bioeffects. They hypothesized that observed bioeffects were due to an acoustic and/or thermal mechanism because of rapid vapor bubble formation and expansion on the timescale of the nanosecond pulse. It was postulated that these combined energy mechanisms, phenomena known as transient

nanoparticle energy transduction (TNET), were responsible for high molecular delivery and high cell viability.

The aforementioned work provided an important foundation to understand energy transfer from the particle to the cell. Sengupta's work [23] concluded that neither the thermal expansion of the particle nor long-range acoustics were mechanistically responsible for TNET [23]. Instead, it was proposed that short-range interactions due to cell – particle interaction caused the observed bioeffects of TNET. In turn, this dissertation builds on that prior work and seeks to provide a more thorough biophysical basis for TNET and its effects on cells.

The first part of this study focused on understanding the role of a cell's mechanical integrity due to TNET. In this work, we explored cytoskeletal mechanics and cell membrane fluidity by altering their proprieties and then testing the resulting bioeffects (i.e. intracellular uptake and viability) with *in vitro* exposures. Actin filaments in the cytoskeleton were weakened with Latrunculin A and rigidified using Jasplakinolide. Cell membrane fluidity was increased with methyl-β-cyclodextrin and decreased with water-soluble cholesterol.

The second part of this work tested various parameters which facilitate short-range cell-CB nanoparticle interaction, while elucidating their mechanistic implications for TNET. The effect of total energy input on this interaction was studied by evaluating the effects of laser pulse, fluence, CB nanoparticle concentration, cell concentration and medium viscosity.

Lastly, we investigated the long-range effects of acoustically active carbon nanoparticles and the resulting cumulative pressure-field. In this study, we attempted to

separate bioeffects from the influence of the nanoparticle. First, we measured the cumulative pressure profiles of three carbon particle systems – CB, single-walled carbon nanotubes (SWCNT), and multi-walled carbon nanotubes (MWCNT). Then, to determine if bioeffects correlate with long-range acoustic output, we tested the three particle systems *in vitro* and quantified the resulting bioeffects (i.e. uptake and viability).

The overall aim of this dissertation is to provide a fundamental mechanistic understanding of energy transductions in TNET that impact cells. This will enable a more rational approach in future optimization of this platform that will be necessary before translating TNET for laboratory applications, *in vivo* and eventually into the clinic.

CHAPTER 2. BACKGROUND

Innovative drug delivery research is necessary to treat complex diseases [2], [24]. Specific targeting of drugs is challenging due to the cell membrane. The cell membrane resists polar molecules and prevents the diffusion of large molecules across the membrane [7]. Researchers including scientists, engineers, clinicians, and pharmacists are developing techniques that will effectively deliver the active substance to highly targeted sites [4], [5]. Revolutionary gene therapy via siRNA and mRNA [8], [25], in addition to innovative active substances [26] are potentially more potent therapies if they reach the cytosol. Thus, targeting of drugs into cells is essential for the advancement of not only drug delivery, but more broadly for the advancement of human health.

2.1 Transport mechanisms to cross the plasma membrane barrier

2.1.1 Passive transport mechanisms

Phospholipids compose the cell membrane and provide a barrier between the cell and its external environment (**Figure 2.1**). The phospholipids contain polar head groups and fatty acid tails which facilitate transport of ions and molecules across the membrane. Selective permeability of the cell membrane is a result of the tightly packed phospholipids and the hydrophobic interior (i.e. due to fatty acid tails). Thus, only select molecules can move freely across the membrane without energy expenditure of the cell. Molecules that are small, nonpolar, and uncharged can cross the membrane via passive transport. Passive transport can be designated into three categories – (i) diffusion, (ii) facilitated diffusion, and (iii) osmosis.

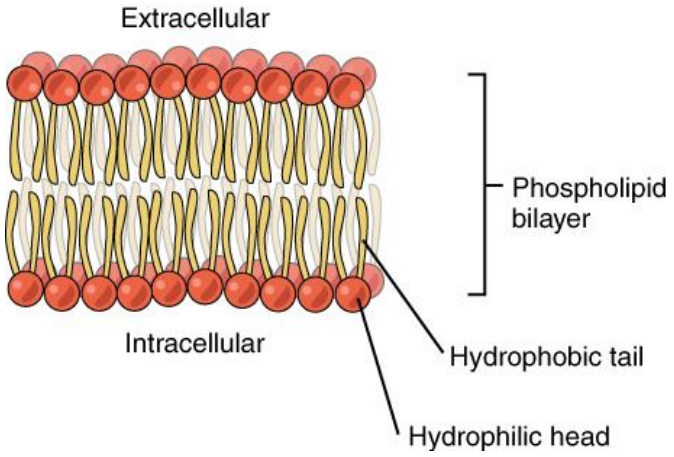

Figure 2.1: Schematic of lipid bilayer showing components of phospholipids that are present in the cell membrane. Adapted from [27].

Diffusion allows small molecules like O2 can freely pass through small holes in cell membrane surface. Diffusion is simply the movement of molecules or particles due to a concentration gradient in an energetically more favorable direction [28]. Charged, polar, or larger molecules cannot pass through the membrane by simple diffusion. Facilitated diffusion transports these types of molecules by transmembrane proteins consisting of channel proteins and carrier proteins. Channel proteins form small pores regulated by the cell's response to external stimuli and allow ions like Ca^{2+} and K^{+} to diffuse across the cell membrane [28]. Molecules that cannot cross due to size or polarity, like glucose are transported by carrier proteins. Carrier proteins are activated when water-soluble molecules like glucose selectively bind to the protein, change its confirmation and results in the transport of the molecule from the external surface to the cell interior. Finally, osmosis is the process in which molecules in water freely diffuse in and out of the cell, regulated by the water potential exerted on the membrane.

2.1.2 Active transport mechanisms

If a molecule must cross the cell membrane against the concentration gradient, the cell must expend energy in the process, which is known as active transport. The cell uses transmembrane proteins or the cell membrane for active transport mechanisms. Transmembrane proteins are used in the sodium-potassium pump (i.e. Na^+/K^+ ATPase), where the cell transports sodium out of the cell and moves potassium into the cell to maintain an electrical gradient across the cell membrane [28]. Active transport can also occur without the assistance of transmembrane proteins (e.g. endocytosis).

Endocytosis is an active transport mechanism for intracellular uptake of molecules that cannot cross the membrane due to size, charge and/or polarity. Endocytosis occurs when the cell membrane extends itself, engulfs external molecules, and pinches that part of the membrane off into a vesicle. For general uptake of molecules, the cell can use phagocytosis or pinocytosis to bring external molecules to its interior. Phagocytosis engulfs large molecules and is commonly used by immune cells such as macrophages, which actively engulf foreign matter in tissues [29]. Pinocytosis, unlike phagocytosis, engulfs external fluid containing dissolved molecules for transport into the cell [29]. For more selective intracellular uptake, the cell can employ receptor-mediated endocytosis. In receptor-mediated endocytosis, receptors must bind to a specific surface ligand before the cell endocytoses the receptor-ligand complexes [29].

2.2 **Intracellular delivery techniques addressing challenge of intracellular targeting**

The inherent structure of the cell poses challenges for intracellular targeting of therapeutics. Because the cell membrane is highly selective, most drug molecules of interest, ranging from small molecules to larger molecules such as DNA and RNA, are not

able to pass through the membrane through passive processes. To overcome the plasma membrane, various drug delivery techniques have been developed which either (i) harness the cell's active transport mechanisms or (ii) disrupt the cell membrane to enable passive transport of molecules.

Chemical and biological drug delivery methods harness endocytosis to deliver therapeutics intracellularly [30]. Chemical methods modify a drug to assist crossing the membrane, whereas biological drug delivery methods (i.e. viruses) use the machinery of the virus to cross the cell membrane. However, a major drawback of endocytosis is possible lysosomal degradation that can occur in the endocytic pathway [8]. In the endocytic pathway, endosomes expose the drug to low pH and can irreversibly damage the drug.

In contrast, physical methods bypass active transport methods by breaking holes in the cell membrane to enable passive transport of molecules into the cell [31]. By creating transient pores in the membrane, the drug can cross the cell membrane through passive transport and bypass potential degradation from the endocytotic pathway.

The following section will review more in detail the three major delivery techniques – chemical, biological and physical, which are used to target therapies intracellularly.

2.2.1 Chemical methods

Chemical methods are used to modify a drug and improve its overall stability. Encapsulation of the drug can assist in crossing the plasma membrane by active transport for delivery into the cytosol. Several approaches to encapsulate a drug include polymer micro/nano capsules made by layer-by-layer assembly [4], [24], [32], [33], hydrogels [4],

[24], peptides with nanoparticles [4], [34], and cationic lipids. These approaches can increase the precision of targeting and may improve release profiles of the drug [4].

Nanoparticles and cationic lipids have different capabilities dependent on their design. Nanoparticle design can vary based on the material, ranging from inorganic materials [35] to polymers [36] (i.e. liposomes [37], dendrimers [38]), and nanocrystals [39]. These materials allow for multifunctional targeting and sometimes imaging capabilities [35]. Cationic lipids can be assembled into liposomes [12], [40] which facilitate endocytic uptake and escape. Cationic lipids can disrupt the cell membrane via electrostatic interactions with membrane phospholipids [10], [41]. Chemical techniques pose a variety of disadvantages, due to stability, clearance, toxicity [10]–[12], and lysosomal degradation [8].

2.2.2 Biological methods

Biological methods include areas of gene delivery, specifically viral vectors that express transgenes for therapy. There are several types of vectors used for biological methods –retroviruses, lentiviruses, and adenoviruses [9]. Virus particles can be used for DNA and RNA delivery, in which viral vectors infect cells and then replicate their viral genome to induce gene expression [9], [42]. While viral vectors hold great promise for therapy, there are rampant issues with immune matching and excessive costs associated with this method of drug delivery [9]. Like chemical methods, these biological methods promote endocytotic uptake, and thus have issues with intracellular delivery since it is mediated by the endocytotic pathway.

2.2.3 Physical methods

Biophysical methods leverage physical stresses to disrupt the cell membrane and drive drug molecules across the membrane. Physical methods are particularly advantageous because they bypass the membrane, avoid the endocytotic pathway, and provide a clear pathway for targeting the cytosol [31], [43]. However, there are also substantial challenges associated with physical methods. The challenge is to control the magnitude of physical stress imparted onto the cell while balancing intracellular delivery and cell viability. These stresses which create transient openings or pores, can sometimes lead to cell death if the pores cannot reseal and/or the cell cannot recover from the stress.

Pores created by physical disruption of the membrane can be characterized according to their spatial and temporal response. Transient pores and pores that exist beyond the transient timeframe can trigger the onset of apoptosis or necrosis [19]. However, pores that can repair themselves, may be able to retain the cells' viability. More specifically, pores that are unstable and reseal themselves exist on a short time span and are very small (i.e. 1 nm). In contrast, pores that are open longer and are larger (i.e. 10 – 100 nm), require active resealing by the cell. To patch these larger pores, the cell uses active cellular process to 'patch-up' wounds in the membrane. For example, pores on this scale are observed in ultrasound drug delivery research due to violent cavitation events [21], [22], [44]. Pores that are 1 – 10 nm are often metastable and undergo passive resealing. This scenario arises due to an increase in free energy when water enters the pores and interacts with the hydrophobic tail interior region of the membrane. Because this interaction is unfavorable, the lipids passively reshape themselves to minimize free energy [45]. These types of pores have been studied extensively in electroporation mediated methods and have been shown to exist on the timescale of milliseconds [46]–[48].

Nevertheless, different biophysical methods can result in pores with the aforementioned characteristics. Relevant physical methods which create these types of pores include electroporation, ultrasound, microinjection, and laser-assisted delivery.

2.2.3.1 Electroporation

Electroporation is a popular biophysical technique used for cell transfection. Electroporation occurs when a short, high-voltage pulse is applied to a cell and the resulting electric field leads to membrane disruption [47]. The disruption creates pores that enable the delivery of molecules across the membrane. This method has successfully delivered a wide range of molecules, e.g. DNA, and proteins [47], and has shown promise with *in vitro* and *in vivo* methods [49], [50]. However, electroporation can be challenging to translate due to empirical optimization that is cell type dependent and in need for invasive electrodes for application to tissues [47].

2.2.3.2 Ultrasound

Ultrasound has been used to deliver genetic materials and chemotherapies into cells by means of acoustic cavitation to mechanically disrupt cell membranes [18], [19], [22]. Cavitation occurs when a bubble collapses and the subsequent release of acoustic energy with compressive and tensile stresses [18] mechanically interact with the cell membrane. Other studies have shown that stable bubble oscillation also works effectively [51]. Ultrasound has proved effective for intracellular delivery [18], [22] and can be combined with microbubbles to improve efficacy of delivery. Yet, there are a number of disadvantages associated with ultrasonic delivery methods. The effects of ultrasound ultimately depend on the amount of acoustic energy released, which in some cases can

cause excessive damage to cells and result in significant cell death. Additionally, the polydispersity of cavitation agents makes ultrasound makes process control very difficult.

2.2.3.3 Microinjection

Essentially any type of molecule can be delivered into cells with microinjection. Microinjection occurs when a glass needle is inserted into a cell and the molecules of interest are directly delivered into the cytosol [52]. This method is advantageous since there is direct control of the amount of therapy delivered into the cells. Still, microinjection is limited by its inherent mechanism – it is only optimal for single cell delivery. Physical injury and cell viability are also drawbacks associated with microinjection [52].

2.2.3.4 Laser-mediated delivery

Engineer and physicist, Theodore Maiman developed the first working laser in 1960 [53]. A year later, dermatologist Leon Goldman was the first to translate laser technology into medicine [54], [55], using a laser to treat skin melanoma. Currently, lasers are used in a variety of medical applications including, but not limited to dermatology, medical imaging, ophthalmology (e.g. LASIK) [54], surgery, and cancer treatment [54].

Laser-mediated intracellular drug delivery can be divided into methods which facilitate the transfer of laser energy to the cell. The literature segments laser-mediated delivery into optoporation and optoinjection methods. Optoporation utilizes a focused laser light to induce thermal damage in cell membranes, creating disruption and then molecular uptake [56]. Optoinjection uses laser light to create acoustic waves or shockwaves to mechanically impact cells and cause disruptions in the membrane to facilitate delivery.

This can be achieved using laser-nanoparticle interaction [57], [58] or shockwave lithography from shocktubes [59]–[61]

We can think of optoinjection methods as driven by energy transducers. That is, an energy absorber receives an external source of energy, converts the energy and then transmits it to its surroundings. A growing category of energy absorbers are nanoparticles for use in nanomedicine applications. Nanoparticles that can strongly absorb near infrared (NIR) laser energy are beneficial for clinical applications. Near-infrared lasers are used in the medical field because NIR light can penetrate several centimeters below the skin and transmit through blood and other components of complex tissue systems [62].

2.2.4 Laser-energy absorbing nanoparticles

2.2.4.1 Gold nanostructures

Metallic nanoparticles, such as gold (Au) are utilized for laser-mediated intracellular drug delivery. Au nanoparticles are highly regarded for their properties and potential for nanomedicine due to their biocompatibility and inherent structural and chemical properties. When Au nanoparticles are irradiated at a specific wavelength of laser light, delocalized electrons oscillate upon exposure to electromagnetic radiation. These electronic oscillations phenomena, coupled with subsequent scattering and absorption is known as the localized surface plasmon resonance (LSPR) effect [62]. When a noble metal nanoparticle absorbs laser light, the particle undergoes a series of electron oscillations, and as a result, heat rapidly transferred to the medium and stress waves are generated [63]. These photothermal effects have been useful for intracellular delivery [63]. The LSPR response is highly dependent on the size, shape, and morphology of the gold nanoparticle

[62]. Gold nanoparticles are useful if the surface plasmon resonance peaks are tuned to near-IR regions for biomedical applications (800-1200 nm) [62], [64].

2.2.4.2 Carbon nanoparticles

Carbon nanoparticles have also been leveraged for laser-mediated drug delivery platforms. Carbon has been studied in drug delivery research, evidenced by the growing popularity of carbon nanotubes and fullerenes [13], [26], [35], [65]. Carbon black (CB), a form of elemental carbon, has been used in medical tattoos and drug delivery [13], [14], while activated carbon/charcoal is used for filtration systems and most recently for possible treatment of irritable bowel syndrome [66]. Carbon black is manufactured to have a range of particle sizes on the nanoscale (25-75 nm) (**Figure 2.2**), but their preferred macrostructure is in the aggregated form [67], resulting in clusters on the order of hundreds of nanometers. Carbon black, in contrast to Au nanostructures, does not have a preferential absorption band in the IR regime but has a broadband absorption that includes the near IR [59] and is relatively inexpensive, abundantly available, and requires no particle modification.

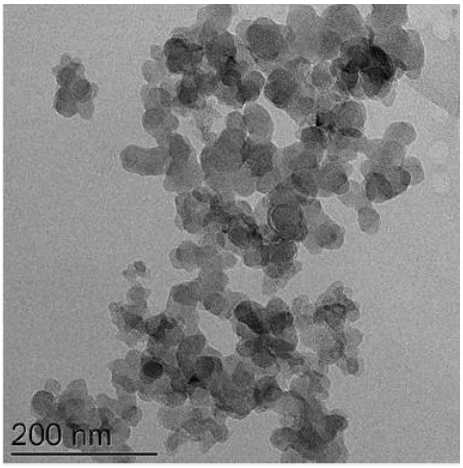

Figure 2.2: TEM image of carbon black nanoparticles with an average diameter of 28 nm as measured by ImageJ software. Scale bar = 200 nm.

2.2.5 Physical methods can be advantageous over chemical and biological methods

Overall, physical methods of drug delivery can be advantageous over chemical and biological methods. Since physical methods exploit external forces for delivery, these techniques are not limited to a particular cell type or drug. Additionally, since drug modification is unnecessary, the active substance can be targeted directly into the cytosol, avoiding the need for ligands or other surface targeting moieties [38]. This direct targeting also enables the bypassing the possibly damaging effects of biological pathways, i.e. endocytosis [7]. Finally, these methods are faster compared to chemical and biological techniques because molecules are delivered intracellularly during active disruption of the cell membrane. Nevertheless, the key challenge with physical methods is to balance the tradeoff associated with cell viability and high drug uptake due to physical forces impacting the cell [38], [39].

2.3 Carbon black for laser-mediated drug delivery

Researchers have studied carbon black extensively to understand its properties and its behavior upon IR laser irradiation. Carbon black has been shown to strongly absorb IR light and release the converted energy in acoustic waves. Diebold and colleagues studied the production of shockwaves, chemical products [68]–[71], and the "photoacoustic effect" [15] associated with IR irradiation of carbon black suspensions after sustained exposures. The photoacoustic effect is caused by a rapid volume change due to formation of a vapor shell around the heated particle. This change in volume induces a carbon-steam reaction, where the gaseous byproducts lead to a rise in pressure [15], [70].

Inspired by Chen and Diebold's photoacoustic effect studies, CB was incorporated into a laser-mediated drug delivery system to leverage CB's photoacoustic properties for disruption of membranes. From a historical context, a variety of studies were conducted in the Prausnitz Laboratory for Drug Delivery using ultrasound [16], [18]–[22], [44]. As previously mentioned, ultrasound drug delivery systems are challenging to optimize, due to the tradeoff between cell viability and molecular delivery. Carbon black's photoacoustic effect was thought to be a better alternative to ultrasound methods, which due to violent cavitation events can result in more cell death than delivery of molecules [22].

When carbon black nanoparticles in suspension with cells and small molecules were exposed to femtosecond-pulsed laser light resulted in high uptake and cell viability [13]. Chakravarty et al. [13], [72] used carbon black coupled with femtosecond and nanosecond laser pulses to deliver DNA, BSA (bovine serum albumin), and calcein (**Figure 2.3**) into DU145 human prostate cancer cells. It was hypothesized that the photoacoustic effect and the carbon-steam chemical reaction observed in Diebold's studies were mechanistically responsible for intracellular delivery. Due to heating of carbon

nanoparticles and the surrounding liquid medium, it was hypothesized that the carbon-steam reaction led to gaseous byproducts and bubble formation [13]. The hypothesis continued to posit that the subsequent collapse of these bubbles emitted acoustic waves [15] and mechanically interacted with the surrounding cellular membranes to create pores [13] and drive intracellular drug delivery.

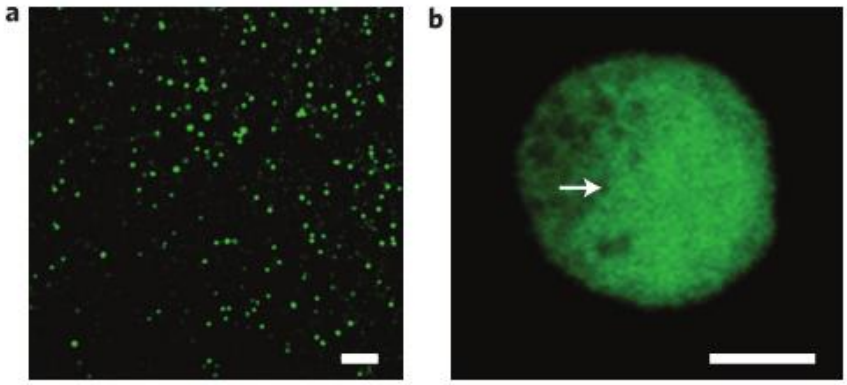

Figure 2.3: Fluorescent micrographs showing intracellular uptake of calcein at a) 10x magnification and b) 40x magnification, where the uptake of calcein is seen throughout the cell. Adapted from [13].

Subsequent work focused on investigating the effects of nanosecond pulsed laser energy. A Nd:YAG laser was an attractive alternative to the previously used Ti:Sapphire femtosecond laser, because of its low cost and ease of manipulation. Sengupta [14], [23] irradiated CB nanoparticles with a Nd:YAG nanosecond-pulsed laser to investigate the mechanisms and potential translational applications associated with this method. For example, using nanosecond-pulse laser energy with CB, siRNA was successfully delivered into ovarian cancer cells and led to gene knockdown [73]. Other studies showed that there is a delivery threshold for this method based on particle size (< 500 kDa) [14].

Sengupta [23] also explored this laser-CB method mechanistically and discovered several important facets fundamental to this thesis. They found that the carbon-steam reaction was not integral to the delivery mechanism as once hypothesized. In fact, it was concluded that the laser irradiation of CB nanoparticles and subsequent thermal expansion was the physical explanation for vapor formation and the release of acoustic waves. It was then hypothesized that the observed bioeffects were due to acoustic and/or thermal mechanisms. This was explained by the greater particle radius change due to vapor bubble formation than for solid volume expansion [23]. This secondary hypothesis posited that the combined energy transduction mechanisms, phenomena hereby referred to as transient nanoparticle energy transduction (TNET), were responsible for the observed bioeffects of high viability and high drug uptake.

Sengupta's work provided a basis to think of CB nanoparticles acting as energy transducers. The energy released was assumed to take different forms. Following laser irradiation of CB nanoparticles, it was hypothesized that CB could possibly transmit energy to the cell via two length-scales -- 1) long-range, indirect, cumulative acoustic emissions from bubbles or 2) short-range, local cell-bubble interaction:

(i) Long-range effects: Thermal expansion of particle leading to pressure disrupting the membrane

(ii) Long-range effects: acoustics/cumulative positive peak pressure output due to heat transfer from the particle which results in vapor formation and then disrupts the membrane

(iii) Short-range: local cell-particle / cell-bubble energy transfer

a. Heat transfer from physical contact of the bubble/particle to cell which create pores in the membrane
b. Point of source, local fluid mechanics and/or near-field acoustics which mechanically disrupt the membrane

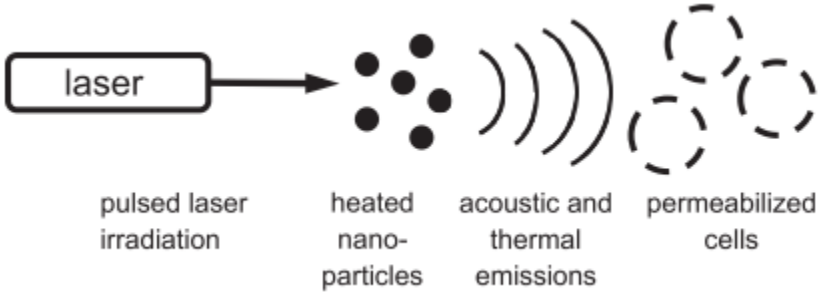

Figure 2.4: Schematic describing TNET where laser irradiation of CB nanoparticles leads to heating, and then acoustic & thermal energy transfer from the nanoparticles. Adapted from [23].

Some of these mechanisms were explored by Sengupta and colleagues. One crucial study from Sengupta's work was the acoustic characterization of carbon black nanoparticles. Several calculations and experiments suggested that a cell only experiences pressure from the nearest CB particles due to a shielding effect from a cumulative field of carbon nanoparticles [23]. This suggested that long-range interactions were not the dominant cause of TNET. Other results from this study showed that TNET was not due to the thermal expansion of the CB nanoparticles. Additionally, Sengupta established the theoretical energy transfer framework using Mie scattering theory, which enabled calculations of peak particle temperatures and vapor bubble size [23].

Nevertheless, there are still many unanswered questions related to TNET mechanistically. More specifically, we aim to have a more detailed understanding of the dominant energy modes which drive TNET. Within that, it is not known how the various

posited energy methods (i.e. (ii) – (iii) listed above) are related to CB's interaction with the cell, the role of cell mechanics in TNET, the influence of physical boundaries *in vitro*, and acoustic long- and near-field effects on the cell membrane. Hence, there is a need to further explore and validate the energetic mechanisms responsible for the observed bioeffects (e.g. highly efficient delivery) due to TNET. This dissertation seeks to addresses these questions and provide a more detailed, biophysical explanation for phenomena observed via transient nanoparticle energy transduction.

CHAPTER 3. ROLE OF CYTOSKELETAL MECHANICS AND CELL MEMBRANE FLUIDITY IN THE INTRACELLULAR DELIVERY OF MOLECULES MEDIATED BY LASER-ACTIVATED CARBON NANOPARTICLES

3.1 Introduction

During TNET, CB nanoparticles strongly absorb near-infrared laser energy and convert the energy into other forms (e.g. pressure, heat) which are transduced into the surrounding medium [23]. More specifically, laser irradiation is believed to heat the CB nanoparticles by hundreds of degrees Celsius, which causes vaporization of the surrounding medium to create bubbles that transfer heat and momentum (e.g. fluid flow and acoustic waves) to nearby cells. These thermal and mechanical stresses are believed to generate transient membrane pores that enable intracellular delivery of molecules as well as sometimes cause cell death.

The biophysical interactions between cells and TNET energy transfer, however, are not fully understood. More specifically, the role of cell mechanical properties has not been studied. Thus, we conducted a study to determine the effects of cytoskeletal mechanics and plasma membrane fluidity on intracellular uptake and cell viability (i.e., bioeffects) associated with TNET. We hypothesize that weakening the cytoskeleton by destabilizing actin filaments increases intracellular uptake of molecules and reduces cell viability loss, whereas altering plasma membrane fluidity may increase or decrease uptake and viability due to TNET.

3.2 Methods

3.2.1 Nanoparticle Preparation

CB nanoparticles were prepared as previously described [14]. In brief, CB nanoparticles (Black Pearls 470, Cabot, Boston, MA) were added at a concentration of 0.4 g/L to deionized water containing 0.013% (v/v) Tween-80 (Sigma-Aldrich, St. Louis, MO) to enhance solution stability. The solution was sonicated for 35 min in an ultrasonic water bath (FS3OH, Fisher Scientific, Pittsburg, PA) and with an ultrasonic needle for 1 min (Sonics Ultracell, Sonics & Materials, Newton, CT). According to the manufacturer, individual CB nanoparticles were 25 nm in size. However, dynamic light scattering measurements conducted by us revealed that the nanoparticle assembled into clusters with an effective diameter of 201.4 ± 5.5 nm (n=10) and a dispersity of 0.15 ± 0.04 nm (n=10 replicates) (ZetaSizer Nano, Malvern Instruments, Malvern, UK). Sonication described above was not able to decrease cluster size further.

3.2.2 Laser system for in vitro exposures

A Nd:YAG solid-state laser (Continuum Powerlite II Plus, Continuum, San Jose, CA) was used to apply 5-9 ns pulses of 1064 nm wavelength at a frequency of 10 Hz (i.e. 10 pulses per second) to cell suspensions. Pulse fluence was varied by changing the amplifier voltage settings of the laser. The initial Super-Gaussian 12 mm wide beam was passed through an 8 mm aperture to create a pseudo-flat top profile to achieve a more homogeneous distribution of the laser energy. The 8 mm beam was then passed through a diverging lens (f =50 cm) (ThorLabs, Newton, NJ) to illuminate the entire exposure area of the cuvette (4 cm^2).

3.2.2.1 Laser beam characterization

A laser beam profiler (LaserCam HR 1098577, Coherent, Santa Clara, CA) was used to characterize the 12 mm super-Gaussian beam emitted from the Nd:YAG laser (Continuum Powerlite II Plus, Continuum, San Jose, CA) prior to and following its propagation through an 8 mm aperture. Several neutral density filters were used to prevent saturation of the signal and damage to the LaserCam HR. The pseudo-flat top beam profile showed a more homogenous distribution of energy compared to the super-Gaussian beam (**Figure 3.1**).

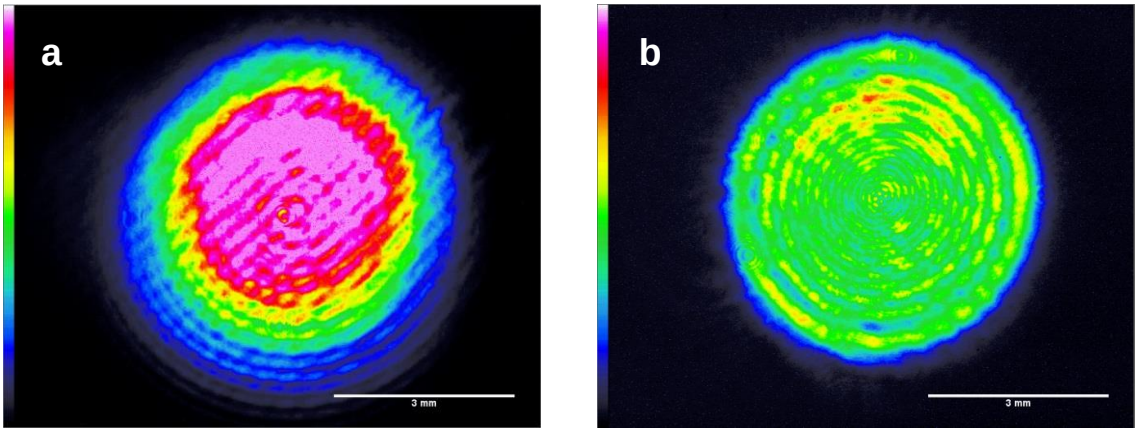

Figure 3.1: Beam profiles of a) super-Gaussian beam and b) pseudo-flat top beam captured with the LaserCam HR. The false color scale bar (left of the profiles) is a qualitative measure of intensity, where the color at the top of the bar is the maximum intensity (BeamView USB 4.8.1 software). The laser beam was focused down using a biconvex lens due to the LaserCam HR camera's 6 mm diameter. Scale bar = 3 mm.

3.2.3 Altering cytoskeleton via actin manipulation

To alter the cytoskeleton's mechanical properties, latrunculin A (LatA) was used to inhibit actin polymerization and dissemble actin filaments [74]–[76] and jasplakinolide (Jasplak) was used to promote actin polymerization, thereby reinforcing and rigidifying actin filaments in the cytoskeleton [77]. LatA (Sigma-Aldrich) was dissolved in ethanol at

a stock concentration of 75 µM and Jasplak (Cayman Chemicals, Ann Arbor, MI) was also dissolved in ethanol at a stock concentration of 10 µM.

3.2.3.1 Assay to measure actin destabilization

A high throughput assay leveraging flow cytometry was developed to quantify actin content via fluorescence of phalloidin. In brief, DU145 cells were incubated with latrunculin A (LatA) for 30 – 60 min at 37ºC. Then, cells were fixed with 4% paraformaldehyde at room temperature and permeated with 0.1% Triton X-100 (Sigma-Aldrich, St. Louis, MO) for staining with fluorescently labeled Alexa Fluor 488–phalloidin (ThermoFisher Scientific, Waltham, MA). Alexa Fluor 488–phalloidin was used to quantify actin fluorescence after DU145 cells were treated with 0.1, 0.3, 0.5, 1, and 5 µM LatA. Histograms from a BD Accuri C6 flow cytometer (Becton Dickinson, Franklin Lakes, NJ) show a significant decrease in the FL1-A signal (FITC channel) with increasing LatA (**Figure 3.2**).

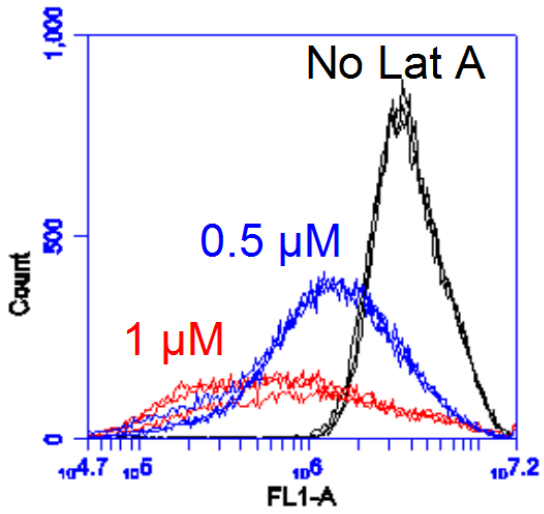

Figure 3.2: Histogram displaying relative Alexa Fluor 488 phalloidin fluorescence for non-treated cells and cells treated with 0.5 and 1 µM LatA.

The total fluorescence signal from the FITC channel for samples were analyzed to compare relative fluorescence. Cells treated with LatA were normalized to cells without LatA treatment, but stained with Alexa Fluor 488–phalloidin to quantify the initial actin fluorescence in DU145 cells (**Figure 3.3**). Latrunculin A's effect of decreasing actin fluorescence was consistent with other studies in literature [74], [75], [78].

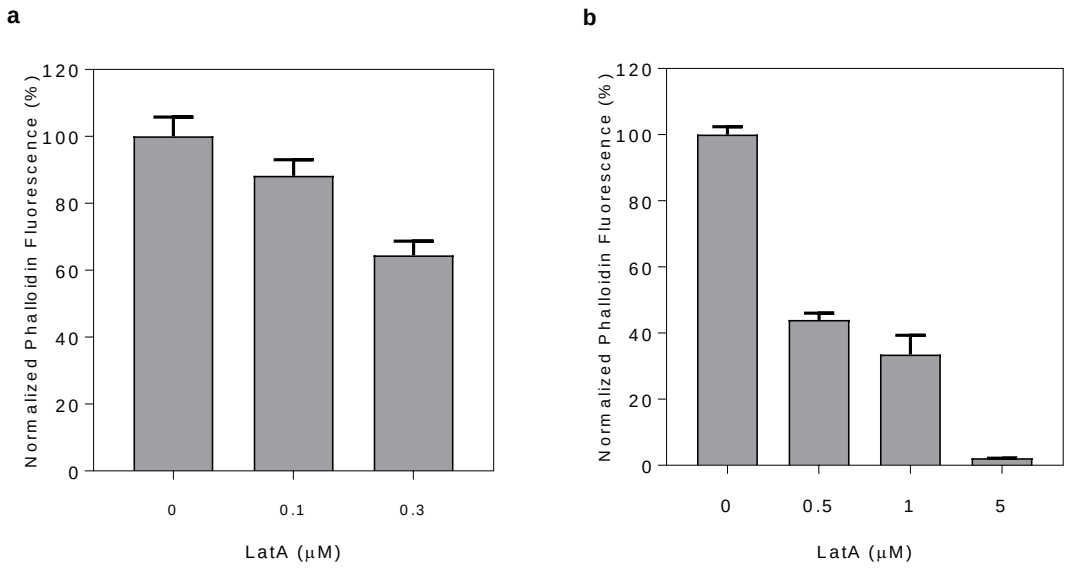

Figure 3.3: Normalized phalloidin fluorescence for DU145 cells stained with Alexa Fluor 488–phalloidin. a) Cells treated with 0.1 µM LatA and 0.3 µM LatA and incubated for 60 min at 37ºC. b) Cells treated with 0.5 µM, 1 µM and 5 µM LatA and incubated for 30 min at 37 ºC. Data show mean and SD (n≥3).

3.2.4 Altering cholesterol content of plasma membrane

Cholesterol content of the plasma membrane was decreased using methyl-β-cyclodextran (MβCD; Sigma-Aldrich) [79] and increased using water-soluble cholesterol (WSC; Sigma-Aldrich). MβCD was prepared in deionized water at a stock solution of 38 mM and WSC was also prepared in deionized water at a stock concentration of 200 mM [76].

3.2.4.1 Assays to confirm cholesterol depletion or enrichment with cholesterol-based reagents

An Amplex-Red cholesterol oxidase assay (ThermoFisher Scientific, Waltham, MA) was used to quantify total cholesterol content for cells treated with MβCD and WSC. DU145 cells were incubated with 200 µM, 1mM and 10 mM MβCD, and 0.1 mM, 1 mM and 5 mM WSC. Cells were seeded at 2500 cells/well in 100 µL onto a black 96 well tissue-cultured treated plate for 24 hours. The fluorescence intensity was measured with a spectrophotometer (Synergy H4, BioTek, Winooski, VT) after one hour of incubation at 37ºC, with excitation and emission peaks at 530 nm (±25) and 590 nm (±35), respectively. MβCD decreased the total cholesterol content compared to non-treated cells (**Figure 3.4a**), whereas WSC increased cholesterol content compared to non-treated cells (**Figure 3.4b**).

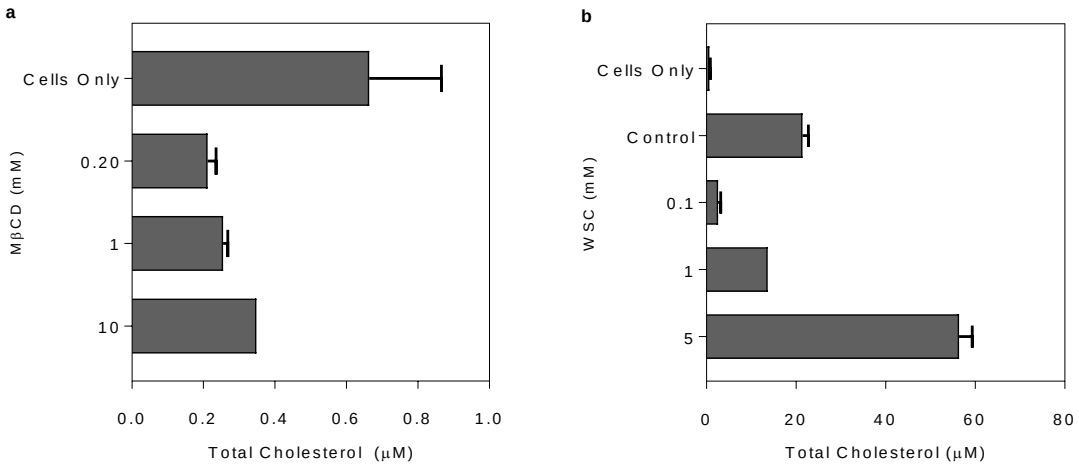

Figure 3.4: Total cholesterol content (µM) for ~2.5 x 10^3 DU145 cells treated with a) MβCD and b) WSC following 1 hour of incubation at 37ºC. The total cholesterol content is the summation of cholesteryl esters plus free cholesterol detected by the cholesterol oxidase assay. Data show mean and SD (n ≥ 3).

3.2.5 Cell culture and in vitro experiments

Human prostate cancer cells (DU145, American Type Culture Collection, Manassas, VA) were cultured as monolayers in a humidified atmosphere of 95% air and 5% CO_2 at 37°C in RPMI-1640 medium (Cellgro, Herndon, VA) supplemented with 100 g/mL penicillin-streptomycin (Cellgro) and 10% (v/v) heat inactivated fetal bovine serum (FBS) (Corning, Palo Alto, CA). Cells were harvested at 80-90% confluence for experiments by trypsin/EDTA (Cellgro) digestion, washed with serum and then re-suspended in RPMI at a cell concentration of 10^6 cells/mL. DU145 cells were used as the model cell line for these experiments because these cells have been widely used and characterized in previous drug delivery studies [13], [14], [20].

Harvested cells were mixed with carbon nanoparticles at a final concentration of 25 mg/L and high-purity calcein (Molecular Probes, Eugene, OR) as an uptake marker at a final concentration of 10 μM, and kept in 1.5 mL microcentrifuge tubes on ice. In some cases, reagents for cytoskeleton and cell membrane manipulation were added and incubated at 37º C for 1 h before laser exposure. Then, 520 μL of the cell suspension was transferred to Pyrex glass cuvettes (37-PX-2, Starna Cells, Atascadero, CA) for laser exposure. Negative controls in the form of 'sham' exposures were samples containing cells, CB nanoparticles, and calcein that experienced the same handling and procedures except the laser exposure.

Following laser exposure, the cuvette contents were transferred back into the microcentrifuge tubes with a transfer pipette and stored on ice to reduce uptake due to endocytosis. To label nonviable, necrotic cells post-irradiation, propidium iodide (Invitrogen, Grand Island, NY) was added at a final concentration of 13.4 μM for 10 min

on ice. Samples were washed at least 3 times with phosphate buffer saline (PBS) to remove excess fluorescence from the bulk solution before analysis by flow cytometry.

3.2.6 Data collection & processing

A bench-top flow cytometer (BD Accuri, BD Biosciences, San Jose, CA) quantified bioeffects in terms of live cells with intracellular uptake (i.e. intact cells with green fluorescence of calcein loading and without red fluorescence of propidium iodide staining) and non-viable cells (i.e. intact cells with propidium iodide staining). Calcein fluorescence was measured using 530/28 nm bandpass filter with excitation at 488 nm and propidium iodide fluorescence was measured using a 670 nm longpass filter with a maximum excitation at 535 nm.

Samples were run at a constant flow rate of 35 μL/min for 1 min. A negative control containing only cells in RPMI was used to construct a cell population gate in the forward-scattered and side-scattered analysis. Cells within this gate were considered to be intact cells. To account for possible cell loss due to cell fragmentation (appearing as low forward scatter and low side scatter events on the flow cytometer), the difference between the number of viable cells (i.e., not stained by propidium iodide) detected in a given sample compared to viable cells detected in sham samples was taken to equal the number of cells lost to fragmentation [80].

3.2.7 Statistical analysis

A minimum of three replicates was used for all conditions, which enabled calculation of means and standard deviations. The null hypothesis was that the average

fraction of cells with uptake or viability in a sham sample and an exposed sample were equal. The equality of means response between exposed samples and sham samples was tested with ANOVA ($\alpha = 0.05$). The equality of means response was tested with 1-way or 2-way ANOVA followed by post-hoc Tukey's pairwise comparison using GraphPad Prism 6 (GraphPad Software, La Jolla, CA).

3.3 Results

3.3.1 Evaluating role of cytoskeleton by actin manipulation with latrunculin A and jasplakinolide

We exposed cells to different concentrations of LatA to decrease the actin content in the cytoskeleton using established methods [74], [78] and verified actin content reduction using an established phalloidin fluorescence assay [81] (**Figure 3.2**, **Figure 3.3**). After completing this validation, cells with and without LatA treatment at different concentrations were exposed to laser pulses over a range of fluence values to determine the effect of cytoskeletal weakening on intracellular uptake of molecules and cell viability (**Figure 3.**).

At low LatA concentration (0.1 µM), mild cytoskeletal weakening had a protective effect that enabled higher intracellular uptake of molecules (**Figure 3.a(i)**) and less loss of cell viability (**Figure 3.b(i)**) at moderate laser fluence. However, this treatment did not have an effect at higher laser fluence where perhaps mild cytoskeletal weakening could not protect against strong TNET forces. In this analysis, intracellular uptake of molecules is expressed as the percent of cells exhibiting uptake of the small molecule fluorescent marker, calcein (623 Da molecular weight). Loss of cell viability is expressed as the percent

of cells either identified as non-viable due to staining with propidium iodide or identified as fragmented during laser treatment.

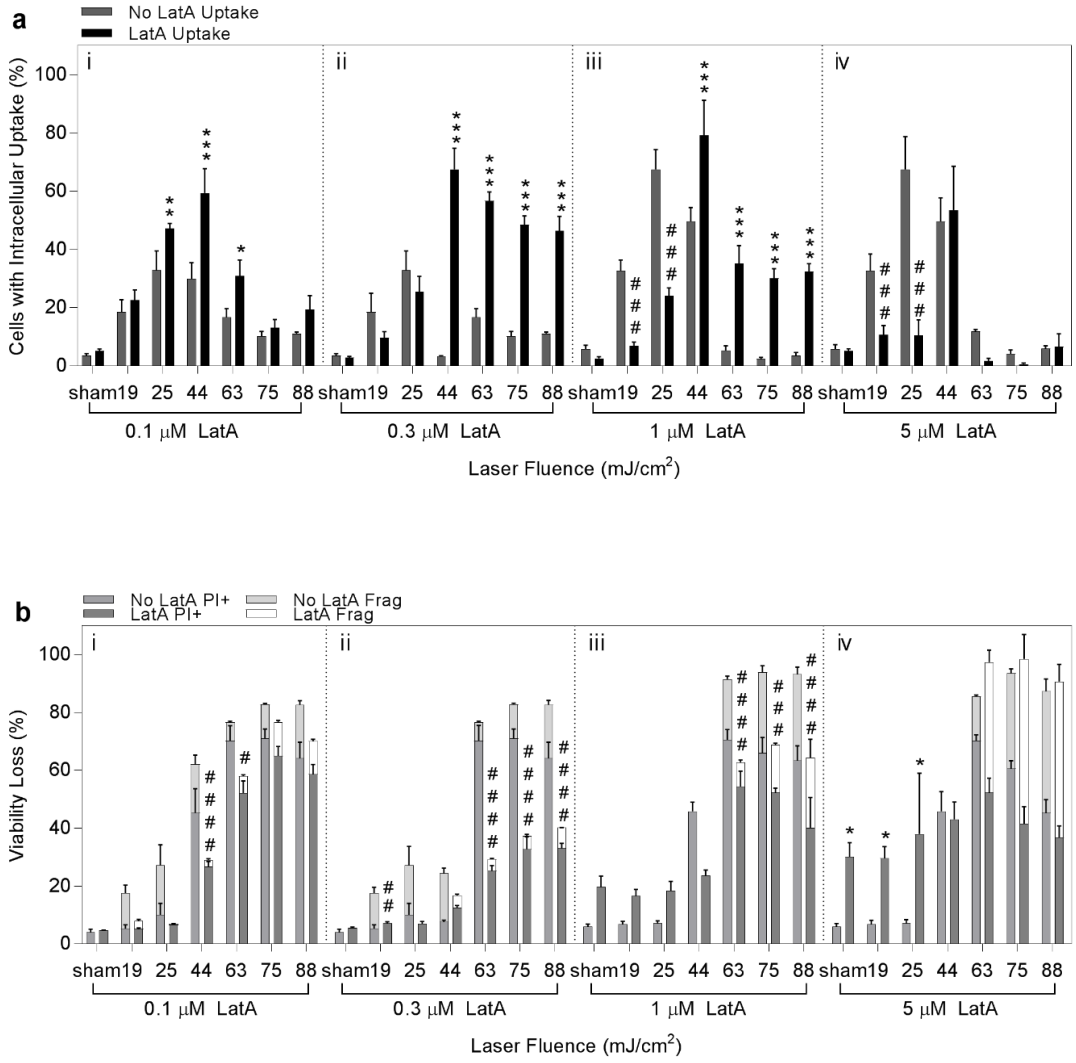

Figure 3.5: Percentage of latrunculin-A (LatA)-treated and non-treated cells with a) intracellular uptake, b) viability loss and c) (*continued on next page*) total bioeffects (uptake and viability loss) after 1 minute of pulsed exposure to laser fluence ranging from 19 - 88 mJ/cm^2. Non-viable cells are subdivided into those staining positive for propidium iodide (PI+) and those determined to be fragmented. Cells were treated with i) 0.1 µM LatA, ii) 0.3 µM LatA, iii) 1 µM LatA, and iv) 5 µM LatA. Asterisks (*) indicate bioeffect was significantly lower in samples with LatA treatment versus companion samples without LatA treatment (ANOVA, * p < 0.05, ** p < 0.01, *** p < 0.001, **** p < 0.0001). Pound (#) indicates bioeffect was significantly higher in samples with LatA treatment versus companion samples without LatA treatment (ANOVA, # p < 0.05, ## p < 0.01, ### p < 0.001, #### p < 0.0001). Data show average ± SD (n=3).

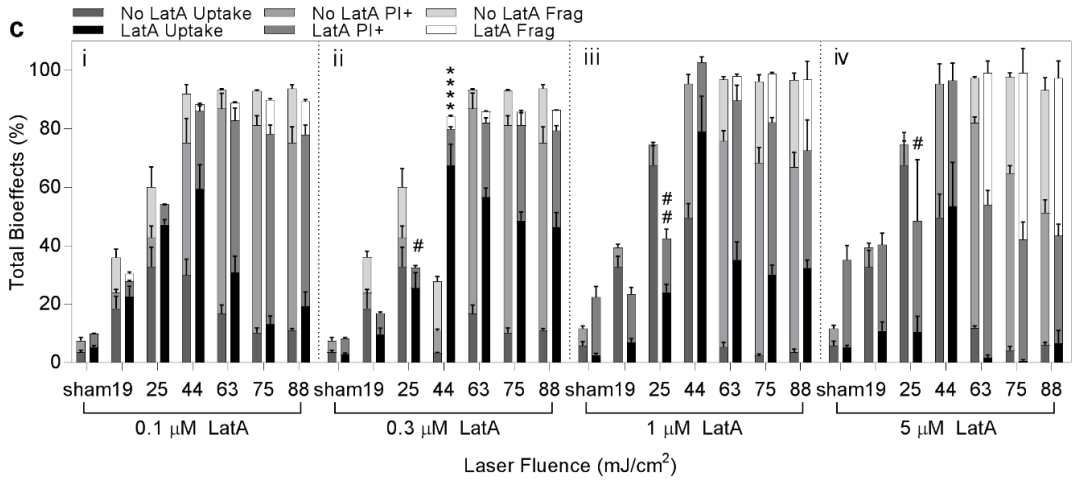

Figure 3.5 (continued): Percentage of latrunculin-A (LatA)-treated and non-treated cells with a) intracellular uptake, b) viability loss and c) total bioeffects (uptake and viability loss) after 1 minute of pulsed exposure to laser fluence ranging from 19 - 88 mJ/cm^2. Non-viable cells are subdivided into those staining positive for propidium iodide (PI+) and those determined to be fragmented. Cells were treated with i) 0.1 µM LatA, ii) 0.3 µM LatA, iii) 1 µM LatA, and iv) 5 µM LatA. Asterisks (*) indicate bioeffect was significantly lower in samples with LatA treatment versus companion samples without LatA treatment (ANOVA, * p < 0.05, ** p < 0.01, *** p < 0.001, **** p < 0.0001). Pound (#) indicates bioeffect was significantly higher in samples with LatA treatment versus companion samples without LatA treatment (ANOVA, # p < 0.05, ## p < 0.01, ### p < 0.001, #### p < 0.0001). Data show average ± SD (n=3).

At higher LatA concentration (0.3 μM, 1 μM), the increased level of cytoskeletal weakening had a protective effect that enabled higher intracellular uptake (**Figure 3.a(ii) and Figure 3.a(iii)**) and less cell viability loss (**Figure 3.b(ii) and Figure 3.b(iii)**) at both moderate and high laser fluence. However, at low laser fluence, treatment with 1 μM LatA had a negative effect on cells, causing lower uptake (**Figure 3.a(iii)**) and more viability loss (even among sham-exposed cells, **Figure 3.b(iii)**), suggesting that the toxic effects of a higher concentration of LatA outweighed its protective effects under mild TNET conditions. LatA concentrations above 0.5 μM are known to cause severe cytoskeletal weakening that can affect cell viability [74], [77].

Finally, at the highest LatA concentration (5 μM), the toxic effects of LatA were even more evident, where the high level of cytoskeletal weakening caused less uptake (**Figure 3.a(iv)**) and more viability loss (again, even among sham-exposed cells, **Figure 3.b(iv)**) and provided no protective effect at higher laser fluence.

Considering the total bioeffects – i.e., all cells exhibiting either intracellular uptake or loss of viability – we see that overall (with a few exceptions) there is no significant difference in the total fraction of cells affected by laser exposure with versus without LatA treatment (**Figure 3.5**Figure 3.**c**). This suggests that LatA does not primarily affect the initial impact of TNET on cells, but rather affects the cells' ability to recover from that impact. We propose that cells with intact cytoskeletons that are permeabilized by TNET may be more likely to become non-viable afterwards due to an inability to recover from the transient damage done by TNET (i.e., what would have been uptake cells become nonviable cells). In contrast, we propose that cells with weakened cytoskeletons are better able to recover from TNET exposures, thereby keeping permeabilized cells viable (i.e.,

uptake cells remain viable). This interpretation is further supported by the observation that there are similar and low levels of fragmented cells among LatA-exposed and non-exposed cells, other than at the highest LatA concentration where LatA toxicity appears to become an important factor. Cell fragmentation is believed to occur at the time of TNET impact on cells, whereas nonviable cells identified by propidium iodide staining are believed to be cells that became nonviable due to stresses after TNET exposure. These interpretations require additional study and further validation.

Given the dramatic effects of cytoskeletal weakening by LatA, we next studied the effects of exposure of cells to Jasplak, which increases actin polymerization and rigidifies existing filaments, thereby strengthening the cytoskeleton [77], [82]. We used a single concentration of 0.5 μM Jasplak, based on prior literature [74], [77]. Intracellular uptake was generally unaffected by exposure to Jasplak, other than at 44 mJ/cm^2, where uptake was higher (**Figure 3.6a**). Cell viability loss (**Figure 3.6b**) and total cells with bioeffects (**Figure 3.6c**) were unaffected at all conditions studied. It is interesting to note, however, that the percentage of fragmented cells was significantly less among cells exposed to Jasplak (ANOVA, $p < 0.001$), suggesting that strengthening the cytoskeleton inhibited cell fragmentation.

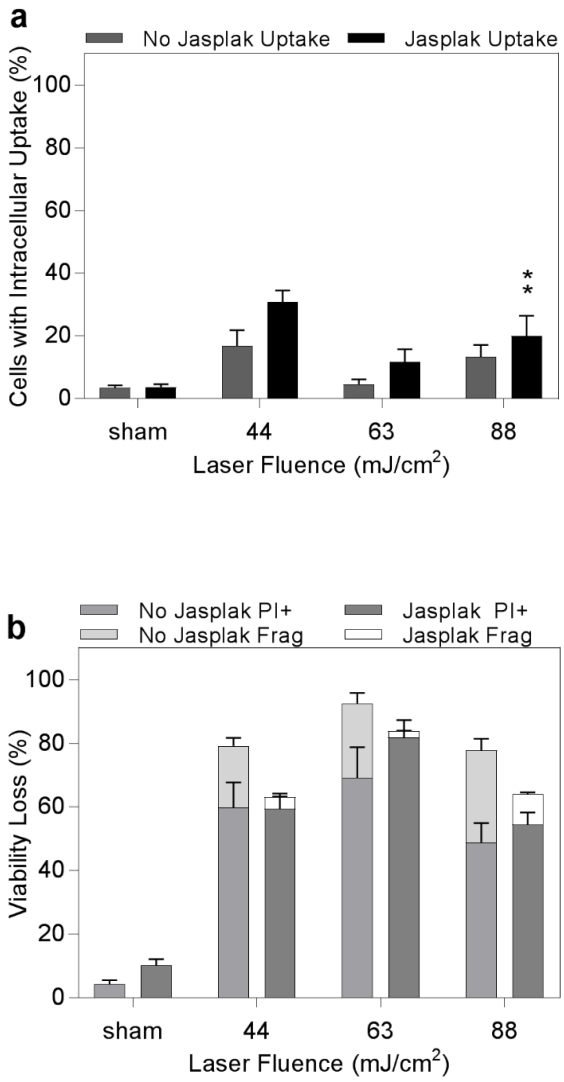

Figure 3.6: Percentage of Jasplakinolide (Jasplak)-treated and non-treated cells with a) intracellular uptake, b) viability loss and c) (*continued on next page*) total bioeffects (uptake and viability loss) after 1 minute of exposure to laser fluence of 44, 63, and 88 mJ/cm^2. Non-viable cells are subdivided into those staining positive for propidium iodide (PI+) and those determined to be fragmented. Asterisks (**) indicate bioeffect was significantly higher in samples with Jasplak treatment versus companion samples without Jasplak treatment (ANOVA, ** $p < 0.01$). Data show mean ± SD (n=3).

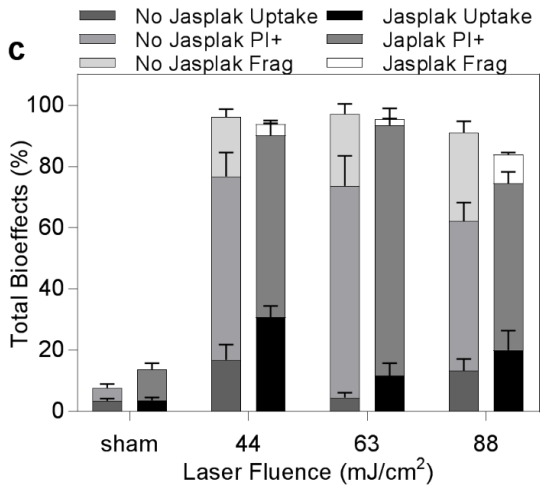

Figure 3.6 (continued): Percentage of Jasplakinolide (Jasplak)-treated and non-treated cells with a) intracellular uptake, b) viability loss and c) total bioeffects (uptake and viability loss) after 1 minute of exposure to laser fluence of 44, 63, and 88 mJ/cm^2. Non-viable cells are subdivided into those staining positive for propidium iodide (PI+) and those determined to be fragmented. Asterisks (**) indicate bioeffect was significantly higher in samples with Jasplak treatment versus companion samples without Jasplak treatment (ANOVA, ** $p < 0.01$). Data show mean ± SD (n=3).

3.3.2 Evaluating role of plasma membrane fluidity with methyl-β-cyclodextrin and water-soluble cholesterol

Cholesterol helps to regulate the overall fluidity of the cell membrane [83], [84]. Exposure of cells to MβCD can increase cell membrane fluidity by depleting cholesterol from the cell membrane [85]–[87], whereas WSC can enrich the membrane with cholesterol and thereby decrease membrane fluidity [88], [89]. We validated these methods of altering cholesterol content in cell membranes (**Figure 3.4**).

To determine if increased cell membrane fluidity affected cellular bioeffects of TNET, we treated cells treated with two different concentrations of MβCD and found that there were no significant differences in uptake, viability loss (including cell fragmentation) or total bioeffects at all laser fluence values, with only one exception (**Figure 3.7a-c**). We therefore conclude that increased membrane fluidity due to MβCD exposure did not significantly influence bioeffects caused by TNET under the conditions studied.

To decrease membrane fluidity, cells were treated with WSC at three different concentrations and then exposed to TNET using a range of laser fluence values. In general, cells treated with WSC showed similar uptake, viability loss (including cell fragmentation) and total bioeffects at all conditions studied, with only a few exceptions (**Figure 3.8**). We therefore conclude that decreased membrane fluidity due to WSC exposure had little or no significant influence on bioeffects caused by TNET under the conditions studied.

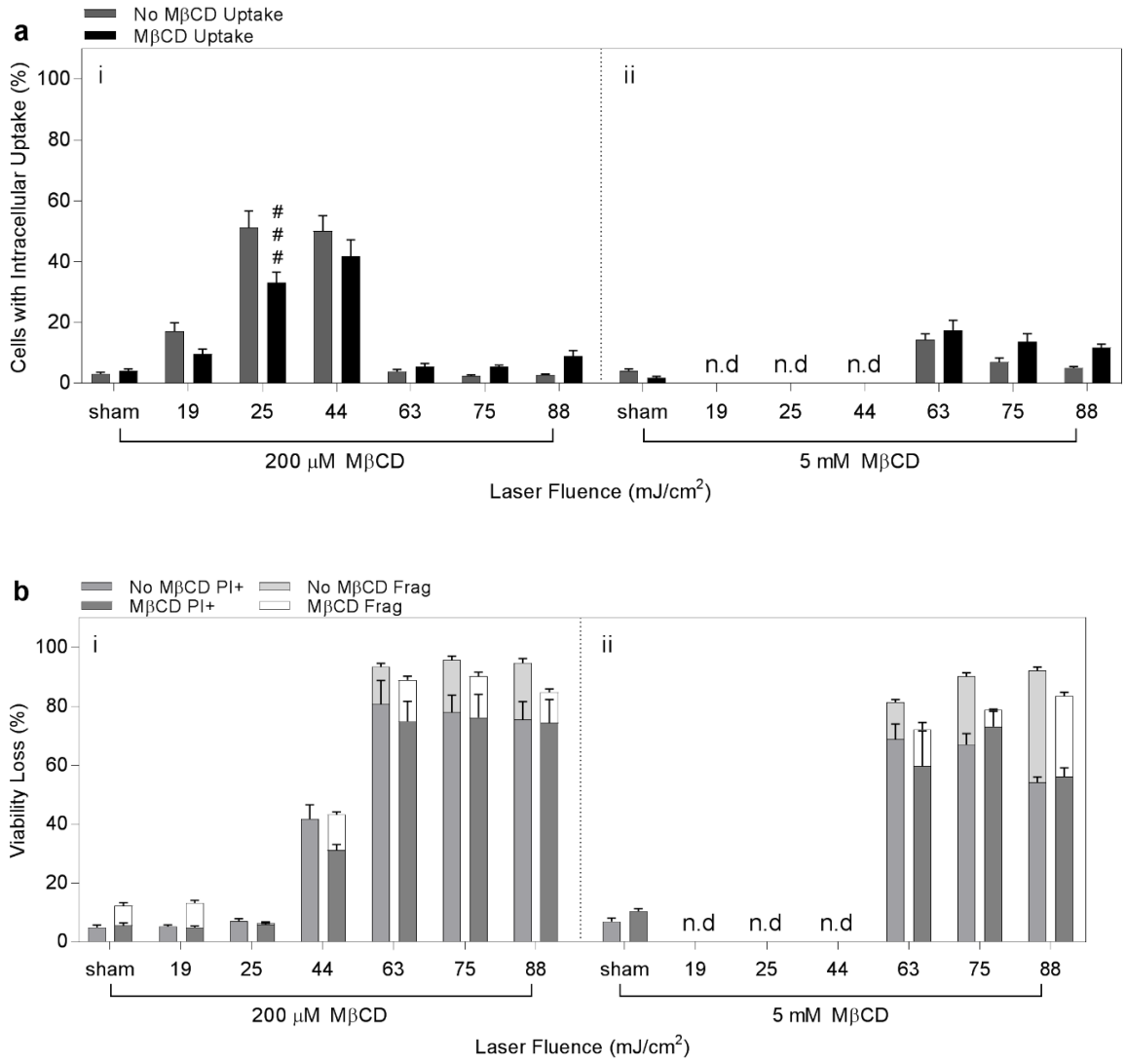

Figure 3.7: Percentage of methyl-β-cyclodextran (MβCD)-treated and non-treated cells with a) intracellular uptake, b) viability loss and c) (*continued on next page*) total bioeffects (uptake and viability loss) after exposure for 1 minute to laser fluence ranging from 19 – 88 mJ/cm^2. Non-viable cells are subdivided into those staining positive for propidium iodide (PI+) and those determined to be fragmented. Cells were treated with i) 200 μM MβCD and ii) 5 mM MβCD. 'n.d' signifies no data for that condition. Pound (#) indicates bioeffect was significantly lower in samples with MβCD treatment versus companion samples without MβCD treatment (ANOVA, $p < 0.001$). Data show mean ± SD (n=3).

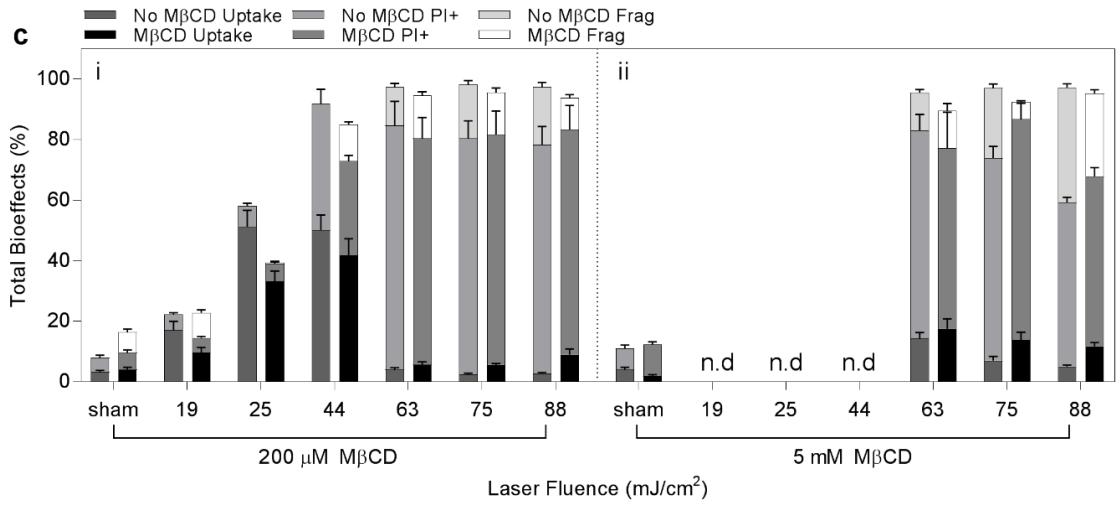

Figure 3.7 (continued): Percentage of methyl-β-cyclodextran (MβCD)-treated and non-treated cells with a) intracellular uptake, b) viability loss and c) total bioeffects (uptake and viability loss) after exposure for 1 minute to laser fluence ranging from 19 – 88 mJ/cm^2. Non-viable cells are subdivided into those staining positive for propidium iodide (PI+) and those determined to be fragmented. Cells were treated with i) 200 μM MβCD and ii) 5 mM MβCD. 'n.d' signifies no data for that condition. Pound (#) indicates bioeffect was significantly lower in samples with MβCD treatment versus companion samples without MβCD treatment (ANOVA, $p < 0.001$). Data show mean ± SD (n=3).

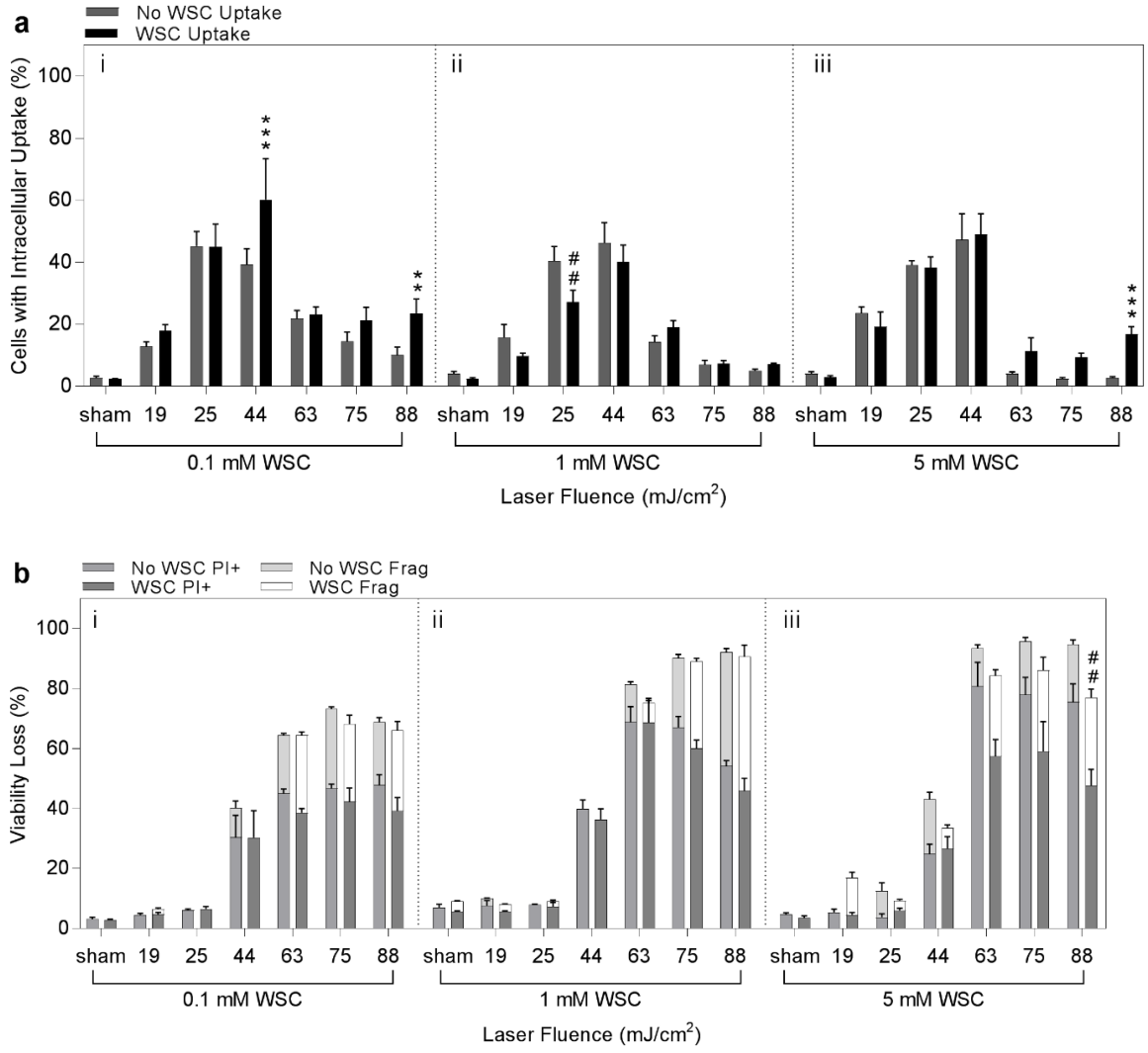

Figure 3.8: Percentage of water-soluble cholesterol (WSC)-treated and non-treated cells with a) intracellular uptake, b) viability loss and c) (*continued on next page*) total bioeffects (uptake and viability loss) after exposure for 1 minute to laser fluence ranging from 19 - 88 mJ/cm^2. Non-viable cells are subdivided into those staining positive for propidium iodide (PI+) and those determined to be fragmented. Cells were treated with i) 0.1 mM WSC, ii) 1 mM WSC, and iii) 5 mM WSC. Asterisks (*) indicate bioeffect was significantly higher in samples with WSC treatment versus companion samples without WSC treatment (ANOVA, ** $p < 0.01$, *** $p < 0.001$). Pound (#) indicates bioeffect was significantly lower in samples with WSC treatment versus companion samples without WSC treatment (ANOVA, ## $p < 0.01$). Data show mean ± SD (n=3).

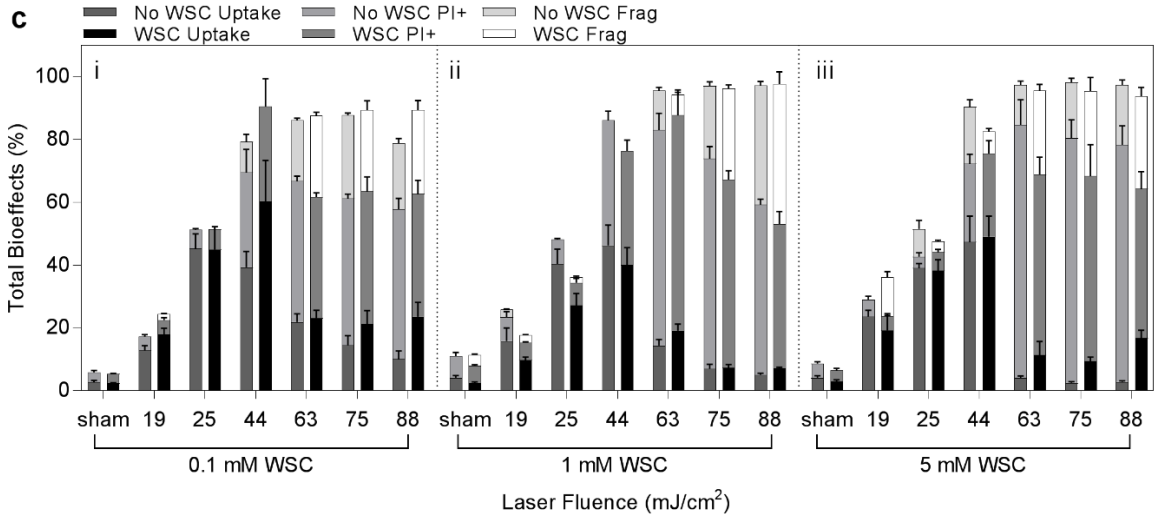

Figure 3.8 (continued): Percentage of water-soluble cholesterol (WSC)-treated and non-treated cells with a) intracellular uptake, b) viability loss and c) total bioeffects (uptake and viability loss) after exposure for 1 minute to laser fluence ranging from 19 - 88 mJ/cm^2. Non-viable cells are subdivided into those staining positive for propidium iodide (PI+) and those determined to be fragmented. Cells were treated with i) 0.1 mM WSC, ii) 1 mM WSC, and iii) 5 mM WSC. Asterisks (*) indicate bioeffect was significantly higher in samples with WSC treatment versus companion samples without WSC treatment (ANOVA, ** $p < 0.01$, *** $p < 0.001$). Pound (#) indicates bioeffect was significantly lower in samples with WSC treatment versus companion samples without WSC treatment (ANOVA, ## $p < 0.01$). Data show mean ± SD (n=3).

3.4 Discussion

The goal of this investigation was to study the influence of cytoskeletal mechanics and the fluidity of the plasma membrane on bioeffects observed with TNET. We hypothesized that weakening cytoskeleton by destabilizing actin filaments increases intracellular uptake of molecules and reduces cell viability loss, whereas altering plasma membrane fluidity has could increase or decrease uptake or viability due to TNET. The results from this study support the former hypothesis, however our fluidity studies showed that there is no significant effect on bioeffects.

3.4.1 Weakening cytoskeletal mechanical properties increased intracellular uptake and reduced viability loss

It is notable that intracellular uptake was increased and viability loss was reduced by cytoskeletal weakening via treatment of cells with LatA (**Figure 3.5**). This finding can provide mechanistic insight into TNET's effects on cells and suggest strategies to increase intracellular delivery of molecules into viable cells, which is a desirable outcome for laboratory and possible future medical applications.

The cytoskeleton provides mechanical and spatial support to the cell and more specifically supports the plasma membrane [90]. Mechanical stresses imparted on a eukaryotic cell are distributed by the cytoskeleton [91], [92], which consists of a biopolymer network of proteins, including actin filaments, microtubules, and intermediate filaments. Actin filaments provide elastic support for the cell, and dynamically assemble and disassemble in response to local stress perturbations to maintain entropic stability [91].

3.4.1.1 Hypothesis #1

We hypothesize that TNET results in a mechanical impact on cells due to an acoustic pressure pulse and/or fluid motion caused by rapidly expanding vapor bubbles surrounding the CB nanoparticle [23]. Weakening the cytoskeleton could alter this mechanical interaction by making the cell more susceptible to deformation and thereby altering the nature of the cell membrane permeabilization that occurs. This change could result in greater and/or longer-lasting permeabilization of the membrane leading to increased intracellular uptake. Other studies demonstrated that LatA disrupts the actin network and can reduce the average Young's modulus by a factor of 3, leading to a significant reduction in the cell's mechanical strength [74].

3.4.1.2 Hypothesis #2

Our first hypothesis does not appear to be sufficient to explain the reduced cell viability loss that was also observed. Another explanation is that the changed interaction between the mechanical forces of TNET and a structurally weakened cell enable permeabilized cells to recover and retain viability more effectively. We hypothesize that some cells permeabilized by TNET can recover from that intervention and thereby be classified as cells with uptake, and that other cells do not recover and are therefore classified as non-viable. It may be that the nature of the permeabilization caused by TNET in cells with weakened cytoskeleton allows them to more easily recover, thereby yielding a greater fraction of cells that remain viable and are therefore classified as cells with uptake. This interpretation is further supported by the observation that the total fraction of cells affected by TNET was independent of treatment with LatA (**Figure 3.5c**). It appears that

cytoskeletal weakening shifted cells from the non-viable classification to the intracellular uptake classification by helping preserve cell viability.

3.4.1.3 Hypothesis #3

There is a third hypothesis that we propose, which is that weakening cytoskeleton has no significant effect at the time of mechanical force impact generated by TNET, i.e., the degree and nature of cell membrane permeabilization does not significantly depend on cytoskeletal weakening, at least under the conditions of this study. Instead, alterations to the cytoskeleton by LatA treatment affect the ability of cells to repair and recover from the transient permeabilization that occurred. It is known from the literature that membrane breaches are generated in cells due to direct application of mechanical forces and the process of repairing these membrane breaches involves transient tethering of the plasma membrane to the underlying cytoskeleton. This would suggest that TNET is a mechanical mechanism being that higher viability was obtained after LatA treatment. The cytoskeleton can act as a physical obstacle for the 'docking' of microvesicles needed for membrane fusion [93], [94]. In this way, destabilizing actin filaments can enhance membrane resealing [94], [95]. Thus, the effects of LatA on the cytoskeleton may facilitate cell membrane repair and/or other intracellular recovery processes that help cells maintain viability.

3.4.2 Strengthening cytoskeletal mechanical properties did not affect intracellular uptake or cell viability

We expected that a rigidified cytoskeleton after treatment with Jasplak would result in less intracellular uptake compared to non-treated cells. Despite that expectation, uptake

and viability loss among Jasplak-treated cells were similar to non-treated cells (**Figure 3.6**). In data not shown, higher Jasplak concentration (i.e., 1 μM) to rigidify actin filaments further [96] was toxic to cells (i.e., even without TNET in 'sham' cells) and resulted in a substantial increase in viability loss prior to laser exposure. Therefore, we tested the highest amount of cytoskeletal rigidification possible with Jaspak in our cells under the conditions studied.

The literature presents conflicting results regarding Jasplak's effects. Some studies indicate that Jasplak stabilizes actin filaments and rigidifies the cytoskeleton [77], [97], [98], while others have shown that Jasplak can sometimes destabilize actin [74], [99], [100]. The disparities in Jasplak's effects appear to be dependent on the cell type and concentration of Jasplak. These contradictory studies may explain the lack of effect of Jasplak on cellular bioeffects in our study.

3.4.3 Plasma membrane fluidity did not affect intracellular uptake or cell viability

Cholesterol is critical to the dynamic stability and fluidity of the plasma membrane [83], [84], [101]. To evaluate the effect of membrane fluidity in TNET, we used MβCD to increase the fluidity of the membrane and WSC to decrease the fluidity of the membrane. Overall, cells treated with these plasma membrane fluidity-altering compounds showed no significant difference in intracellular uptake or viability loss compared to non-treated cells (**Figure 3.7** and **Figure 3.8**).

Previous studies have shown that the addition of MβCD and WSC not only influences lipid bilayer stiffness [102] but also can affect cellular mechanotransduction properties [89]. Interestingly, some studies have shown that MβCD can lead to cell

stiffening, while WSC can increase cell elasticity [76], [101], [103]. Other investigations argue that these effects are cell-type dependent and are not strongly coupled [102]. These observations illustrate the complexity of analyzing our data. Nevertheless, our data did not suggest any significant effect of treatment with MβCD and WSC on intracellular uptake or viability, which supports the interpretation that cell membrane fluidity does not play a significant role in uptake and viability in TNET. This data suggests that a thermal mechanism in TNET is not dominant. Other laser-mediated techniques have shown that a thermal mechanism via local heat can increase membrane permeability [104]. However, without a direct assay of possible lipid phase transitions a thermal mechanism cannot be definitively ruled out.

3.5 Conclusion

In this study, we investigated the role of cytoskeletal mechanics and plasma membrane fluidity on resulting bioeffects from TNET. We showed that destabilizing actin in the cytoskeleton using Latrunculin A led to greater intracellular uptake and less cell viability loss compared to non-treated cells. This suggested that the cytoskeletal effects of LatA may facilitate cell membrane permeabilization caused by TNET that allows greater uptake of molecules. It also suggested that LatA may affect the cytoskeleton in ways that enable cells to more easily recover from the effects TNET We also demonstrated that rigidifying the cytoskeleton with Jasplakinolide had no significant effect on uptake and viability, and found that plasma membrane fluidity did not play a significant role in bioeffects of TNET because neither treatment with MβCD to increase membrane fluidity nor treatment with WCS to decrease membrane fluidity significantly altered uptake or cell viability. We conclude that TNET offers a novel approach to loading molecules into cells

and that cytoskeletal weakening can increase intracellular uptake while reducing loss of cell viability.

CHAPTER 4. EFFECT OF LASER FLUENCE, NANOPARTICLE CONCENTRATION AND TOTAL ENERGY INPUT PER CELL ON PHOTOPORATION OF CELLS

4.1 Introduction

During TNET, CB nanoparticles strongly absorb NIR laser energy and are heated to temperatures that can exceed 1000ºC within nanoseconds. This thermal energy is then transferred to the surrounding aqueous medium, which vaporizes water and generates gas bubbles that grow on a time scale on the order of 100 ns and achieve a radius of up to 1 μm [23]. The sudden growth of the bubble emits acoustic waves and generates local fluid flow that can impart mechanical stresses to neighboring cells. Heat transfer to cells from hot bubbles also occurs. By mechanisms that are not yet fully understood, these mechanical and thermal stresses lead to photoporation. Photoporation, which leverages pulsed laser light to induce membrane poration [105], is believed to involve the creation of transient pores in cell membranes through which extracellular molecules can access the cytosol.

Many parameters are expected affect the efficiency of photoporation by TNET. Increasing laser fluence, and number of laser pulses directly increases cumulative energy input into the system. Increasing CB nanoparticle concentration should also increase the energy input, because more nanoparticles should absorb more laser energy. Increasing cell concentration may not affect energy input, but could affect photoporation because the

cumulative energy input is divided up among more cells. Very high CB nanoparticle or cell concentration could reduce cumulative energy input due to laser light scattering and shielding/shadowing of CB nanoparticles. However, the effects of many of these parameters have not been studied in detail before.

The purpose of this work was to evaluate the effects of laser fluence, laser pulse length, CB nanoparticle concentration and cell concentration on cellular bioeffects, i.e., intracellular uptake, loss of cell viability and cell fragmentation. We hypothesize that the effects of these four different parameters on photoporation can be explained by the cumulative energy input per cell that they generate, which we predict determines the resulting bioeffects.

4.2 Methods

4.2.1 Nanoparticle preparation

As previously described [14], CB nanoparticles (Black Pearls 470, Cabot, Boston, MA) were added to deionized water and 0.013% (v/v) Tween-80 (Sigma-Aldrich, St. Louis, MO) to make a stock concentration of 0.4 g/L. The solution was sonicated for 35 min in an ultrasonic water bath, followed by further mixing using an ultrasonic needle for 1 min (Sonics Ultracell, Sonics & Materials, Newton, CT). According to the manufacturer, CB nanoparticles had a primary particle size of 25 nm, but even after ultrasound treatment described above, the particles were aggregates measuring 201 ± 6 nm in size with a dispersity of 0.15 ± 0.04 nm (n=10), as determined by dynamic light scattering (ZetaSizerNano, Malvern Instruments, Lavern, Worcestershire, UK). In some cases, CB nanoparticle solutions were further diluted with deionized water.

4.2.2 Laser system for in vitro exposures

A Nd:YAG solid-state laser (Powerlite II Plus, Continuum, San Jose, CA) was used to apply pulses of 1064 nm wavelength with 5-9 ns pulse length to cell samples. The pulses were applied at a frequency of 10 Hz (i.e., 10 pulses per second). Laser pulse energy was varied by changing the amplifier voltage settings. The initial 12 mm beam from the laser was passed through an 8 mm aperture and then through a diverging lens (*f = 50 cm*) (ThorLabs, Newton, NJ) to illuminate the entire exposure area of the Pyrex cuvette (4 cm^2).

4.2.3 Cell culture and laser exposure experiments

Human prostate cancer cells (DU145, American Type Culture Collection, Manassas, VA) were cultured as monolayers in a humidified atmosphere of 95% air and 5% CO_2 at 37°C in RPMI-1640 medium (Cellgro, Herndon, VA) supplemented with 100 g/mL penicillin-streptomycin (Cellgro) and 10% (v/v) heat inactivated fetal bovine serum (Corning, Palo Alto, CA). Cells were harvested for experiments at 80% confluence by trypsin/EDTA (Cellgro) digestion, washed with serum and then re-suspended in RPMI. DU145 cells were used in this study because they have been extensively used and characterized in previous intracellular delivery studies as a model mammalian cell [13], [14], [20].

Harvested cells were stored in 1.5 mL microcentrifuge tubes on ice and then transferred to Pyrex glass cuvettes (37-PX-2, Starna Cells, Atascadero, CA) for laser exposure. Exposed cuvettes contained 520 μL of cells suspended, CB nanoparticles at specified concentrations and 10 μM. high-purity calcein (Molecular Probes, Eugene, OR).

'Sham' samples contained cells, CB nanoparticles, and calcein that underwent the same experimental conditions except without laser exposure.

Following laser exposure, samples were transferred back into the microcentrifuge tubes with a transfer pipette and stored on ice to reduce uptake due to endocytosis until all samples were exposed (i.e., up to 30 min). To label non-viable cells post-exposure, propidium iodide (PI; Invitrogen, Grand Island, NY) was added at a concentration of 13.4 μM and incubated with cells for 10 min to stain non-viable cells. Samples were washed at least 3 times to remove excess fluorescence from the bulk solution before analysis by flow cytometry.

4.2.4 Viscosity experiments

Carboxyl methylcellulose (CMC; 90 kDa, low-viscosity, Sigma Aldrich, St. Louis, MO) was added to some cell samples to increase viscosity. CMC was added to RPMI and placed in an ultrasonic water bath for 1 h before addition to cell samples at a final concentration of 2% CMC. The viscosities of the solution with and without 2% CMC were determined to be 16.9 ± 0.6 cP and 1.30 ± 0.02 cP, respectively, using a viscometer at 25ºC (Brookfield DV2T, Brookfield AMETEK, Middleboro, MA).

4.2.5 Data collection and processing

A bench-top flow cytometer (BD Accuri, BD Biosciences, San Jose, CA) quantified bioeffects in terms of viable cells with intracellular uptake of calcein (i.e, percentage of cells with intracellular calcein and lacking PI staining), non-viable cells (i.e., percentage of intact cells with PI staining) and fragmented cells (see below). Calcein uptake was

measured by green fluorescence of cells (530/28 nm bandpass filter) and loss of cell viability was measured by red fluorescence of PI (670 nm longpass filter).

Samples were run at a constant flow rate of 35 μL/min for 1 min. A 'cells-only' negative control was used to construct a cell population gate based on forward-scatter and side-scatter intensities. Cells within this gate were considered intact cells. To account for possible cell loss due to cell fragmentation (appearing as a field of very low forward- and side-scattering events on the flow cytometer), the number of PI-negative cells collected from a given sample was subtracted from the number of PI-negative cells in 'sham' negative control samples. Next, this difference was subtracted from the number of PI-positive cells and that result was taken to be the number of cells that were lost due to cell fragmentation [80].

4.2.6 Statistical Analysis

A minimum of three replicates was used for all conditions which enabled calculation of means and standard deviations. The null hypothesis was that the average percentage of cells exhibiting uptake, viability loss or fragmentation between a sham sample and an exposed sample were equal. The equality of means response between exposed samples and sham samples was tested with ($\alpha = 0.05$). The equality of mean response was tested with 1-way or 2-way, followed by post hoc Tukey's pairwise comparison using GraphPad Prism 6 (GraphPad Software, La Jolla, CA).

4.3 Results and Discussion

4.3.1 Effects of CB nanoparticle concentration

Previous studies with laser-activated CB nanoparticles showed differences in bioeffects (i.e. uptake and viability loss) when the nanoparticle concentration was altered [23], [72]. To study the effect of energy input via CB nanoparticles, we surveyed a comprehensive range of nanoparticle concentrations (i.e. 0.05 mg/L to 157 mg/L) *in vitro* and quantified the resulting bioeffects with increasing laser fluence (**Figure 4.1**). At low CB nanoparticle concentrations (i.e. $\leq$ 0.39 mg/L), exposed cells showed minimal uptake, almost no viability loss and no fragmentation (**Figure 4.1a-c**). At intermediate concentrations (i.e. 3.1 – 10 mg/L), uptake increased significantly and then plateaued, viability loss was minimal and no significant fragmentation occurred (**Figure 4.1d-f**). At higher concentrations (i.e. 15 – 20 mg/L), uptake also plateaued with increasing laser fluence and fragmentation was minimal, but non-viable cells increased and plateaued with increasing laser fluence (**Figure 4.1g-h**). At even higher concentrations (i.e. 25 – 157 mg/L), uptake peaked and then decreased, non-viable cells peaked and decreased and fragmentation increased significantly for 100 and 157 mg/L (**Figure 4.1i-k**). Overall, as CB nanoparticle concentration increased, cellular bioeffects became increasingly stronger.

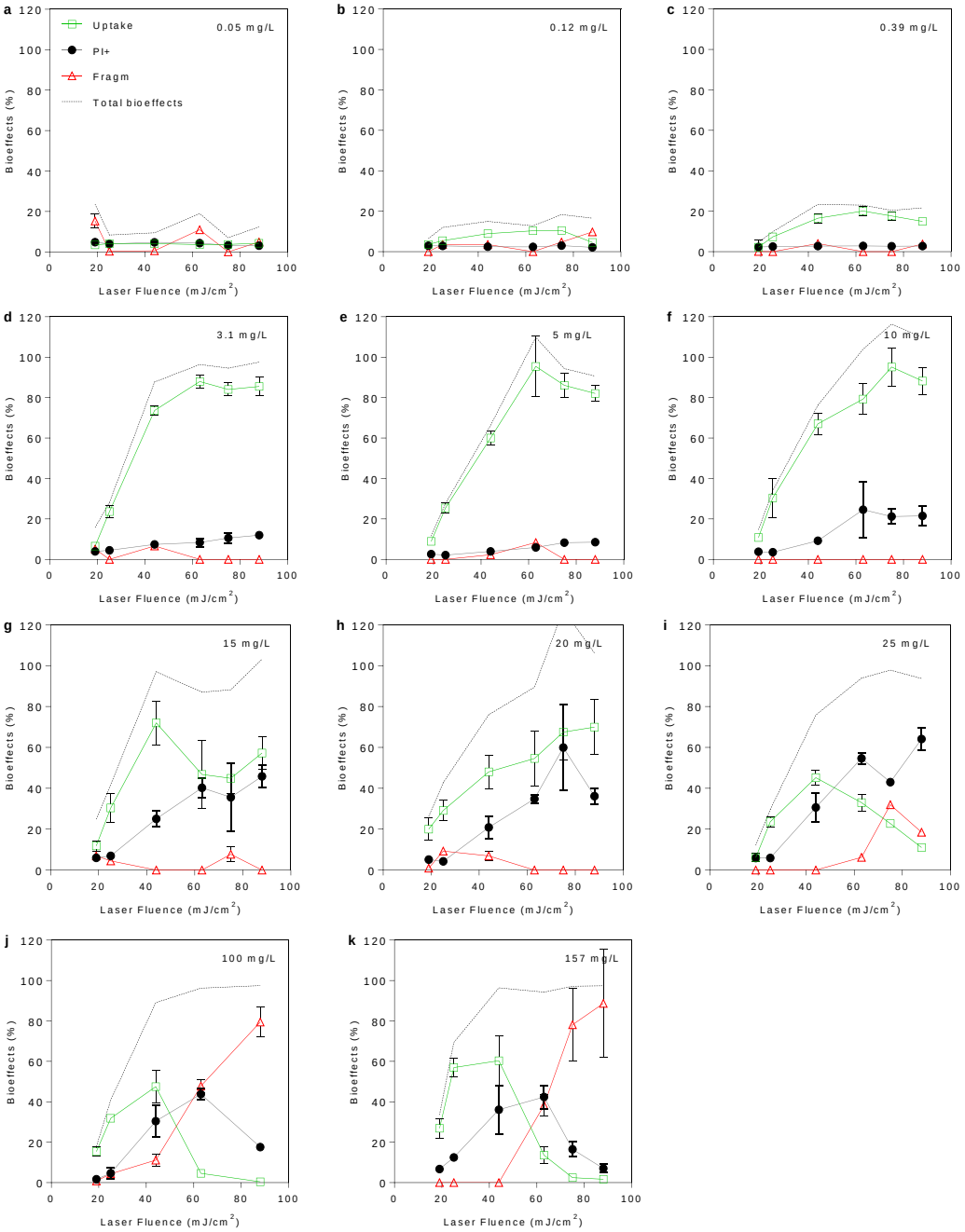

Figure 4.1: Percentage of cells with intracellular uptake, non-viable cells (intact, PI+), fragmented cells (i.e. cells loss) after 600 pulses of exposure to laser fluence ranging from 19 – 88 mJ/cm^2 with CB nanoparticle concentrations ranging from a) 0.05 mg/L, b) 0.12 mg/L, c) 0.39 mg/L, d) 3.1 mg/L, e) 5 mg/L, f) 10 mg/L, g) 15 mg/L, h) 20 mg/L, i) 25 mg/L, j) 100 mg/L, and k) 157 mg/L. Total bioeffects (--) are also shown. Data show average ± SD (n=3).

4.3.2 Effect of laser fluence

Laser energy was also used to increase the total energy input to the system. As such, we took all the data from **Figure 4.1** and separated bioeffects based on laser fluence (**Figure 4.2**). At the lowest laser fluence, 19 mJ/cm^2, little bioeffects – uptake, non-viable cells, and fragmentation – were observed for all CB concentrations evaluated (**Figure 4.2a**). Bioeffects steadily increased with laser fluence, where at 25 mJ/cm^2, little bioeffects were observed for dilute CB concentrations (i.e. < 1 mg/L), but significant uptake was seen at concentrations above that threshold (**Figure 4.2b**). Like the 19 mJ/cm^2 data, minimal viability loss and fragmentation was observed for all concentrations at 25 mJ/cm^2. At an intermediate laser fluence of 44 mJ/cm^2, significant bioeffects were observed for CB concentrations > 1 mg/L, as uptake increased and plateaued with increasing CB concentration (**Figure 4.2c**). Total bioeffects saturated at higher laser fluence (i.e. 63 – 88 mJ/cm^2) for all CB concentrations tested (**Figure 4.2d-f**).

We also estimated the effective CB-CB spacing and number of CB nanoparticles per cell. At the lowest laser fluence (i.e. 19 mJ/cm^2), higher CB per cell values (i.e. > 1 E+4) did not increase bioeffects greatly compared to lower CB per cell values. At 44 mJ/cm^2, we saw that bioeffects saturated at CB per cell values ≥ 1.7 E+3 and when the CB-CB spacing was shorter than the radius of cell (10 μm). At even higher laser fluence (i.e. 63 – 88 mJ/cm^2), total bioeffects saturated at CB per cell values ≥ 5.5 E+3, suggesting that increasing the number of particles near the cell has a limiting effect.

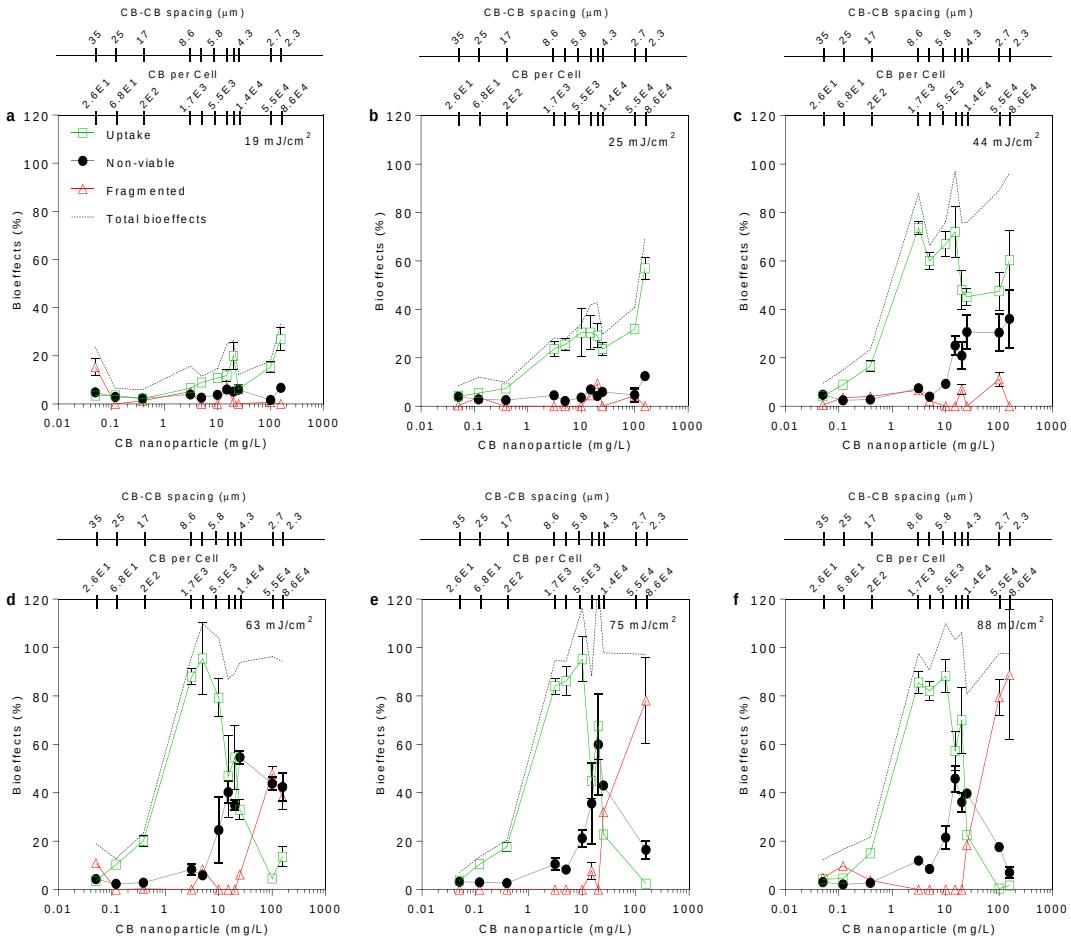

Figure 4.2 Percentage of cells with intracellular uptake, non-viable cells (intact, PI+), fragmented cells (i.e. cells loss) after 600 pulses of exposure to laser fluence ranging from a) 19 mJ/cm^2 b) 25 mJ/cm^2, c) 44 mJ/cm^2, d) 63 mJ/cm^2, e) 75 mJ/cm^2 and f) 88 mJ/cm^2 with CB nanoparticle concentrations ranging from 0.05 – 157 mg/L shown on the lower x axis. The first upper x axis shows the corresponding CB-CB spacing (i.e., from the center of each CB nanoparticle to its neighboring CB nanoparticle, assuming a cubic lattice) and the second upper x-axis shows the corresponding number of CB nanoparticles per cell. Total bioeffects (--) are also shown. Data show average ± SD (n=3).

4.3.2.1 Bioeffect zones due to CB nanoparticle concentration and laser fluence

From **Figure 4.1** and **Figure 4.2**, we noticed distinct regions or zones of bioeffects dependent on CB nanoparticle concentration and laser fluence. These thresholds were divided into different zones dependent on laser fluence with increasing CB concentration

(**Figure 4.3**) and dependent on CB concentration with increasing laser fluence (**Figure 4.4**). In evaluating cells with intracellular uptake, three distinct zones emerged. The first zone for samples exposed to 19 and 25 mJ/cm^2, with a few exceptions at high CB concentrations (i.e. ≥ 100 mg/L), exhibited low uptake with a few exceptions at CB concentrations > 100 mg/L (**Figure 4.3ai**). The next zone showed uptake plateaued at 44 mJ/cm^2, uptake increased and plateaued with increasing CB concentration (**Figure 4.3aii**) and finally in the last zone, uptake peaked and then decreased at higher fluence (i.e. 63 – 88 mJ/cm^2), uptake peaked and then decreased with increasing CB concentration (**Figure 4.3aiii**). Viability loss (i.e. non-viable cells) was also divided into three zones of behavior. At low laser fluence (19 – 25 mJ/cm^2), the viability loss was minimal (**Figure 4.3bi**). In the second zone, viability loss plateaued at 44 mJ/cm^2 (**Figure 4.3bii**) and peaked, then decreased in the third zone at high laser fluence (i.e. 63 – 88 mJ/cm^2) (**Figure 4.3biii**). Fragmentation occurred into two distinct zones (**Figure 4.3ci-cii**). The first zone, from 19 – 44 mJ/cm^2 (**Figure 4.3ci**), showed no fragmentation, in contrast to the second zone at higher laser fluence (i.e. 63 – 88 mJ/cm^2), where significant fragmentation occurred (**Figure 4.3cii**).

Like the laser fluence zones, there were transition zones of bioeffects dependent on CB concentration with increasing laser fluence (Figure 4.4). Uptake behavior was divided into three zones, as well, with the first zone of low CB concentrations (i.e. 0.05 – 0.39 mg/L) showing minimal uptake (**Figure 4.4ai**). In the second zone, uptake increased and plateaued with higher concentrations (i.e. 3.1 – 20 mg/L) (**Figure 4.4aii**), and at even higher concentrations (i.e. 25 – 157 mg/L), uptake peaked and then decreased in the third

zone (**Figure 4.4aiii**). Viability loss (**Figure 4.4b**) and fragmentation (**Figure 4.4c**) were also divided into two and three zones, respectively.

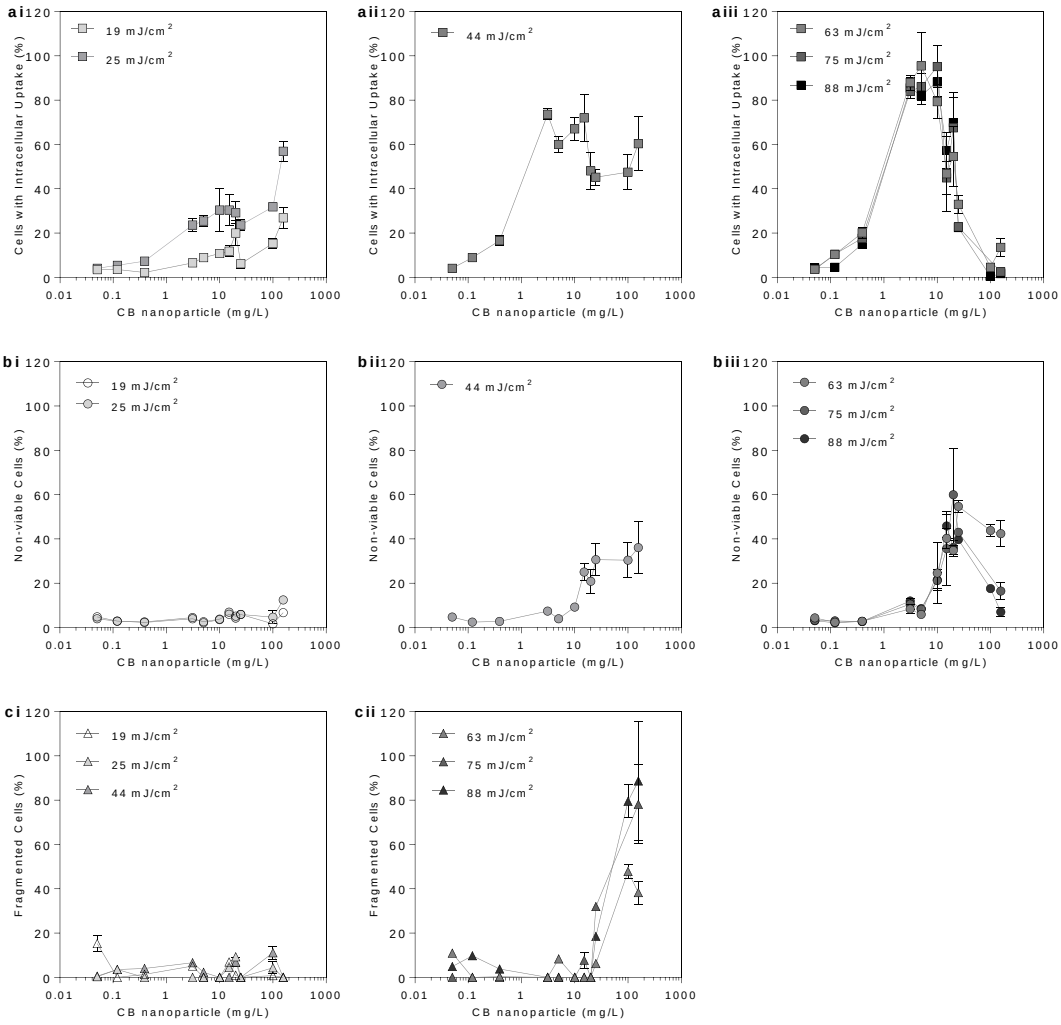

Figure 4.3: Bioeffects and thresholds as a result of varying CB nanoparticle concentration and increasing laser fluence. Percentage of cells with thresholds of intracellular uptake (ai – aiii) in which (ai) in Zone I little to no uptake occurs with increasing laser fluence. (aii) In Zone II, uptake plateaus and in (aiii) Zone III, uptake drops. Percentage of cells with thresholds of non-viable cells (bi-biii) in which (bi) in Zone I little to no cells exhibit non-viable cells. (bii) In Zone II, percentage of non-viable cells plateaus with increasing laser fluence and (biii) Zone III, non-viable cells peak and then decrease with increasing laser fluence. Percentage of cells with thresholds of fragmentation (ci-cii). (ci) In Zone I little to no fragmentation occurs with increasing laser fluence. (cii) At higher CB concentration, fragmentation increases with increasing laser fluence. Data show average ± SD (n=3).

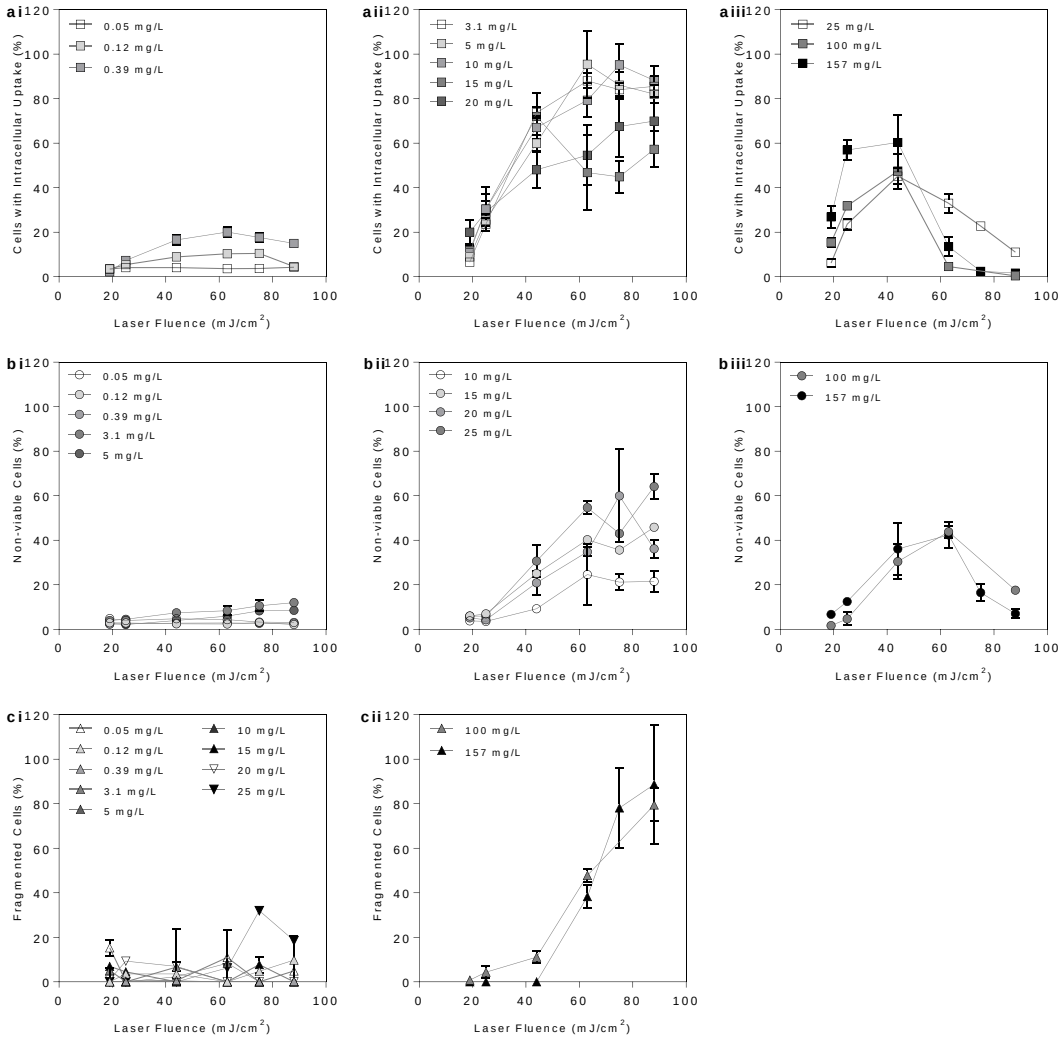

Figure 4.4: Bioeffects and thresholds as a result of varying laser fluence and increasing CB concentration. Percentage of cells with thresholds of intracellular uptake (ai – aiii) in which (ai) in Zone I (19-25 mJ/cm^2) little to no uptake occurs with increasing CB concentration. (aii) In Zone II, uptake plateaus (44 mJ/cm^2) and in (aiii) Zone III, uptake drops (63-88mJ/cm^2). Percentage of cells with thresholds of non-viable cells (bi-biii) in which (bi) in Zone I (19-25 mJ/cm^2) little to no cells exhibit non-viable cells. (bii) In Zone II (44 mJcm^2), percentage of non-viable cells plateaus with increasing laser fluence and (biii) Zone III (63-88 mJ/cm^2), non-viable cells peak and then decrease with increasing CB concentration. Percentage of cells with thresholds of fragmentation (ci-cii). (ci) In Zone I (19-44 mJ/cm^2) little to no fragmentation occurs with increasing CB concentration. (cii) At high laser fluence (63-88mJ/cm^2), fragmentation increases with increasing CB concentration. Data show average ± SD (n=3).

4.3.3 Bioeffect zones depend on laser input energy and vaporization sites surrounding the cell

Overall, we posit that the bioeffect transition zone trends in **Figure 4.3** and **Figure 4.4** highlight the importance of input energy and vaporization sites surrounding the cell, and more broadly the short-range interactions which drive TNET.

Our analysis reveal that laser fluence and CB concentration correlate strongly with bioeffects. In terms of laser fluence, we saw that low laser fluence (i.e. 19 – 25 mJ/cm^2) resulted in minimal bioeffects for most CB concentrations (**Figure 4.3ai, bi, ci**), whereas bioeffects increased linearly with higher fluence (i.e. ≥ 44 mJ/cm^2) (**Figure 4.3biii**). This suggests that total input energy, by way of laser fluence correlates with bioeffects.

Similarly, we saw that CB concentration correlated with bioeffects. Our previous estimations indicated that upon laser exposure, the CB nanoparticles heat up to hundreds of degrees Celsius and results in vaporization (**Appendix B**). Thus, we can think of nanoparticles as nucleation sites for vaporization. At lower nanoparticle concentrations, even when we increased fluence (**Figure 4.4ai-ci**), there were not enough nanoparticles/bubbles present to induce strong cellular bioeffects. At higher concentrations, more nanoparticles can absorb more laser energy, leading to the formation of more bubbles surrounding a cell. Therefore, a major conclusion from this set of studies is that energy input via CB nanoparticle concentration and more broadly the number of bubbles, is also a guiding parameter in determining the magnitude of bioeffects.

4.3.4 Total energy input per cell

4.3.4.1 <u>CB nanoparticle concentration & Laser fluence</u>

CB nanoparticles strongly absorb in the NIR [106], [107]. Calculations reveal that the percent absorbed at any given laser fluence is strongly dependent on the number of nanoparticles (i.e. the concentration). Based on Mie scattering theory used in our previous analysis [23], we can predict the total energy absorbed per pulse (Q_{in}) by any concentration of CB nanoparticles and then estimate the total energy input per cell (***Appendix B***). The transition zones shown in **Figure 4.3** and **Figure 4.4** can be explained by the differences in energy input per cell (**Figure 4.5**).

The lack of bioeffects when the CB nanoparticle concentration is low (i.e. < 1 mg/L) at laser fluence ≥ 44 mJ/cm^2, is due to the relatively lower amount of energy input at those concentrations (**Figure 4.5a**). That is when little energy is absorbed, little energy is transduced to surrounding cells, resulting in little to no bioeffects. For comparison, even at the highest laser fluence used in this study, 88 mJ/cm^2, the Q_{in} for a nanoparticle concentration of 0.39 mg/L (2.7 x 10^{-1} mJ/pulse) is still only ~25% of the energy absorbed for a nanoparticle concentration of 3.1 mg/L at 44 mJ/cm^2, where 1.09 mJ/pulse of energy is absorbed (**Appendix B**). Once sufficient laser energy is absorbed at or above the laser fluence threshold (i.e. 44 mJ/cm^2) by higher nanoparticle concentrations (i.e. between 1 and 100 mg/L), significant uptake, increase in viability loss and no fragmentation occurred (**Figure 4.5a-c**).

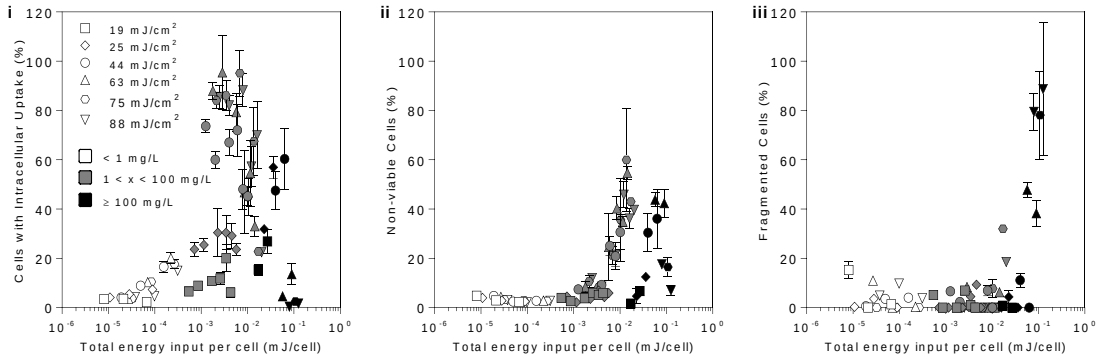

Figure 4.5: Total energy input per cell (mJ/cell) for a) cells with uptake, b) non-viable cells, and c) fragmented cells dependent on laser fluence and CB nanoparticle concentration data from Figure 4.3 & **Figure 4.4.**

The importance of energy input per cell is especially highlighted at high CB concentrations. High CB concentrations exhibited higher energy absorption, but only showed significant bioeffects at high laser fluence (i.e. 63 – 88 mJ/cm^2) (**Figure 4.5b-c**). That is, the number of particles (concentration) in conjunction with the amount of energy they absorb (laser fluence dependent), are critical to the overall energy input per cell. Moreover, it is interesting to note that at higher nanoparticle concentrations (i.e. ≥ 25 mg/L), the total energy absorbed dwarfs the energy absorption of lower concentrations for the same laser fluence. For example, at 44 mJ/cm^2, the total energy absorbed for 157 mg/L is 55 mJ/shot, meaning there is a ~4900% increase in energy absorbed, compared to 1.1 mJ/pulse for 3.1 mg/L. In the same way, when the CB nanoparticle concentration is lower, fragmentation does not occur, even at very high laser fluence (i.e., 63 – 88 mJ/cm^2). Again, this can be attributed to the relatively low magnitude of total energy input per cell at those given concentrations (i.e. < 1 mg/L) (**Figure 4.5c**).

4.3.4.2 Laser pulses & Cell concentration

We also explored two other experimental parameters which affect cellular bioeffects – laser pulses and cell concentration. When these parameters were normalized for total energy input per cell, it also showed a strong correlation with energy and bioeffects. First, as the number of laser pulses increases, the total energy input per cell increases – however, the magnitude of bioeffects was strongly related to the CB nanoparticle concentration and the laser fluence (**Figure 4.5**). As such, we tested higher CB concentrations (i.e. 25 & 157 mg/L). We saw that as the number of pulses increased, bioeffects became stronger (**Figure 4.6a**). The apparent shielding effect of bubbles at high CB nanoparticle concentration supports the idea of direct cell-bubble interaction that can occur over a distance (and can be blocked by the presence of other bubbles in between).

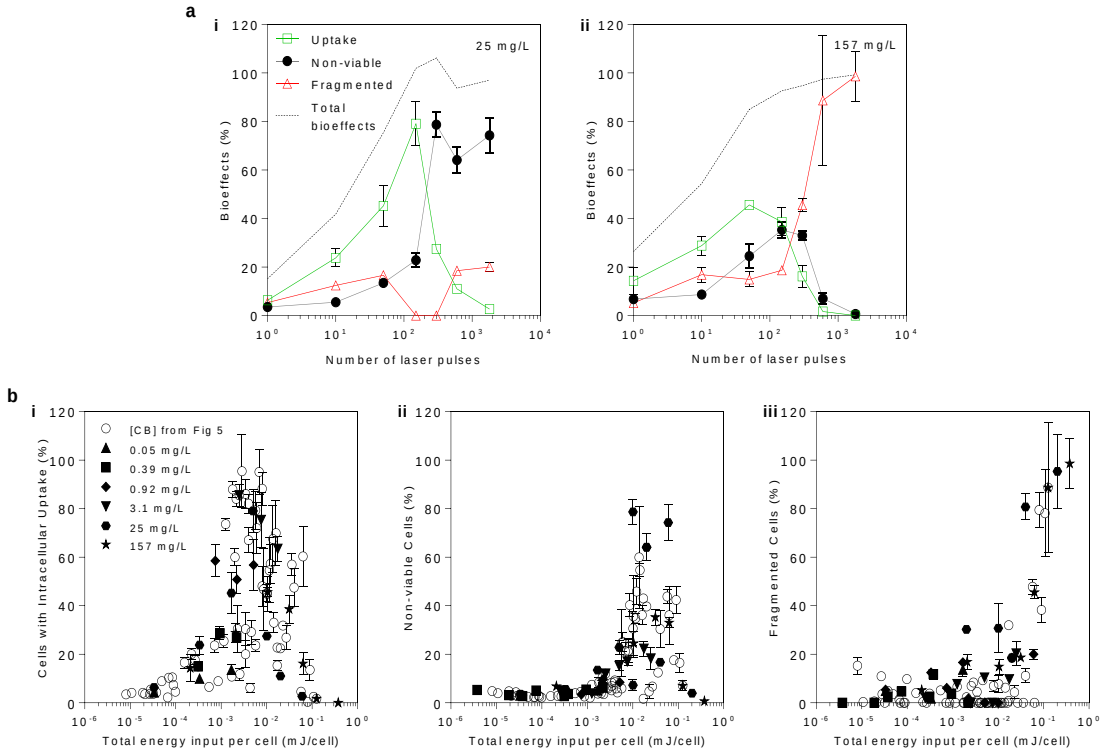

Figure 4.6: a) Cells exposed to 1 – 1800 laser pulses at 88 mJ/cm^2 with ai) 25 mg/L and aii) 157 mg/L CB particle concentration. Data shows percentage of cells with intracellular uptake, non-viable cells, fragmented cells and total bioeffects. b) Total energy input per cell (mJ/cell) for bi) cells with uptake, bii) non-viable cells, and bii) fragmented cells dependent on laser pulses and CB concentration. Single shot mode was used for pulses ≤ 50, exposed manually at 1 shot every 5 secs. Pulses ≥ 150 were exposed at a frequency of 10 shots/sec. Data show average ± SD (n = 3).

Cell concentration was varied to better understand these direct interactions. We saw total energy input per cell decreased linearly with increasing cell concentration, because the total input energy was divided among more cells (**Figure 4.7b**). For example, at 25 mg/L, there was a decrease in bioeffects above 10^6 cells/mL (**Figure 4.7a(iii)**). Based on the cell-cell spacing at this point, there seems to be a protective effect of higher cell concentrations, decreasing overall effects of TNET. Since cellular bioeffects became weaker with increasing cell concentration (i.e. closer cell-cell spacing) (**Figure 4.7b**), this

once again suggests that there are direct interactions between cells and neighboring bubbles, as opposed to a change in the overall environment around the cells (e.g. elevating pressure), which would not be significantly affected by cell concentration.

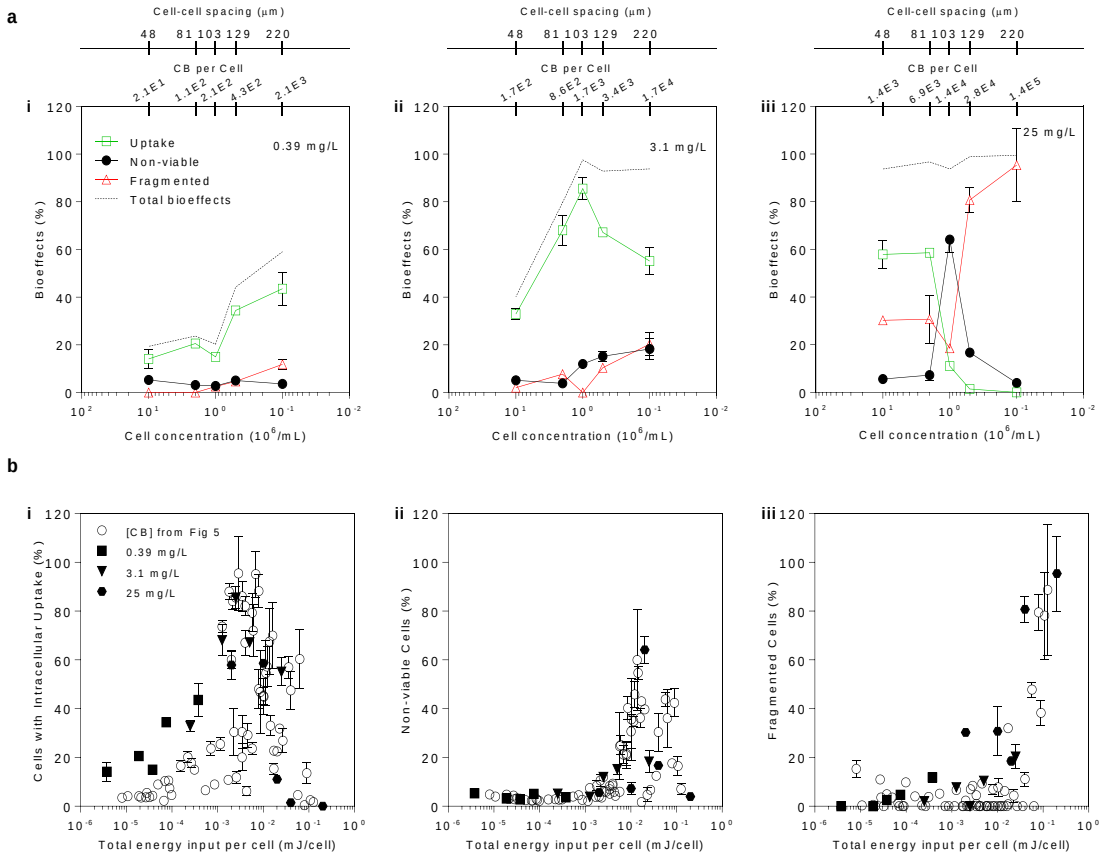

Figure 4.7: a) Percentage of cells with intracellular uptake, non-viable cells, and fragmented cells exposed with ai) 0.39 mg/L CB, aii) 3.1 mg/L CB and aiii) 25 mg/L CB. Cell concentration was varied from 0.1, 0.5, 1.0, 2.0 and 10 x 10^6 cells per mL (*lower x-axis)* and the corresponding cell-cell spacing (i.e., from the center of each cell to its neighboring cells, assuming a cubic lattice) is shown on the *upper x-axis* and the corresponding number of CB nanoparticles per cell is shown in the *second upper x-axis*. Data also shows total bioeffects. Samples were exposed for 600 pulses at 88 mJ/cm^2. Data show average ± SD (n=3). b) Total energy input per cell (mJ/cell) for bi) cells with uptake, bii) non-viable cells, and biii) fragmented cells dependent on cell concentration and CB nanoparticle concentration.

4.3.5 Dampening short-range interactions with medium viscosity

Previous studies indicated that CMC aqueous solutions retain nearly similar thermal properties (e.g. heat capacity, thermal conductivity) as pure water [108]. Thus, to dampen local fluid mechanics energy transfer from irradiated CB nanoparticles while maintaining similar thermal properties, we increased the viscosity of the suspension medium (i.e. serum-free RPMI) nearly 13-fold compared with 2% CMC (**Methods**). Samples were exposed with 3.1 mg/L CB because this nanoparticle concentration had previously shown efficacious delivery (Figure 4.1). With a more viscous medium, intracellular delivery of calcein to the cells was significantly reduced (**Figure 4.8a**). Due to a higher viscosity, some cells were lost in sample transfer during experiments (data not shown). That withstanding, viability loss was similar for 0% CMC and 2% CMC samples at both 44 and 88 mJ/cm^2 (**Figure 4.8b**).

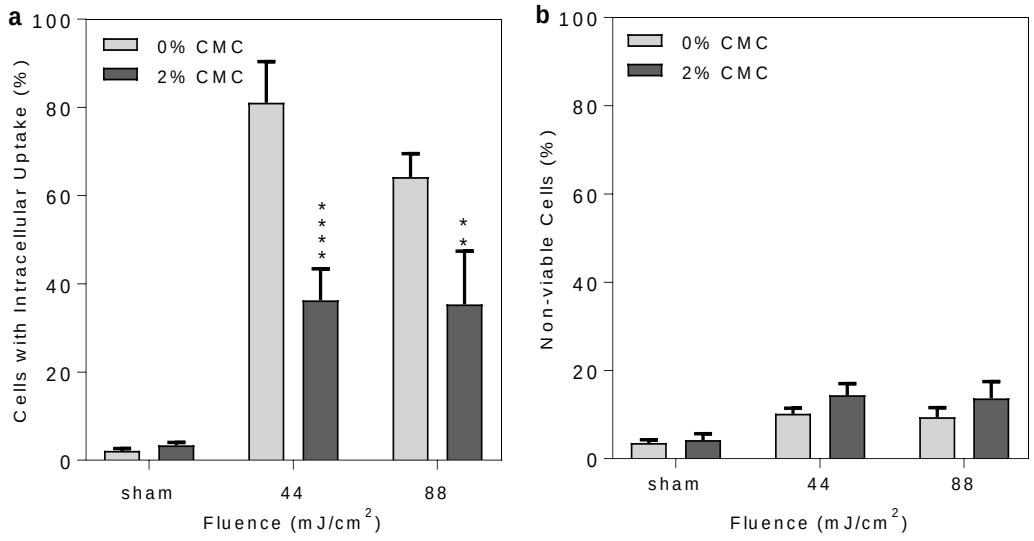

Figure 4.8: a) Cells with uptake and b) non-viable cells in suspension with 0% and 2% CMC (w/v) + RPMI, exposed to 44 mJ/cm^2 and 88 mJ/cm^2 for 600 pulses minute with 3.1 mg/L CB concentration. Asterisk (*) indicate data is statistically different from other condition (ANOVA, **p < 0.01, ****p<0.0001). Data show average ± SD (n=3).

Other work using microbubbles for sonoluminescence applications have shown that increasing the viscosity of the liquid drastically reduces the bubble's ability to expand [109]. It is possible that the timescale of the bubble growth rate was decreased significantly enough to suppress bioeffects. Since the growth rate of the bubble should be reduced in a more viscous medium, the resulting vapor bubble velocity and acceleration may have resulted in less short-range energy transfer in the form of local fluid displacement and/or near-field pressure release.

In addition, being that the thermal properties of the medium were relatively unaltered with the addition of CMC, these results have some implications for TNET mechanistically. The results seem to point to a fluid mechanical method rather than a thermal mechanism which leads to poration of the membrane and subsequent molecular delivery. Had a thermal mechanism been dominant in TNET, we would have expected to see little to no significant change in bioeffects upon the addition of CMC, however we saw that bioeffects were significantly dampened. This dampening again supports a possible hindrance of fluid mechanical energy transfer from bubble to cell upon laser irradiation of the carbon nanoparticles.

4.3.6 Implications of these various parameters

This study examined the effect of four experimental parameters – laser fluence, number of laser pulses, CB nanoparticle concentration, and cell concentration – on cellular bioeffects, including intracellular uptake of molecules, loss of cell viability (in intact cells) and cell fragmentation.

For increasing laser fluence, number of pulses and CB nanoparticle concentration, and for decreasing cell concentration, cellular bioeffects became increasingly stronger. At the weakest exposure conditions, no significant effects on cells were seen. As exposure conditions became stronger, (i) significant intracellular uptake was seen and increased, (ii) then loss of cell viability began to occur and increased, while intracellular uptake correspondingly decreased and (iii) finally at the strongest exposure conditions, cell fragmentation was observed and increased, while intracellular uptake and loss of cell viability decreased (**Figure 4.3** & **Figure 4.4**).

The effects of these four parameters could be accounted for by correlation with a single parameter: total energy input per cell (**Figure 4.5**, **Figure 4.6b**, **Figure 4.7b**). These parameters increased linearly with laser fluence and number of laser pulses, as well as with CB nanoparticle concentration, because more nanoparticles were able to absorb more laser light. It decreased linearly with cell concentration because the energy needed to be divided up among more cells. While all the data fell onto a single curve when plotting each of the bioeffects versus total energy input per cell (**Figure 4.5**), the data at the highest CB nanoparticle concentrations ($\geq$100 mg/L) were shifted to higher energy to achieve the same bioeffects. We believe this is due to bubbles created around CB nanoparticles shielding [23] the interactions between neighboring cells and more-distant bubbles.

Overall, these data, in context with the broader literature, suggest that each laser pulse administers a certain amount of energy into each nanoparticle. Each nanoparticle transduces that energy into thermal, fluid mechanical and acoustic energy emissions that are transmitted to neighboring cells. The cumulative energy transmitted to cells determines the cellular bioeffects, and it does not matter what combination of laser fluence, number of

laser pulses, CB nanoparticle concentration or cell concentration values together determine that cumulative energy transmitted to each cell.

Understanding bioeffect transition zones in addition to the magnitudes of total energy input per cell is imperative for future TNET applications. Future studies to detail the type of energy transduction associated with short-range interactions, i.e. mechanical and/or thermal stresses, is warranted and moreover, understanding the magnitude of the energy transduced will be instructive to further developing TNET into a promising intracellular drug delivery platform.

4.4 Conclusion

In this study, we investigated four parameters – CB nanoparticle concentration, laser fluence, laser pulses, and cell concentration – which influence short-range cell–CB nanoparticle interaction and resulting bioeffects. The results from this work provide an important theoretical framework to understand short-range cell–CB nanoparticle interactions in TNET. Our results revealed total energy input per cell correlates strongly with cellular bioeffects. These results provide a deeper fundamental biophysical understanding for TNET.

CHAPTER 5. EFFECTS OF NANOSECOND-PULSED LASER IRRADIATION OF CARBON NANOTUBES ON INTRACELLULAR UPTAKE AND CELL VIABILITY, AND THEIR RELATIONSHIP TO PHOTOACOUSTIC PRESSURE

5.1 Introduction

Previously, we investigated the long-range acoustics associated with a pressure field produced by laser-irradiated CB nanoparticles and its role in intracellular delivery [23]. We found that the laser-irradiated CB nanoparticles were heated to more than 1000 K and generated vapor bubbles that rapidly expand and release acoustic waves [23]. Two length scales of cell-bubble interaction were hypothesized: 1) long-range, indirect, cumulative acoustic emissions from bubbles or 2) short-range, local cell-bubble interaction. Several calculations and experiments suggested that a cell only experiences pressure from the nearest CB particles due to a shielding effect from a cumulative field of carbon nanoparticles [23]. We further posited that observed bioeffects were due to possible fluid mechanical and/or thermal mechanisms, in which liquid momentum or direct heat transfer from the hot vapor bubble to the cell (i.e. short-range effects). This suggested that spatially cumulative acoustic interactions (i.e. long-range effects) were not the dominant mechanism of TNET's effects on cells.

While previous studies have characterized the photoacoustic properties of CB nanoparticles [15], [23], [69], [71], [110]–[112] and we have used CB nanoparticles extensively in our intracellular delivery work [13], [14], [23], [72], [73], use of carbon in

different forms, e.g., carbon nanotubes (CNT), has not been studied before in the context of intracellular delivery by TNET. Therefore, in this study we compared the cellular bioeffects, as well as the photoacoustic output, from CB nanoparticles, multi-walled CNTs (MWCNT) and single-walled CNTs (SWCNT). We hypothesized that TNET would occur differently in these three types of carbon nanoparticles and thereby have different effects on intracellular delivery and cell viability. We further hypothesized that the photoacoustic output from these three types of nanoparticles would be different, and assessed whether the diverse bioeffects from the different types of nanoparticles could be explained on the basis of photoacoustic pressure (i.e., whether bioeffects would correlate with photoacoustic pressure for all three types of nanoparticles.

5.2 Methods

5.2.1 Nanoparticle preparation

Three carbon nanoparticle materials were utilized in this study—CB, SWCNT, and MWCNT. CB nanoparticles were obtained from Cabot Corporation (Boston, MA) and prepared as previously described [14] with a stock concentration of 0.40 g/L. Per the manufacturer, the individual CB nanoparticles were 25 nm in diameter, but aggregated to form clusters of 200 nm diameter. We performed dynamic light scattering (DLS) measurements (ZetaSizerNano, Malvern Instruments, Lavern, Worcestershire, UK), which indicated that the CB nanoparticles (i.e., clusters) had a diameter of 200 ± 6 nm (n=10), which is similar to previous studies [13], [14].

SWCNT and MWCNT suspensions (Nanostructured & Amorphous Materials, Houston, TX) were diluted to stock concentrations of 1.056 g/L and 0.304 g/L,

respectively. Per the manufacturer, the individual SWCNT were 5-30 μm in length and 1-2 nm in diameter, whereas the individual MWCNT were 10-30 μm in length and 20-30 nm in diameter. DLS studies showed that SWCNT and MWCNT bundled into aggregates with diameters of 395 ± 20 nm (n=10) and 252 ± 23 nm (n=10), respectively. Although DLS is more accurate for spherical particles, previous studies have reported that CNT tend to curl-up and agglomerate [113], and aggregate size has been measured using DLS [113]–[115].

5.2.2 Laser system

Acoustic measurements and *in vitro* exposures were conducted with a Nd:YAG solid-state laser (Continuum Powerlite II Plus, San Jose, CA), which was used to apply 5-9 ns duration pulses of 1064 nm wavelength, at a frequency of 10 Hz (i.e., 10 pulses per second). Laser pulse energy was varied by changing the laser amplifier voltage settings.

For *in vitro* delivery experiments, the laser beam, with an initial diameter of 12 mm, was passed through an 8 mm aperture to obtain a more uniform laser energy profile. A diverging lens was positioned after the 8 mm aperture to illuminate the exposure area (4 cm^2) of the cuvette used to hold cells and nanoparticles in suspension. For photoacoustic measurements, the 12 mm laser beam was passed through a 2 mm aperture to minimize the spot size.

5.2.3 Acoustic measurements

Acoustic measurements of the three nanoparticle systems (i.e. CB, MWCNT, SWNCT) were conducted as described in previous work [23]. In brief, nanoparticle suspensions were pumped at a flow rate of 85 mL/h (New Era Pump Systems, Farmingdale,

NY) as a stable vertical stream from a 'supply' needle into a glass-walled tank filled with degassed water at 22 ± 2 ºC. As the laser system irradiated a small section of the stream, a needle hydrophone (HNC-0200, ONDA, Sunnyvale, CA) received the photoacoustic signal. Before and after laser exposures, a focused ultrasound transducer (Panametrics V310-SU, Olympus) connected to a pulse receiver (Panametrics 5072PR, Olympus) was used to estimate the position of the hydrophone tip relative to the nanoparticle stream from the cross-correlation of scattered signals from the needle tip and hydrophone tip. Nanoparticle accumulation in the water tank was mitigated by operation of a collection system (needle, tubing and syringe pump) positioned approximately 3 cm beneath the supply needle. Data were collected with a 100 MHz digitizer (CS320A, Cleverscope, Auckland, New Zealand). Acoustic pressures were determined using a complex-valued calibration of the needle hydrophone [23].

5.2.4 Cell culture & in vitro experiments

Human prostate cancer cells (DU145, American Type Culture Collection, Manassas, VA) were cultured as monolayers in a humidified atmosphere of 95% air and 5% CO_2 at 37°C in RPMI-1640 medium (Cellgro, Herndon, VA) supplemented with 100 g/mL penicillin-streptomycin (Cellgro) and 10% (v/v) heat-inactivated fetal bovine serum (FBS) (Corning, Palo Alto, CA). Cells were harvested at 80-90% confluence for experiments by trypsin/EDTA (Cellgro) digestion, washed with serum and then re-suspended in RPMI at a cell concentration of 10^6 cells/mL. DU145 cells were used as the model cell line for these experiments because they have been widely used and characterized in previous drug delivery studies [13], [14], [20].

Harvested cells were transported in 1.5 mL microcentrifuge tubes and stored on ice until exposure. Optically clear glass cuvettes (Starna Cells, Atascadero, CA) contained 520 μL of cells; CB, SWCNT, or MWCNT added at a final concentration of 25 mg/L, 70 mg/L, 20.1 mg/L respectively; and high-purity calcein (Molecular Probes, Eugene, OR) added as an uptake marker at a final concentration of 10 μM. The CB, SWCNT, and MWCNT concentrations were selected as ones that exhibited the same light transmittance under our laser exposure conditions, as determined by spectrophotometry.

Following exposure, the contents of the cuvette were transferred back into the microcentrifuge tubes with a transfer pipette and stored on ice to reduce uptake due to endocytosis. To label non-viable cells >30 min post-irradiation, propidium iodide (PI, Invitrogen, Grand Island, NY) was added at a concentration of 13.5 μM and cells were incubated for 10 min. Samples were then washed at least three times with phosphate buffer saline (PBS) to remove extracellular fluorescence from the solution.

5.2.5 Data collection and processing

5.2.5.1 *In vitro* exposure experiments

A flow cytometer (BD Accuri, BD Biosciences, San Jose, CA) quantified bioeffects in terms of live cells with intracellular uptake (i.e. intact cells with green fluorescence of calcein loading and without red fluorescence of propidium iodide (PI) staining) and non-viable cells (i.e. intact cells with PI staining). Calcein fluorescence was measured with a 530/28 nm bandpass filter and PI was measured with a 670 nm longpass filter. Samples were run at a constant flow rate of 35 μL/min for 1 min.

A negative, 'sham' control containing cells in RPMI that were not exposed to laser was used to construct a cell population gate in the forward-scattered and side-scattered analysis. Cells within this gate were considered to be intact cells. To account for possible cell loss due to fragmentation, the number of live cells (i.e., PI-negative) for each exposed sample subtracted from the number of live cells for the sham was taken to be the number of fragmented cells, which appeared as a field of debris at low forward and side scatter [80].

5.2.6 Statistical analysis

5.2.6.1 *In vitro* exposures

A minimum of three replicates was used for all conditions, which allowed for the calculation of means and standard deviations (which is how all data are presented). The null hypothesis was that the average fraction of cells with uptake or viability between a sham sample and an exposed sample were equal. The equality of means response between exposed samples and sham samples was tested with ANOVA ($\alpha = 0.05$). The equality of mean response was tested with 1-way or 2-way ANOVA followed by post hoc Tukey's pairwise comparison, depending on the number of data points, using GraphPad Prism 6 (GraphPad Software, La Jolla, CA).

5.3 Results

5.3.1 Effect of CB on intracellular uptake, cell viability and cell fragmentation

We determined the effect of CB, MWCNT and SWCNT on intracellular uptake, cell viability and cell fragmentation due to laser irradiation over a range of fluence values.

Laser irradiation with CB nanoparticles showed progressively stronger bioeffects with increasing laser fluence (**Figure 5.1**). Initially, intracellular uptake increased at a laser fluence ≥ 25 mJ/cm^2, peaked at 44 mJ/cm^2 with 45% of cells exhibiting uptake and then decreased at 44 – 100 mJ/cm^2 (**Figure 5.1a**). When uptake decreased, loss of cell viability increased at 44 mJ/cm^2, peaked at 63 mJ/cm^2 and then decreased and plateaued at 75 – 100 mJ/cm^2 (**Figure 5.1b**). When cell viability loss decreased, cell fragmentation increased at 75 – 100 mJ/cm^2 (**Figure 5.1c**).

Finally, when accounting for cells that exhibited any bioeffect (i.e., uptake, viability loss or fragmentation), there was a steady increase in bioeffects starting at 25 mJ/cm^2 until it plateaued when ~100% of cells were affected at 63 – 100 mJ/cm^2 (**Figure 5.1d**). These data suggest that increasing laser fluence in the presence of CB caused progressively stronger bioeffects, starting with intracellular uptake (i.e., reversible permeabilization), transitioning to loss of viability (i.e., irreversible permeabilization) and finally to cell fragmentation.

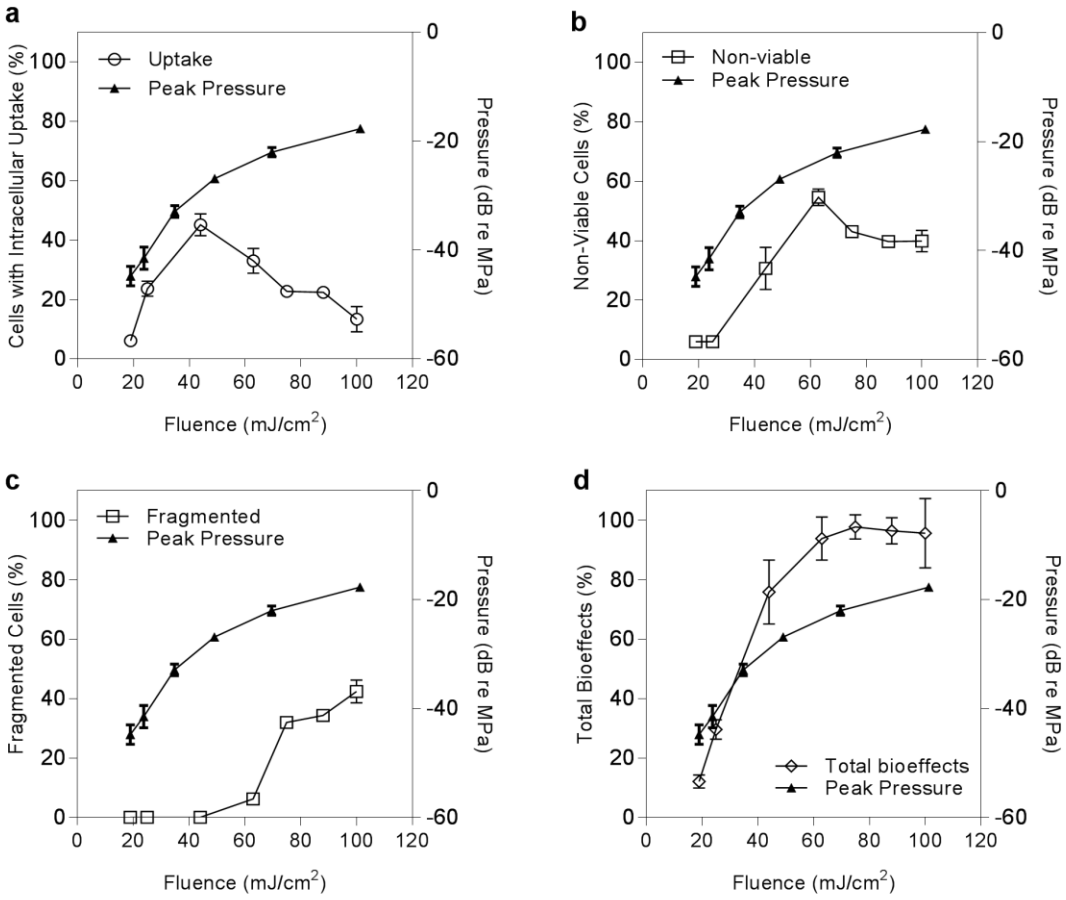

Figure 5.1: (*left y-axis)* Percentage of cells suspended with CB nanoparticles with a) intracellular uptake, b) non-viable cells (i.e. PI+), c) fragmented cells and d) total bioeffects (uptake, non-viable cells and fragmented) after 1 minute of pulsed exposure to laser fluence ranging from 19 - 100 mJ/cm^2. Data show average ± SD (n=3). (*right y-axis*) Cumulative peak pressure output of CB nanoparticles after exposure to laser fluence ranging from 19 – 100 mJ/cm^2. Data show average ± SD (n ≥ 100).

5.3.2 Effect of MWCNT on intracellular uptake, cell viability and cell fragmentation

Laser irradiation in the presence of MWCNT showed behavior similar to CB, but with important differences. Initially, significant uptake was seen at 19 mJ/cm^2, plateaued at 44 – 75 mJ/cm^2 with up to ~50% of cells showing uptake, and then decreased at 88 – 100 mJ/cm^2 (**Figure 5.2a**). Compared to CB, uptake caused by laser irradiation with MWCNT was first observed at a lower fluence, was seen in a higher percentage of cells with uptake, and was maintained at high levels over a much broader range of fluence values. In contrast to CB, cells exposed with MWCNT never experienced significant loss of cell viability over the range of conditions studied (**Figure 5.2b**). Instead, cellular bioeffects transitioned directly from uptake to uptake and fragmentation at fluence ≥ 63 mJ/cm^2 (**Figure 5.2c**). Total bioeffects increased from 19 mJ/cm^2 until it plateaued at 63 – 100 mJ/cm^2.

These data show that the only condition where there was significant uptake and no significant cell viability loss or fragmentation due to exposure with CB was 25 mJ/cm^2 at a level of 24% of cells with uptake. In contrast, exposure with MWCNT caused significant uptake without significant cell viability loss or fragmentation over the range 20 – 44 mJ/cm^2 at a peak level of 50% of cells with uptake. This indicates that use of MWCNT may be preferred over CB when the objective is maximizing intracellular uptake while maintaining cell viability.

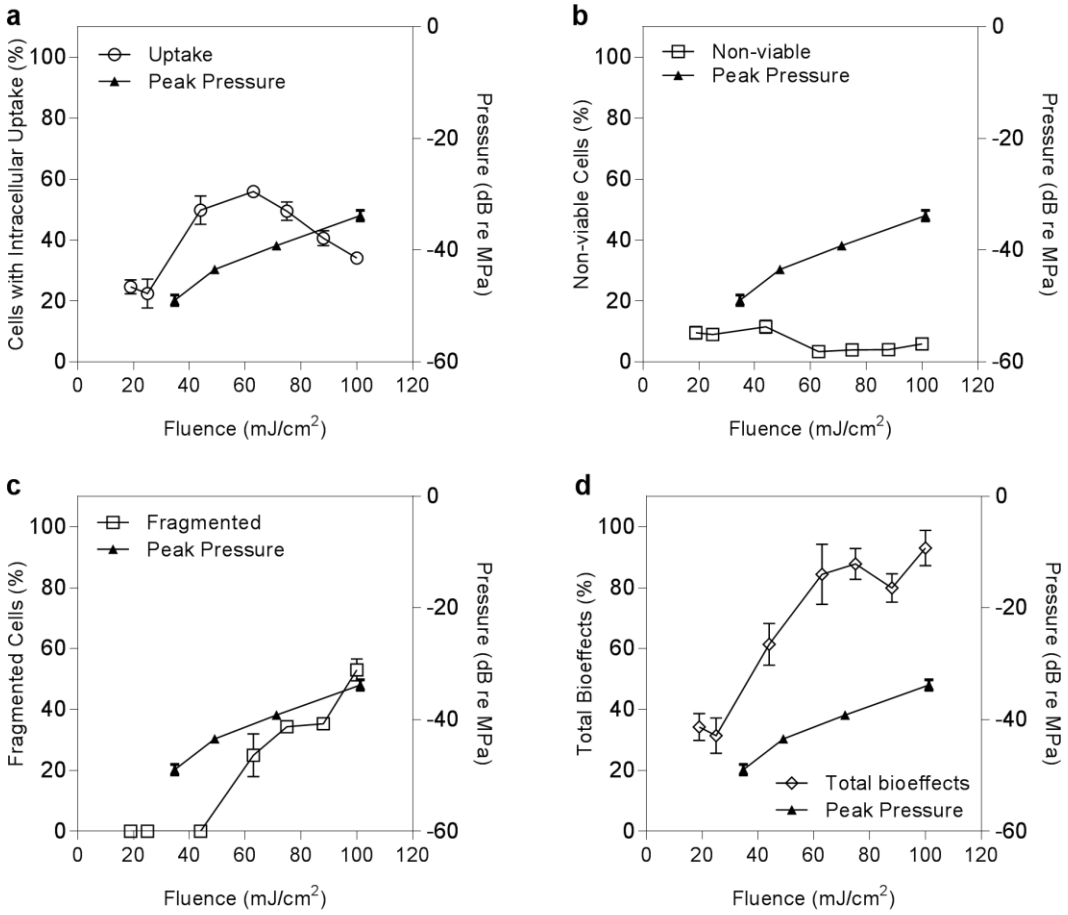

Figure 5.2: (left y-axis) Percentage of cells suspended with MWCNT with a) intracellular uptake, b) non-viable cells (i.e. PI+), c) fragmented cells and d) total bioeffects (uptake, non-viable cells and fragmented) after 1 minute of pulsed exposure to laser fluence ranging from 19 - 100 mJ/cm^2. Data show average ± SD (n=3). (right y-axis) Cumulative peak pressure output of MWCNT after exposure to laser fluence ranging from 35 – 100 mJ/cm^2. Data show average ± SD (n ≥ 100).

5.3.3 Effect of SWCNT on intracellular uptake, cell viability and cell fragmentation

Laser irradiation in the presence of SWCNT did not exhibit significant changes in uptake, viability loss or fragmentation over the range of laser fluences studied, 19 – 100 mJ/cm^2 (**Figure 5.3**). This behavior is dramatically different from what we saw using CB or MWCNT.

We wanted to know if laser irradiation with SWCNTs would ever cause bioeffects, and therefore exposed cells to laser irradiation with SWCNT for up to 3 min (instead of the 1 min exposures used previously) at 25 mJ/cm^2. However, increasing the length of exposure did not significantly alter bioeffects (**Figure 5.4a**). Next, we increased the laser exposure to 5 min and increased laser fluence to 44 – 75 mJ/cm^2. At these extreme conditions, there was still insignificant intracellular uptake (**Figure 5.4b(i)**) and little cell fragmentation (**Figure 5.4b(iii)**), but there was significant viability loss at 63 – 75 mJ/cm^2 (**Figure 5.4b(ii)**). This outcome may be due to thermal effects on cells caused by heat transfer from the SWCNT, which is similar to other studies showing that continuous NIR heating of nanoparticles can lead to significant viability loss [116]–[118].

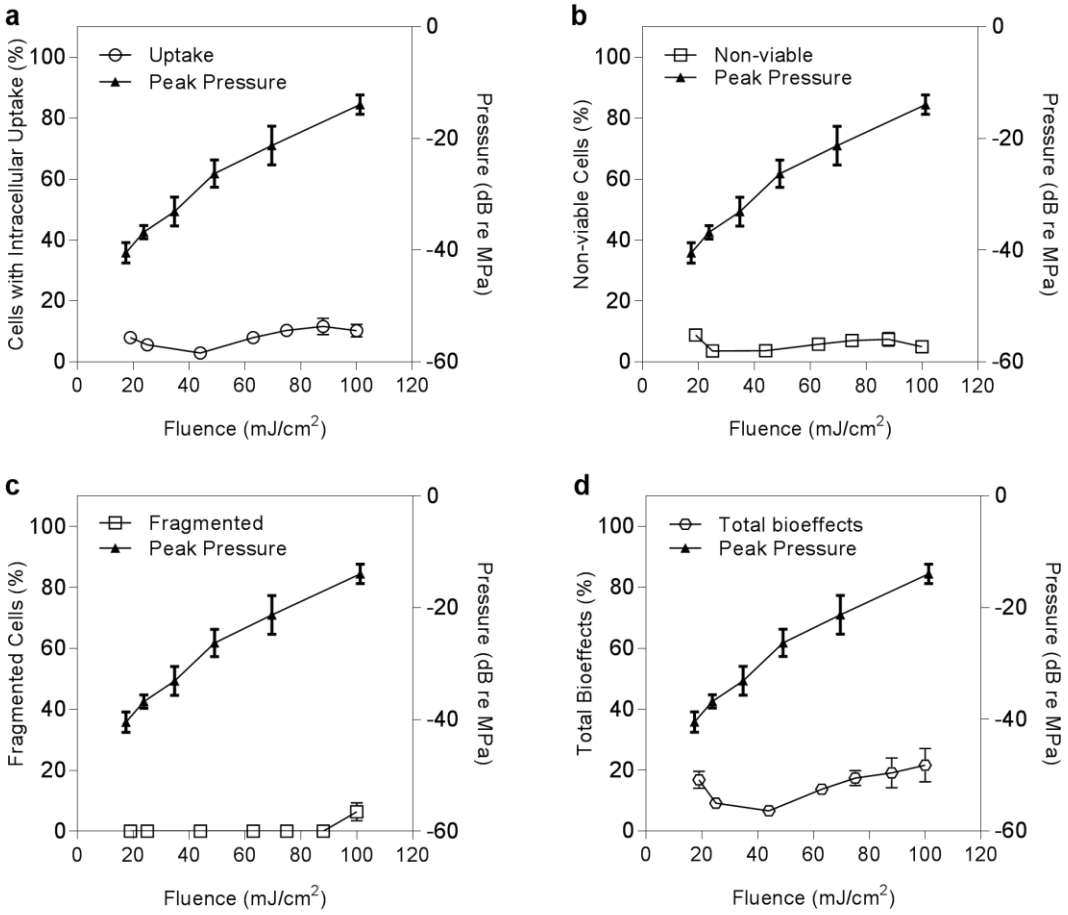

Figure 5.3: (left y-axis) Percentage of cells suspended with SWCNT with a) intracellular uptake, b) non-viable cells (i.e. PI+), c) fragmented cells and d) total bioeffects (uptake, non-viable cells and fragmented) after 1 minute of pulsed exposure to laser fluence ranging from 19 - 100 mJ/cm^2. Data show average ± SD (n=3). (right y-axis) Cumulative peak pressure output of SWCNT after exposure to laser fluence ranging from 13 – 100 mJ/cm^2. Data show average ± SD (n ≥ 100).

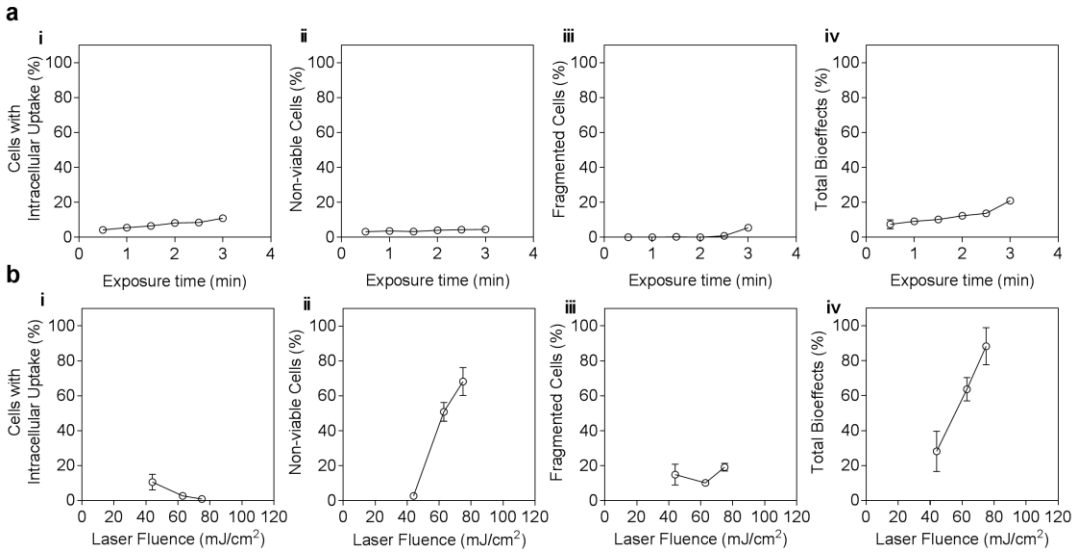

Figure 5.4: Percentage of cells suspended with SWCNT after a) exposure to 25 mJ/cm2 for 0.5 – 3 min that are ai) intracellular uptake, aii) non-viable c, aiii) fragmented cells and aiv) total bioeffects (uptake, non-viable and fragmented). Percentage of cells with SWCNT after b) exposure to higher laser fluence (i.e. (44-75 mJ/cm^2) for 5 min with bi) intracellular uptake, bii) non-viable cells, biii) fragmented cells and biv) total bioeffects (uptake, non-viable and fragmented). Data show average ± SD (n=3).

5.3.4 Characterization of photoacoustic pressure emitted by laser-irradiated nanoparticles

During TNET, a variety of energy transfers can occur, including momentum transfer due to the rapidly expanding bubbles formed around the nanoparticles and heat transfer from the hot nanoparticles and surrounding bubbles. We hypothesized that the varied effects of the three different types of carbon nanoparticles studied here might be explained by differences in photoacoustic pressure generated by the rapidly expanding bubbles.

First, we characterized photoacoustic pressures generated by laser-irradiation of the nanoparticles (**Figure 5.5**). For all three types of nanoparticles, there was a primarily positive pressure pulse, consistent with the rapid expansion of bubbles due to heat transfer from the hot nanoparticles to the surrounding medium, followed by a slow cooling of the bubbles that did not generate a significant negative pressure. A mostly positive pressure pulse also means that stresses due to the acoustic radiation are largely compressive in the free field and that there were no significant pressure oscillations. The pressure rise time was on the order of 20-40 ns and the pulse duration was hundreds of nanoseconds, which is an order of magnitude longer that the laser pulses and is consistent with prior calculations of heat transfer kinetics from the irradiated nanoparticles [23].

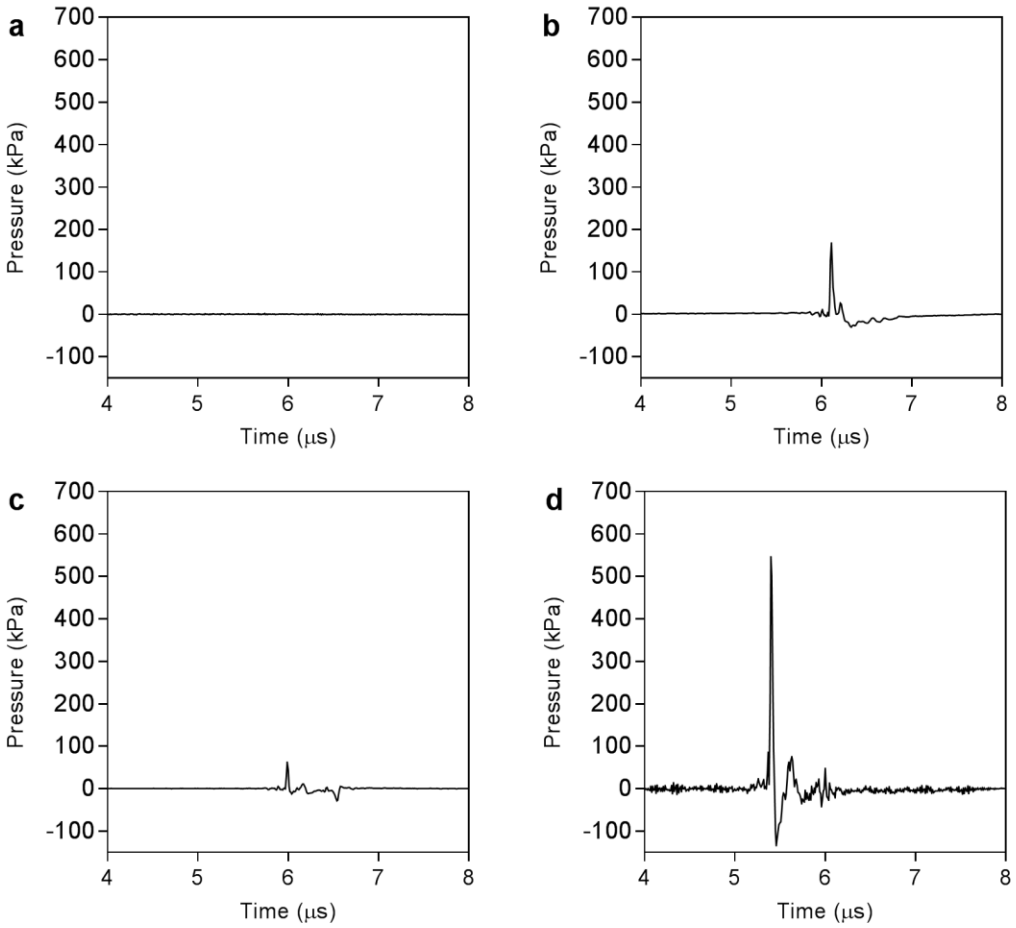

Figure 5.5: Cumulative peak pressure was measured for water, CB, SWCNT, MWCNT irradiated by nanosecond pulses. Pressure waveforms of a) water, b) CB, c) MWCNT and d) SWCNT showing pressure (kPa) versus time (μs) after exposure to in-water laser fluence of 200 mJ/cm^2.

In addition to these similarities, the absolute pressures are significantly different among the three different types of nanoparticles when exposed at the same laser conditions using nanoparticle concentrations that absorbed roughly the same amount of energy. For example, when exposed to an in-water laser fluence of 200 mJ/cm^2, laser irradiation of CB generated a peak pressure of 292 ± 23 kPa (mean ± standard deviation) over the ensemble of pulses collected (**Figure 5.5b**). In contrast, the MWCNT generated a much lower pressure of 69 kPa ± 5 kPa (**Figure 5.5c**) and the SWCNT generated a much higher pressure of 549 ± 49 kPa (**Figure 5.5d**). Although SWCNT generated the highest photoacoustic pressure, it caused the weakest cellular bioeffects (**Figure 5.3**). While CB and MWCNT had significantly different pressures, they caused similar bioeffects over a range of conditions (**Figure 5.1** and **Figure 5.2**). These findings suggest that there is a poor correlation between photoacoustic pressure and cellular bioeffects.

5.3.5 Correlation between photoacoustic pressure and cellular bioeffects

To better understand the relationship between pressure and cellular bioeffects, we examined the peak photoacoustic pressures associated with each of the cellular exposures to see if there might be a correlation. For CB, as pressure continuously increased with increasing laser fluence, uptake and viability loss each increased, peaked and declined (**Figure 5.1a, b**), cell fragmentation increased above a threshold fluence (**Figure 5.1c**) and total bioeffects increased and plateaued (**Figure 5.1d**). For MWCNT, pressure showed a similar relationship with uptake, fragmentation and total bioeffects (**Figure 5.2a, c, d**), but there was no change in nonviable cells while pressure steadily increased (**Figure 5.2b**). Finally, for SWCNT, as pressure increased, there were little or no bioeffects (**Figure 5.3**).

Review of the acoustic data showed a tendency for pressure pulse length to modestly increase at lower fluences, so that peak pressure may not always track energetic output. This effect was quantified using time-averaged acoustic potential energy density, which showed relatively minor differences in fluence trend from those obtained with peak pressure (**Figure 5.6**), suggesting that neither of the two cumulative acoustic quantities was universally correlated to bioeffects. Estimates of total acoustic energy emitted by the nanoparticle stream, paired with calculations of energy absorbed by the CB nanoparticles [23] indicated that the proportion of absorbed energy converted into acoustic energy is no more than 0.51% at the highest fluence evaluated (100 mJ/cm^2). Since this fraction is so small, it is perhaps less surprising that the acoustic correlations to bioeffects are so weak. Acoustic monitoring as performed here may indicate vapor bubble formation, but may not have value as an indicator of photoporation-mediated drug delivery.

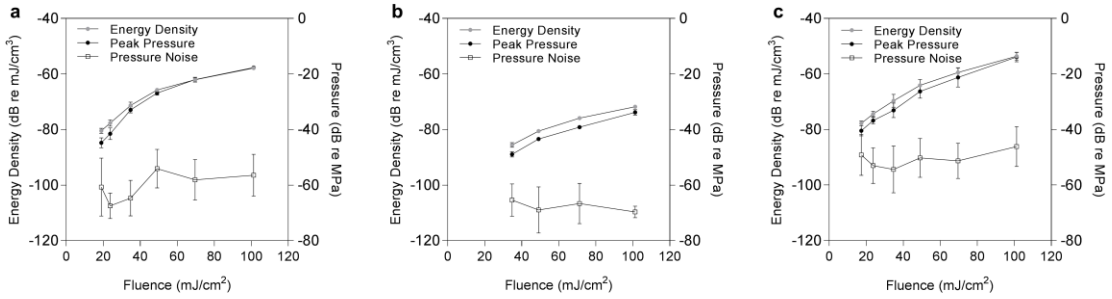

Figure 5.6: ***(left y-axis)*** **Acoustic potential energy density signal,** ***(right y-axis)*** **peak acoustic pressure signal, and pressure noise (bottom curve) as a function of in-water fluence for laser-irradiation of a) CB nanoparticle, b) MWCNT, and c) SWCNT. Data show mean and SD (n ≥ 100). Background noise was measured in the absence of laser irradiation. Time-averaged acoustic potential energy density was calculated as $U = (1/\tau\rho c^2)\int_0^\tau p(t)^2 dt$ where $p(t)$ is the acoustic pressure as a function of time, τ is the laser pulse repetition period, and ρ and c are the medium density and sound speed, respectively.**

While there may be a correlation between photoacoustic pressure and bioeffects under some circumstances, it will be most informative to combine all the data to determine if there is a universal correlation of bioeffects with pressure, independent of type of nanoparticle, to serve as a unifying parameter more closely related to mechanism of action. We therefore plotted bioeffects (e.g., uptake) as a function of peak photoacoustic pressure generated by CB, MWCNT, and SWCNT (**Figure 5.7a**). This analysis showed that peak pressure does not serve as a unifying parameter (i.e., the data do not all fall on a common curve on any of the graphs) and therefore does not explain the disparate bioeffects caused by different types of nanoparticles. While the bioeffects of CB and MWCNT often show similar functionality, there is an abscissa shift such that bioeffects caused by MWCNT occur at lower pressures than when they are caused by CB.

We also plotted bioeffects caused by CB, MWCNT and SWCNT as a function of laser fluence, which can be thought of as a measure of total energy input into the system (**Figure 5.7b**). While the data again do not all fall onto common curves, the correlations were much better compared to peak photoacoustic pressure (**Figure 5.7b**). Although SWCNT had little effect on cells and MWCNTs did not generate nonviable cells, the CB and MWCNT data follow each other reasonably well, suggesting that the total energy input is a better correlation – and perhaps a better mechanistic indicator – for bioeffects caused by TNET.

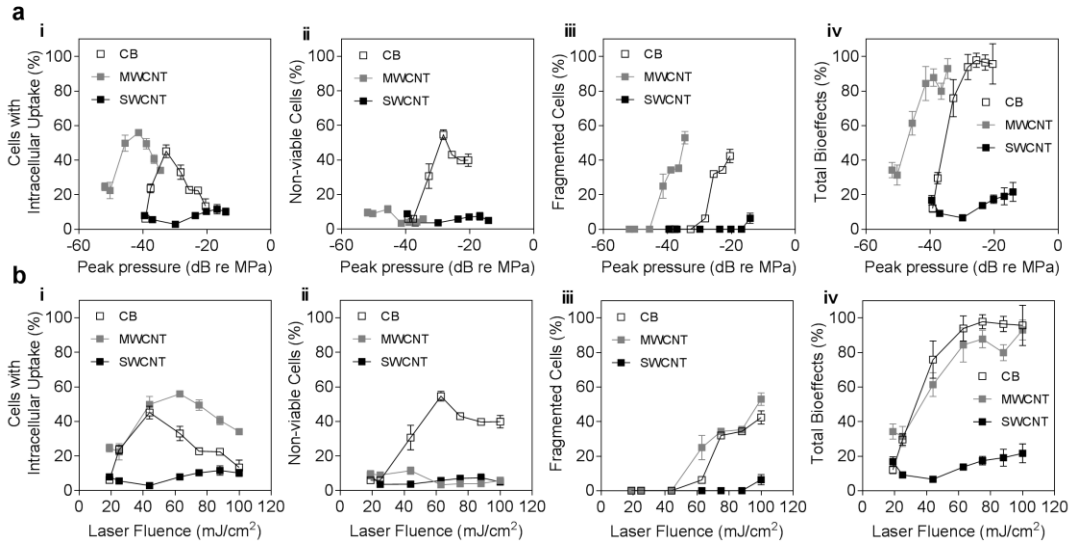

Figure 5.7: Percentage of i) cells with intracellular uptake, ii) non-viable cells (PI+), iii) fragmented cells, and iv) total bioeffects after exposure with CB, MWCNT, and SWCNT with a) increasing peak pressure and b) increasing laser fluence. Expected pressures for those not physically measured were interpolated from measured pressure to plot bioeffects over same range of laser fluence as *in vitro* experiments.

5.4 Discussion

The purpose of this study was to investigate the effect of different carbon nanoparticles – CB, MWCNT, SWCNT – in terms of their TNET-associated bioeffects, as well as their photoacoustic output. We found that each type of nanoparticle had different bioeffect "profiles" and had different photoacoustic emission intensities.

Laser-irradiated CB affected cells in ways that led to reversible permeabilization (i.e. viable cells with intracellular uptake) without significant viability loss at mild conditions (e.g., low laser fluence) (**Figure 5.1a**); a combination of reversible permeabilization and irreversible permeabilization (i.e., nonviable, intact cells) at moderate conditions (**Figure 5.1a-b**); and cell fragmentation at the strongest conditions (**Figure 5.1c**). Laser-irradiated MWCNT, on the other hand, affected cells in ways that only led to

reversible permeabilization at mild or moderate conditions (**Figure 5.2b**) and at strong conditions there was also fragmentation (**Figure 5.2c**). Interestingly, SWCNT did not cause reversible permeabilization (**Figure 5.3b**), but at very strong conditions (i.e. high laser fluence and longer exposures) caused irreversible permeabilization (**Figure 5.3c**). Since MWCNT showed the broadest range of laser fluence values leading to reversible permeabilization without viability loss, they may be an attractive nanoparticle system for TNET-mediated intracellular drug delivery applications. CNTs have been previously used for other drug delivery applications [119], [120] and have been shown to be nontoxic upon surface functionalization [121], [122] in some *in vivo* scenarios [123]–[125].

The three types of nanoparticles released mechanical energy in the form of photoacoustic waves. The experimental data showed that all nanoparticles generated increasing photoacoustic pressure with increasing laser fluence, but the absolute peak pressure intensity varied with the type of nanoparticle. Cumulative peak photoacoustic pressure was highest for SWCNT, followed by CB, and then MWCNT (**Figure 5.5**). This trend does not mirror that of bioeffects, where SWCNT caused almost no bioeffects, but had the highest peak pressure (**Figure 5.3**). Moreover, the pressure waveform (i.e., rise-time, pulse duration) was similar for each type of nanoparticle (**Figure 5.5**), which also does not correlate with bioeffects, which varied with type of nanoparticle. Because the different types of nanoparticle had different geometries and aggregate sizes, the radial velocity and acceleration profiles of the bubbles they generated could be different, but analysis of these effects is beyond the scope of this study. Also, the concentration of each type of nanoparticle was different (i.e. to provide similar laser energy absorption), which means that the energy absorbed on a per-nanoparticle basis was different for each type of

nanoparticle; this may also play a role in explaining the effect of nanoparticle type on bioeffects. Altogether, the lack of correlation between features of the pressure output and cellular bioeffects caused by different types of nanoparticles suggests that the photoacoustic pressure may not play a direct mechanistic role in the observed bioeffects.

Photoporation-mediated bioeffects are caused by the conversion of laser light energy into other forms of energy by carbon nanoparticles that act as the energy transducers. One form of energy emitted by the nanoparticles is in the form of an acoustic wave created by a rapidly expanding gas bubble. Our data suggest that this form of energy is not mechanistically responsible for the observed bioeffects. The bubble growth also pushes fluid that can impact cells, imparting compressive and/or shear forces to the cell membrane that could cause bioeffects. The nanoparticles and bubbles are also very hot (e.g., >> 100°C), so there can be heat transfer to cells that could lead to bioeffects [23].

Our previous work suggested that bioeffects from photoporation were not due to long-range acoustic effects, but were dominated by short-range effects [23]. Data from the present study also suggested that long-range cumulative acoustic pressure was not likely the dominant mechanism in TNET given the lack of correlation between bioeffects and photoacoustic pressure from the different types of nanoparticles, However, given the complex pressure behavior close to the pressure source [126], the pressure within a length scale on the order of the largest nanoparticle/bubble dimensions (i.e. 1 – 10 μm for the conditions tested here) may be mechanistically important and provide additional insight. For example, the near-field pressure and associated fluid motion from rod-like nanoparticles (e.g. CNTs) should be quite different from spherical nanoparticles (e.g. CB)

[127] and, in that way, explain the varied bioeffects seen for the different types of nanoparticles.

In contrast to cumulative photoacoustic pressure, total energy input to the nanoparticles correlated better with bioeffects (**Figure 5.7b**). This suggests that a different form of energy output from the nanoparticles that correlates with energy input is mechanistically responsible for TNET-mediated bioeffects. Future work should investigate these other forms of energy output, including short-range cell-nanoparticle interactions (i.e. 1 - 10 μm) mediated by thermal, fluid mechanical and/or near-field pressure energy transfer from nanoparticles and their surrounding bubbles to nearby cells, either directly or via the surrounding medium to transiently porate cell membranes.

5.5 Conclusion

In this study, we compared the cellular bioeffects of CB, MWCNT and SWCNT during nanosecond-pulsed NIR laser irradiation. Using DU145 prostate cancer cells as a model system, we found that each nanoparticle had a different bioeffect "profile" as laser fluence increased. CB showed a clear transition from cells with uptake of molecules (i.e., reversibly permeabilized cells) to non-viable cells (i.e., irreversibly permeabilized cells that remained intact) to fragmented cells (i.e., appearing as cellular debris) with increasing laser fluence. In contrast, cells exposed to laser-irradiated MWCNT exhibited uptake at higher levels over a broader range of laser fluence values compared to CB nanoparticles. Moreover, very few non-viable cells were seen after irradiation with MWCNTs; cells were either viable or found fragmented at the highest fluence levels. SWCNT showed still different behavior, with little evidence of any cellular bioeffects, except at the highest laser

exposure duration and fluence, which generated non-viable cells, some cell fragmentation, but no significant uptake of molecules into cells. The finding that MWCNTs enable efficient intracellular delivery without loss of cell viability over a range of laser fluence values may be of use for intracellular delivery applications.

In order to explain these different behaviors, we tried to correlate the bioeffects with peak photoacoustic pressure emitted by the nanoparticles, but found that there was no universal correlation when data from all three types of nanoparticles were considered together. This indicated that the peak photoacoustic pressure was not mechanistically responsible for bioeffects. Additionally, since the pressure waveforms for CB, MWCNT, and SWCNT were similar, with the exception of the cumulative peak pressure, this again suggests that photoacoustic pressure does not explain the varied bioeffects caused by the different types of nanoparticles. Future studies should examine the role of short-range cell-nanoparticle interactions mediated by thermal, fluid mechanical and/or near-field acoustic effects and their possible role in TNET-mediated bioeffects.

CHAPTER 6. DISCUSSION

Novel drug delivery techniques are essential to improve drug targeting. Specific targeting is needed for delivery of potentially revolutionary therapies once they reach the cytosol [4], [5]. However, the cell's plasma membrane presents a barrier to the delivery of molecules that are polar or large in nature to be delivered by methods other than active transport. Active transport mechanisms can degrade the drug during the endocytotic pathway [8]. Physical methods are of interest due to their ability to bypass the endocytotic pathway by physically creating transient pores in the membrane to enable passive transport of molecules into the cytosol [31]. However, one of the major disadvantages of physical methods is that applying too much force to the cell can lead to irreversible damage and viability loss. Thus, efficient physical drug delivery methods balance the extent of physical disruption (maintaining high cell viability), while delivering molecules efficiently to the intracellular space.

To balance this tradeoff, our lab has developed a novel laser-mediated method known as TNET. Previous studies have shown that when CB nanoparticles in suspension with cells and small molecules are irradiated by nanosecond pulse NIR laser energy, highly efficacious delivery and high viability are achieved [13], [14], [73]. First, Chakravarty's studies with femtosecond and nanosecond laser pulses suggested that the carbon-steam reaction and the photoacoustic effects as a byproduct, were responsible for intracellular delivery [13]. Further studies by Sengupta showed that instead, short-range interactions due to cell-particle interaction (e.g. bubble contact with cell) were responsible for

bioeffects [23]. As such, this thesis sought to provide a more thorough understanding of fundamental biophysical phenomena that drive TNET.

6.1 Role of cell mechanics in TNET

The first study in this work sought to understand the role of cell mechanics in TNET and more specifically how cellular mechanics influence the outcome (i.e. intramolecular uptake and viability loss) of TNET. We explored cytoskeletal mechanics and cell membrane fluidity by altering their properties and then quantified the resulting bioeffects after *in vitro* exposures.

We found that destabilizing the cytoskeleton with LatA led to greater intracellular uptake and less viability loss due to TNET. We hypothesized that the effects of cytoskeletal weakening may be due to an enhanced ability of the cell to recover and reseal the membrane. Other studies have shown that the cytoskeleton can be a physical obstacle for microvesicles needed for membrane fusion [93], [94] and as such destabilizing actin filaments can enhance membrane resealing [94], [95].

We also used Jasplak to rigidify the cytoskeleton, with the expectation that Jasplak treatment would result in less intracellular uptake compared to non-treated cells. However, the results showed that there was no significant difference in uptake and viability loss compared to non-treated cells. We hypothesized that these results could be attributed to the conflicting effects of Jasplak present in the literature. Some studies showed that Jasplak can rigidify the cytoskeleton [77], [97], [98], whereas others showed that Jasplak can induce the opposite effect (i.e. destabilize actin) [74], [99], [100].

In this study, we also altered plasma membrane fluidity by enriching and depleting cholesterol content with methyl-β-cyclodextrin (MβCD) and water-soluble cholesterol (WSC), respectively. The results indicate that changing membrane fluidity by altering cholesterol content with these reagents did not induce a significant difference in intracellular uptake or viability loss compared to non-treated cells for either compound used. From these results, we concluded that cell membrane fluidity did not play a significant role in uptake and viability in TNET.

6.2 Cell-CB nanoparticle interactions drive TNET

The second part of this work focused on understanding the parameter space of short-range material-laser and more specifically, how total energy input influences cell-CB nanoparticle interactions which drive TNET. We studied the effect of total energy input on this interaction by evaluating the effects of laser pulses, CB nanoparticle concentration, cell concentration, and medium viscosity.

Our studies on the effects of CB nanoparticle concentration and cell concentration highlighted several important aspects of TNET. First, we saw that there was a nanoparticle concentration threshold necessary for bioeffects and below that threshold significant bioeffects did not occur. This highlights several important aspects of TNET – first that there is a threshold CB nanoparticle concentration required for there to be bioeffects. Second, we also observed a laser fluence threshold (i.e. $\geq$ 44 mJ/cm^2) for bioeffects to occur, regardless of CB nanoparticle concentration. Above these two thresholds, we saw that bioeffects increase, first as increased uptake, then increased viability loss and finally increased cell fragmentation.

Our additional studies with cell concentration and laser pulses revealed that total energy input per cell is a governing parameter for photoporation achieved with TNET. Moreover, we saw that as cell concentration decreased cellular bioeffects increased, being that more energy was imparted on each cell. Similarly, we saw that with increasing laser pulses, cellular bioeffects increased, again due to the increase in total energy input per cell. Taken altogether with the CB concentration and laser fluence data, we showed that total energy input per cell is a strong predictor of bioeffects due to TNET.

Finally, we also studied the effect of cell medium viscosity on bioeffects. By using carboxymethylcellulose (CMC) we increased the viscosity of the cell medium ~13 fold and showed that uptake was significantly reduced in a more viscous medium compared to a suspension without CMC. This suggests that the short-range energy transfer induced by the growth of the bubble and fluid displacement due to bubble radial motion was dampened by the increase in viscosity and led to lesser bioeffects. Another factor could be the molecular diffusion was slowed and that led to reduced uptake.

6.3 Mechanistic implications of photoacoustics

The last part of this work investigated the TNET effects of different carbon materials and their mechanistic implications for TNET. Fundamentally, we were interested in separating bioeffects from the influence of the particle. We measured the cumulative pressure profiles of three carbon particle systems – CB, multi-walled carbon nanotubes (MWCNT) and single-walled carbon nanotubes (SWCNT). Then, we incorporated these particle systems *in vitro* and quantified the resulting bioeffects to determine if acoustics universally correlate to bioeffects.

The cellular bioeffects of CB, MWCNT, and SWCNT had different bioeffect 'profiles' *in vitro*. First, as the laser fluence increased, CB showed a transition from cells with uptake to non-viable cells (i.e. PI+ cells) to fragmented cells. In contrast, cells exposed with MWCNT showed higher uptake levels over a greater range of fluence compared to CB and at even higher fluence showed fragmentation. SWCNT had little effect on cells – that is, there was no significant uptake or viability loss.

From these observations, we then tried to correlate bioeffects with the particles' respective acoustic profiles. Our acoustic measurements revealed that the SWCNT exhibited the highest cumulative peak pressure profiles compared to CB and MWCNT, in descending order. Since there was no universal correlation with peak pressure and resulting bioeffects, we hypothesized that total energy input was mechanistically more important than pressure output in TNET.

CHAPTER 7. CONCLUSIONS & RECOMMENDATIONS

7.1 Conclusions & Contributions

7.1.1 Conclusions

The overall aim of this work was to provide mechanistic understanding of the energy transductions in TNET that impacts cells. As such, understanding the role of cellular mechanics, CB-cell interaction and photoacoustics in TNET was needed to enable a more rational approach in optimization of this drug delivery platform. First, we showed that the mechanical structure of the cell and its ability to repair itself after TNET is dependent on the cytoskeleton (actin filaments). We also showed that plasma membrane fluidity does not significantly influence bioeffects. Second, we showed that total energy input and total energy input per cell strongly influences CB-cell short-range interactions and moreover, these interactions are strongly dictated by CB nanoparticle concentration and laser fluence. This provides mechanistic insight needed before translating this platform for applications, for example – where the threshold for intracellular uptake and viability loss can be calibrated by specific nanoparticle concentrations. Lastly, we showed that the role of photoacoustics in TNET is minimal at best, since peak pressure does not universally correlate with bioeffects and that mechanistically, total energy input is more critical. This again supported our findings that TNET is driven by short-range CB-cell interactions, rather than by long-range acoustics.

7.1.2 Contributions

This thesis contributed to intracellular drug delivery research in various ways. Leveraging nanotechnology coupled with NIR laser systems is a cutting edge platform for which there is growing interest [105]. More specifically, most laser-mediated photoporation systems use other materials (e.g. gold) for delivery, typically by a thermal mechanism, whereas we have uniquely studied and successfully used CB nanoparticles to achieve efficacious delivery and develop a mechanistic understanding of TNET that appears to involve mechanical, and possibly thermal, interactions. By showing that short-range nanoparticle-cell interactions drive TNET, we laid the foundation for further optimization of this platform before translating into applications. In addition, by studying material-laser interactions, we provided the foundation for future studies which must consider materials properties for successful drug delivery. Overall, TNET is a novel, promising method to deliver small molecules into cells efficiently and once optimized, has potential to have great impact in the clinic and improve healthcare.

7.2 Recommendations

7.2.1 Boundary effects of the cuvette

The *in vitro* intracellular drug delivery studies were typically conducted using a Pyrex cuvette system. We were curious about the extent of the cuvette's role in TNET and more importantly if it had a significant role at all. As such, we conducted some preliminary studies to explore the consequence of the cuvette on bioeffects. The initial results (**Appendix A**) suggest that the physical boundary of TNET does in fact play an interesting role in observed bioeffects because of TNET.

First, we evaluated acoustic field effects present in the cuvette, in which a set of *in vitro* delivery experiments were conducted in a water tank. The purpose of submerging the cuvette with CB nanoparticles, cells, and calcein in a large bath of water was to minimize reflections off the glass-exterior interface normally present when the cuvette was irradiated in air (i.e. not submerged in water). The results show that intracellular uptake was significantly reduced for samples submerged and irradiated in water compared to samples irradiated in air (no water) (**Appendix A**). These preliminary results suggest that reverberations in the cuvette, due to acoustic energy buildup and reflections of tensile stresses at the glass-air interface may contribute to TNET.

We also considered the physical effects of the cuvette walls and boundary. To vary the physical boundary of the cuvette wall, we irradiated CB nanoparticles, cells and calcein in cuvettes with different path lengths (i.e. 2.5 mm and 10 mm). The preliminary results show that cuvette with a longer path length (10 mm) showed a significant increase in cell viability compared to the 2.5 mm cuvette (**Appendix A**). These initial results suggest that the physical boundary (i.e. cuvette walls) is important to TNET and moreover, supports our hypothesis that TNET is mediated by short-range, local effects. Combined with the water tank experiments, these results make a case to better understand the physical role of the cuvette in TNET.

With that, a study further exploring these cuvette effects is warranted. Understanding the physical boundary effects is integral for our mechanistic understanding of TNET and has implications for translating this platform *in vivo*. The next set of studies should attempt to answer the question of TNET's efficacy if unconstrained and unbounded by the cuvette's walls. One way to test this is to design a cuvette apparatus (e.g. consisting

of low density polyethylene walls or mylar film surfaces and neoprene walls) which would minimize acoustic boundary effects while maintaining optical transparency necessary to irradiate samples. An *in vitro* experiment can then be conducted where prior to irradiation the new cuvette is submerged in a water tank to further minimize acoustic reflections that would be present at an air-glass interface. Since it is possible that the reflections exert tensile stresses on the cells, if this new custom cuvette shows greater efficacy (i.e. higher viability and uptake) compared to the Pyrex cuvette, it would suggest that the rigid boundaries are an impediment to higher efficacy in TNET. Moreover, it would suggest that the rigid boundaries act as a 'kill zone', where cells near the rigid boundaries experience greater tensile stresses compared to cells near the cuvette interior. We observed this type of phenomena where the 2.5 mm cuvette exhibited greater viability loss compared to the 10 mm cuvette when irradiated in air (i.e. not submerged in water) (**Appendix A**). Investigating the effect of rigid boundaries is critical to predicting how TNET would perform *in vivo*, where the boundaries would have a drastically different rigidity or lack thereof due to soft tissue. Furthermore, if less rigid interfaces lead to more intracellular uptake and higher viability, we could better optimize the platform for *in vivo* work and for eventual translation into the clinic.

7.2.2 Discerning stresses experienced by the cell under TNET

To further elucidate the biophysical basis of TNET, we need to understand the magnitude and type of stresses experienced by the cell. This thesis suggests that TNET is mediated by short-range cell-nanoparticle interaction due in part to the presence and growth of vapor bubbles. In conjunction with the preliminary cuvette boundary work and the breadth of parameters studied for the short-range effects, it is possible that the cells

experience mechanical (i.e. tensile, compressive, shear) stresses and/or thermal stresses from point sources (i.e. local effects from CB nanoparticles).

Our acoustic measurements of irradiated nanoparticle streams (**CHAPTER 5**) showed a mostly compressive acoustic profile, in contrast to other physical methods which leverage acoustic stresses for poration. For example, cavitation events in ultrasound drug delivery methods release acoustic waves with tensile and compressive components, where the compressive component of these waves is reported to lead to subsequent cellular or tissue damage [60], [61].

To discern the mechanical stresses experienced by the cell in TNET, a combination of high speed imaging and computational efforts could provide more insight. There are some systems in the literature which have coupled external imaging with high resolution microscopy and pulsed lasers [56], [57], but the challenge is often reconciling spatial resolution with temporal resolution. For instance, high speed imaging has been used to observe effects of sonoporation [128], [129] but the bubble lifetime existed well beyond what we have seen in our studies (i.e. 1-10's of microseconds vs hundreds of nanoseconds). Thus, a more pragmatic approach would be to employ computational methods coupling theoretical predictions with experimental observations.

There have been previous attempts to simulate the behavior of phospholipids in the cell membrane upon impact of shock waves using molecular dynamics (MD) [130]–[132] and coarse grain MD methods [133]. The acoustic emissions in our system do not have characteristics of shock waves, but nevertheless the literature can provide a basis for simulating cellular response to stress fronts. One limitation to computational methods is

that the entire cellular response cannot be captured by current techniques. That is, current computational capabilities can either capture lipid dynamics or continuum mechanics of the cell, but not both length-scales. Simulations can still be useful though to comprehend cellular response to stress at the membrane level. Moreover, if we can understand how the membrane deforms under stresses from TNET, we can better predict bioeffects associated with TNET. Computational models can also be used to simulate stress thresholds needed to transiently porate the membrane and those thresholds can then be correlated to extent of intracellular uptake and viability based on various input parameters (e.g. laser fluence, CB nanoparticle concentration).

From our membrane fluidity studies (**Chapter 3**), we hypothesized that energy transduction during TNET is primarily mechanical in nature; however, we do not have direct evidence to rule out a thermal mechanism. To test the possibility of a thermal mechanism, probes that could indicate a temperature change or lipid phase transition in the cell membrane should be considered. There have been some studies which have used FTIR analysis [134] and fluorescent probes such as diphenylhexatriene (DPH) [135]–[137] for fluorescence anisotropy analysis to quantify lipid phase changes. These types of probes may serve as assays to determine if TNET has a strong thermal energy component necessary for cell poration and drug delivery.

Finally, there is also interest in discerning if shear stresses lead to permeabilization and molecular delivery in TNET. Other work with needle loading [138] and microfluidic devices [139] showed that shear forces can cause reversible permeabilization. It is possible that during TNET, cells experience shear stresses which causes bioeffects. McNeil's work [138] for example, showed that adding poloxamers (i.e. pluronics) preserved cell viability

after shear loading cells to deliver macromolecules. Interestingly, previous work using TNET also showed that using poloxamers enabled greater cell viability compared to exposed samples without the treatment [80]. Further studies comparing and quantifying shear stresses of TNET to other methods would be useful to better elucidate the impact of shear on permeabilization of cells for drug delivery.

7.2.3 Length-scale of TNET effects

Our studies have shown that long-range effects (i.e. cumulative acoustic output) is not likely in TNET (**Chapter 5**). Additionally, our further studies have shown that short-range effects (i.e. cell-CB interaction) are most likely dominant (**Chapter 4**). Based on our observations, we hypothesize that energy transduction from the laser-activated carbon nanoparticle is occurring on the order of 1 – 10 μm (**Chapter 5**). However, in the scope of this thesis, we have not been able to definitively provide a length-scale of TNET effects. Thus, to further explore cell-CB interaction and discern the length-scale of effects, individual cell-particle interactions should be tested. This could be conducted with gel microdroplets, which have been previously used to isolate single cells and molecules into agarose microdroplets and quantified with flow cytometry [140]. These droplets can be used to study the local environment by studying individual cellular effects in suspension with CB nanoparticles.

7.2.4 Nanoparticle studies and criteria for future TNET efforts

7.2.4.1 Carbon studies

Different carbon nanoparticles have been studied in this thesis (i.e. CB, SWCNT, MWCNT). We tested CNTs with a length dimension on the order of microns, but shorter SWCNT and MWCNTs are readily available. An *in vitro* exposure study to compare bioeffects as a result of differing aspect ratios would be interesting, considering possible differences in timescale for heat transfer and subsequent bubble growth due to changes in nanotube length.

CB's broadband absorption in the NIR is related to its electron band structure and the electronic states upon irradiation. Understanding this laser-CB interaction on the electronic and photonic level may provide more insight into the transfer of energy upon irradiation. Additionally, it would be worthwhile to understand the absorption behavior of other carbon allotropes such as diamond [141], graphene [142], and other fullerene-based [143], [144] nanoparticles and test their performance *in vitro* to understand if a carbon nanoparticle is essential to the bioeffects achieved with TNET.

7.2.4.2 Criteria for nanoparticles *in vivo*

Prior to translating TNET *in vivo,* it is important to understand the role of materials properties in TNET. Due to difficulties in uniform dispersion of the aggregates, constraints on size (due to aggregation) and issues of dispersion with previous attempts at *in vivo* work [145], it is not yet known if CB nanoparticles are the ideal candidate for future TNET work. Thus, testing and designing other candidate nanoparticles *in vitro* will be critical prior to *in vivo* studies.

Nanoparticle size is an important parameter for *in vivo* work. Particles < 5 nm in diameter can clear rapidly in the renal system [146], but reducing the size of the

nanoparticles also decreases its melting point [147] and can lead to morphological changes upon irradiation. For tumor applications, nanoparticles ~50 nm in diameter can penetrate complicated vasculature, but that is also dependent on surface charge and particle morphology [148]. To compare, our CB nanoparticles have a primary particle size of 25 nm but aggregate into agglomerates on the order of ~200 nm due to van der Waals forces. Thus, testing other materials which can be uniformly dispersed and resist agglomeration is necessary for practical translation of TNET *in vivo*.

Next, significant work on particle modification for *in vivo* stability is necessary. Studies have shown that surface modification of SWCNT [149], [150] and MWCNT [114], [115] can be advantageous for drug delivery. These modification strategies involve surface PEGylation of CNTs for passivation needed for stable circulation [115] and for effective penetration into tissues [151]–[153]. Alternatively, it may be worth exploring conjugation of surface ligands to nanoparticles with the purpose of selective tumor receptor binding for specific targeting prior to laser irradiation.

Lastly, candidate nanoparticles needed to strongly absorb in the NIR. The NIR region is highly advantageous for clinical applications since NIR is weakly absorbed by tissue and can thus be focused several centimeters through tissue [62] for tumor treatment. Moreover, effective NIR absorption is necessary for rapid nanoparticle heat, expansion and vaporization in TNET.

APPENDIX A. BOUNDARY EFFECTS OF CUVETTE

To consider all the components of our *in vitro* laser-mediated system, we were interested in the effects of the cuvette on TNET. More specifically, we wanted to investigate if the rigid physical boundaries of the cuvette walls (i.e. path length) contributed to energy transfer processes during irradiation of the CB nanoparticles.

We conducted a series of preliminary studies to address the role of cuvette boundary effect in TNET. First, we compared bioeffects of samples irradiated in air (i.e. normal exposure conditions) with bioeffects of samples irradiated in a water tank. Next, we tested the effects of cuvette dimensions on TNET by exposing samples in a cuvette with a longer path length (i.e. 10 mm) compared to our standard cuvette (i.e. 2.5 mm). The compelling results from this study provide a foundation for further cuvette boundary effect studies necessary to fully understand the *in vitro* environment prior to transitioning *in vivo*.

A.1 Methods

A.1.1 Nanoparticle Prep

CB nanoparticles were prepared as previously described [14] with a stock concentration of 0.4 g/L. Dynamic light scattering measurements conducted by us revealed that the nanoparticle assembled into clusters with an effective diameter of 201.4 ± 5.5 nm (n=10) and a dispersity of 0.15 ± 0.04 nm (n=10 replicates) (ZetaSizer Nano, Malvern Instruments, Malvern, UK). Solutions were further diluted with DI water to obtain lower CB concentrations.

A.1.2 Laser system

A Nd:YAG solid-state laser (Continuum Powerlite II Plus, Continuum, San Jose, CA) was used to apply 5-9 ns pulses of 1064 nm wavelength at a frequency of 10 Hz (i.e. 10 pulses per second) to cell suspensions. Pulse fluence was varied by changing the amplifier voltage settings of the laser. The initial Super-Gaussian 12 mm wide beam was passed through an 8 mm aperture to create a pseudo-flat top profile to achieve a more homogeneous distribution of the laser energy.

A.1.3 Cell culture & in vitro exposures

Human prostate cancer cells (DU145, American Type Culture Collection, Manassas, VA, USA) were cultured as monolayers in a humidified atmosphere of 95% air and 5% CO2 at 37°C in RPMI-1640 medium (Cellgro, Herndon, VA, USA) supplemented with 100 g/mL penicillin-streptomycin (Cellgro) and 10% (v/v) heat inactivated fetal bovine serum (FBS) (Corning, Palo Alto, CA, USA). Cells were harvested at 80-90% confluence for experiments by trypsin/EDTA (Cellgro) digestion, washed with serum and then re-suspended in RPMI at a cell concentration of 10^6 cells/ml.

Cells were transferred to Pyrex glass cuvettes with a 2.5 mm path length, and in some cases a 10 mm path length for exposure. Harvested cells were transported in 1.5 ml microcentrifuge tubes and stored on ice until exposure. Exposed cuvettes contained 520 μL of cells suspended in RPMI, in addition to carbon nanoparticle solutions added at final concentrations of 3.1, 25 mg/L and 157 mg/L. High purity calcein (Molecular Probes, Eugene, OR, USA) was added as an uptake marker at a final concentration of 10 μM. Following exposure, the contents were transferred back into the microcentrifuge tubes with

a transfer pipette and stored on ice to reduce uptake due to endocytosis. To label nonviable cells post-irradiation, propidium iodide (Invitrogen, Grand Island, NY, USA) was added at a concentration of 13.5 μM and cells were incubated for 10 minutes. Samples were washed at least 3 times with phosphate buffer saline (PBS) to remove excess fluorescence from the bulk solution.

A.1.4 Analysis

A flow cytometer (BD Accuri, BD Biosciences, San Jose, CA) quantified bioeffects in terms of live cells with intracellular uptake (i.e. intact cells with green fluorescence of calcein loading and without red fluorescence of propidium iodide staining) and non-viable cells (i.e. intact cells with propidium iodide staining). Calcein fluorescence was measured with a 530/28 nm bandpass filter and propidium iodide (PI) was measured with a 670 nm longpass filter. Samples were run at a constant flow rate of 35 μL/min for 1 min.

A negative control containing cells only in RPMI was used to construct a cell population gate in the forward-scattered and side-scattered analysis. Cells within this gate were intact cells, whereas events with a lower forward-scatter and higher side-scatter signal were considered to be dead cells. To account for possible cell loss due to cell fragmentation and necrotic death, the number of PI-negative cells for each exposed sample was compared to the PI-negative cells for the sham [80].

A.2 Results

First, we evaluated effects of the acoustic field in the cuvette with a series of experiments in a water tank. Samples in the cuvette were submerged in a water tank to

minimize reflections off the glass-exterior interface usually present in normal exposure conditions (i.e. cuvette exposed in air). Samples irradiated in water showed significantly lower intracellular uptake at both 44 mJ/cm^2 and 88 mJ/cm^2 when compared to samples exposed in air (**Figure A.1**).

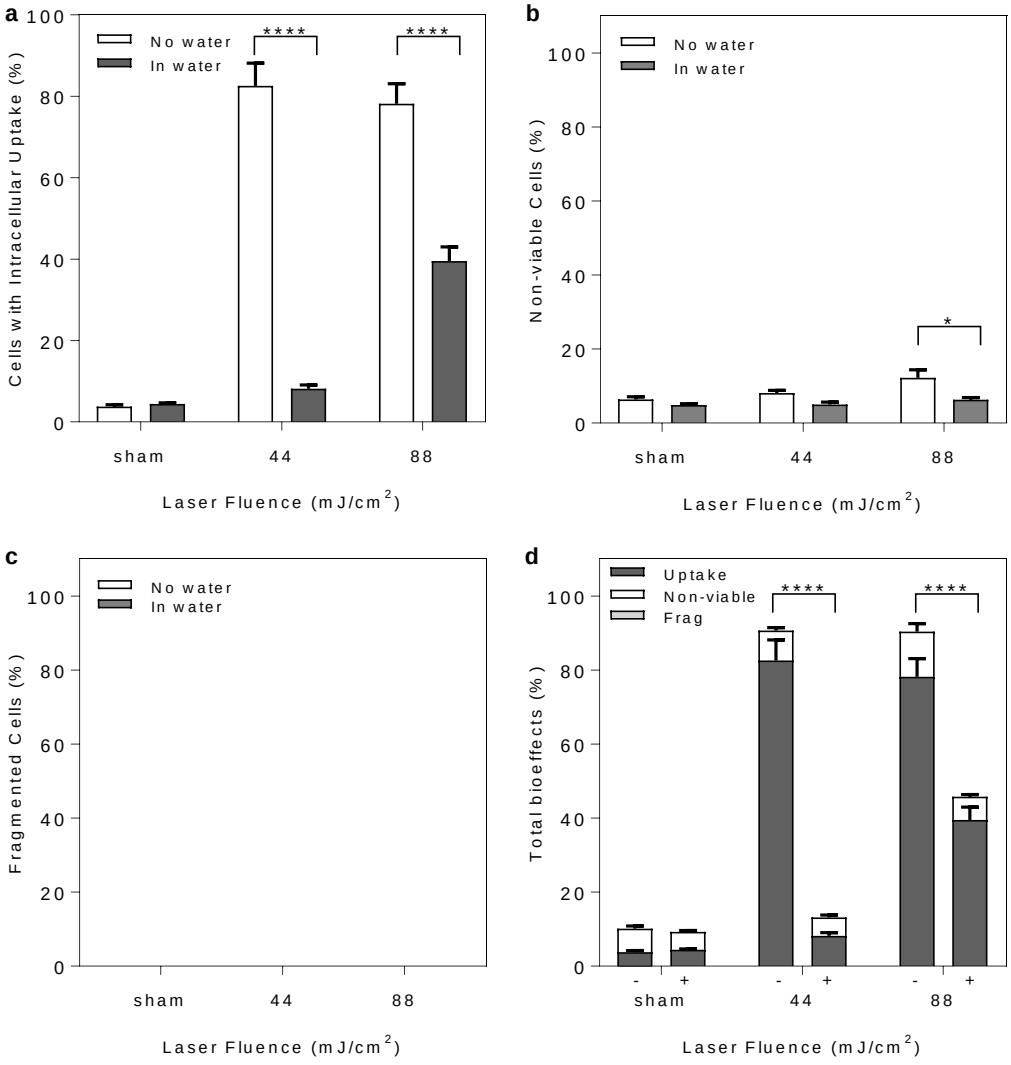

Figure A.1: Cells in cuvette exposed to 600 pulses at 44 and 88 mJ/cm^2 in air and submerged in water: a) uptake, b) non-viable cells, c) fragmented cells, and d) total bioeffects (uptake, non-viable, fragmented). Asterisks (*) indicate statistical significance (ANOVA, *p< 0.05, ****p< 0.0001). Data show average ± SD (n = 3).

The effects of the physical boundary (i.e. walls / path length) of the cuvette was also investigated. Experiments were conducted where the same front surface area of the cuvette was the same, but the thickness or the path length of the cuvette was altered from 2 mm to 10 mm (5x the initial path length). Cells, carbon black, and calcein were added to the more voluminous cuvettes (i.e. 10 mm) by scaling the volumes with the original cuvette. Samples were exposed for the shortest number of pulses which we observed bioeffects with a final CB concentration of 25 mg/L (Error! Reference source not found.).

The preliminary results indicate that intracellular uptake increased for samples exposed in the 10 mm cuvette compared to the 2.5 mm cuvette (**Figure A.2a**). There was no significant difference in viability loss (PI+ cells) between the 2.5 mm and 10 mm cuvettes (**Figure A.2b**). Cells exposed in the 10 mm did, however, exhibit significantly less fragmentation compared to the 2.5 mm cuvette (**Figure A.2c**). There was no significant difference in total bioeffects between the 2.5 mm and 10 mm cuvettes ($p = 0.9524$) (**Figure A.2d**). These initial results suggest that the physical boundary (i.e. cuvette walls) is important to TNET and moreover, supports our hypothesis that TNET is mediated by short-range, local effects.

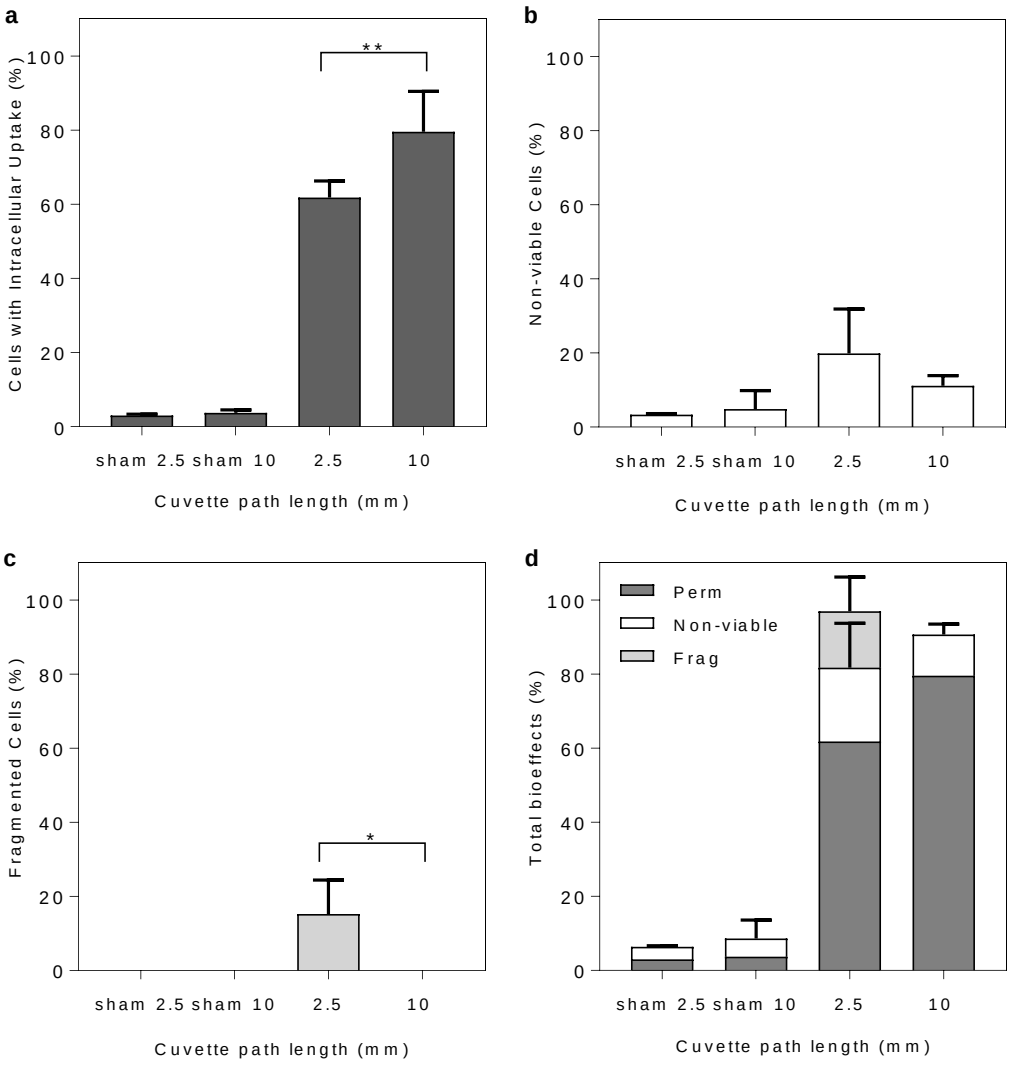

Figure A.2: Percentage of cells with a) uptake, b) non-viable, c) fragmented, and d) total bioeffects (uptake, non-viable, fragmented) after exposure to 150 pulses at 88 mJ/cm^2 with 25 mg/L CB nanoparticles with cuvette thicknesses changed from 2.5 to 10 mm. Asterisks (*) indicate statistical significance (ANOVA, *p < 0.05, **p < 0.01). Data show mean ± SD (n=3).

A.3 Conclusions

The preliminary results for the water tank and cuvette path length experiments suggest further investigation is needed to reconcile the role of the cuvette in TNET. We saw that by minimizing reflections at the glass-air interface, less bioeffects occurred. This suggests that pressure may be reverberating inside the cuvette and applies shear and/or tensile forces on cells, leading to viability loss. Additionally, the cuvette path length experiments seem to indicate that TNET is a local effect [23] limited by physical boundaries, since we saw that by increasing the path length intracellular uptake increased and fragmentation was significant reduced. Further studies to better understand these cuvette effects are highly warranted.

APPENDIX B. CALCULATIONS OF CB NANOPARTICLE HEATING, ENERGY ABSORBED AND BUBBLE SIZE

B.1 Calculating energy absorbed (Q_{in})

Using Mie scattering theory analyses from previous work [23] allows us to calculate Q_{in}. Let us calculate Q_{in} for 0.39 mg/L CB nanoparticle concentration at 44 mJ/cm^2. Mie scattering calculations were done with an online calculator [154].

Input Parameters:

Sphere Diameter = 0.025 μm

Wavelength in Vacuum = 1.064 nm

Index of Refraction of media (water) = 1.33

Carbon Refractive Index = 2-0.29i [155]

Number of Angles =100

Concentration = Number of spheres in one aggregate/ Volume of each aggregate = 31751.4 spheres/cm^3

Output Parameters:

Scattering Cross Section = 1.27 x 10^{-8} μm^2

Backscattering Cross Section = 1.90 x 10^{-8} μm^2

Extinction Cross Section = 2.1 x 10^{-5} μm^2

Total Scattering Cross Section = Scattering Cross Section + Backscattering Cross Section

$= 3.18 \times 10^{-8}\ \mu m^2$

Total Absorption = Total Extinction – Total Scattering = $2.10 \times 10^{-5}\ \mu m^2$

Number of spherules per aggregate = 133

Total absorption area in 1 aggregate = Total Number of spherules in each aggregate x Absorption by each spherule

$= 133 \times (2.10 \times 10^{-5}\ \mu m^2) = 2.79 \times 10^{-3}\ \mu m^2$

Total scattering by 1 aggregate = Total number of spherules in each aggregate^2 x Scattering by each spherule

$= 1332 \times (3.18 \times 10^{-8}\ \mu m^2) = 5.62 \times 10^{-4}\ \mu m^2$

For a 0.39 mg/L carbon solution:

Total number of spherules = 1.48×10^{10}

Total absorption by solution = Total Number of spherules x Absorption by each spherule

$= 3.10 \times 10^{-7}\ m^2$

Total scattering by solution = Total number of spherules per aggregate^2 x Scattering per spherule x Total number of aggregates = Total Number of Spherules x Total number of spherules per aggregate x Scattering per spherule = $6.25 \times 10^{-8}\ m^2$

Absorbed Energy =Total absorption area / Total area

= ((3.10 x 10^{-7} m^2) x 100)/(4 x 10^{-4} m^2) = 0.08%

Scattered Energy =Total scattering area / Total area

= ((6.25 x 10^{-8} m^2) x 100)/(4.0 x 10^{-4} m^2) = 0.016%

Energy Attenuation = Absorbed % + Scattered % = 0.093%

Total laser energy at 44 mJ/cm^2: 175 mJ

Q_{in}: (Absorbed energy (%) x Total laser energy) / 100 =0.136 mJ/shot

B.2 Calculating CB nanoparticle heating

Again, let us continue to use a 0.39 mg/L CB nanoparticle concentration exposed to a laser fluence of 44 mJ/cm^2 as an example. We will now calculate the peak particle temperature based on previous work [23].

Total mass of CB in cuvette = 0.39 mg/L x 0.563 mL = 2.19 x 10^{-7} g

Heat capacity of CB = 0.7 J/g^{o}C

Peak particle temperature = (Q_{in}) / (Total mass of CB x C_p) = 884 ^{o}C

B.3 Calculating vapor-bubble size

Now let's calculate the vapor-bubble size based on the above parameters:

Heat capacity of water = 4.184 J/g^{o}C

ΔT = (100 – 23) ^{o}C = 77 ^{o}C

$\Delta H_{vaporization}$ = 2260 kJ/mol

Moles of water produced (n) = ((Q_{in} – Total mass x $C_{pcarbon}$ x ΔT) / (C_{pwater} x ΔT + ΔHvaporization)) = 5.25 x 10^{-11} kg

Mass of water vapor per NP = Moles of water produced / Total # aggregates

= (5.25 x 10^{-11} kg) / (1.1 x 10^{8})

= 4.72 x 10^{-19} kg

Steam specific volume = 1.67 m^3/kg

Volume of vapor = Mass of water vapor per NP x Steam specific volume

= 7.88 x 10^{-19} m^3

Radius of vapor = (Volume of vapor x 0.75) / ($\pi^{1/3}$)

= 573 nm

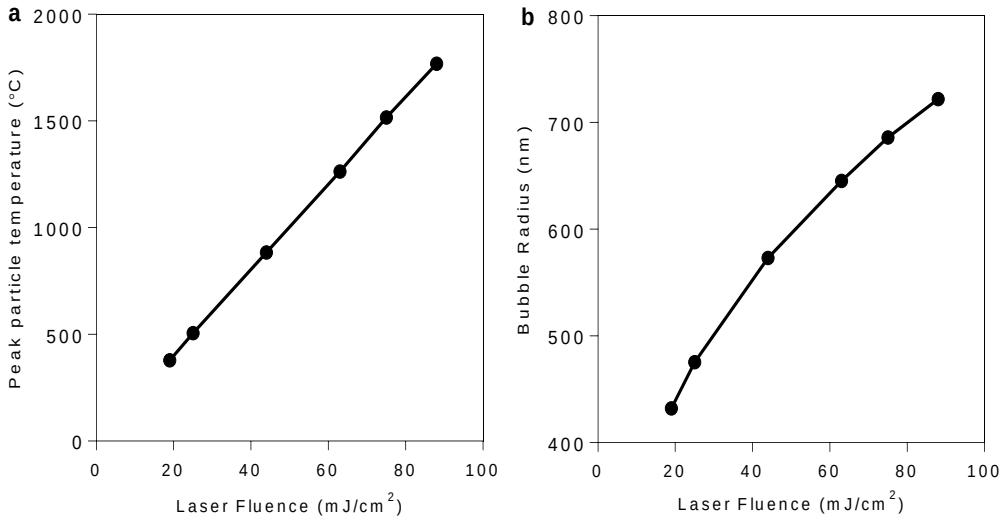

Figure B.1: a) Calculated peak particle temperature with increasing laser fluence shows a linear relationship with fluence and temperature. b) Calculated bubble size

with increasing laser fluence shows a nonlinear relationship with fluence and bubble radius.

B.3 Total energy input per cell

Table B.1: Total energy input per cell calculations for all CB nanoparticle concentrations and laser pulses tested based on Figure 4.6. Asterisks (*) indicate number of cells for a given 520 µL volume in the cuvette, based on a cell concentration of 10^6 cells/mL. Q_{in} represent the total energy absorbed for the system.

CB (mg/L)	Laser Fluence (mJ/cm^2)	Q_{in} (mJ/pulse)	# pulses	# Cells*	Total energy absorbed per cell (mJ/cell)
25	88	1.7E+01	1	5.2E+05	3.4E-05
	88	1.7E+01	10	5.2E+05	3.4E-04
	88	1.7E+01	50	5.2E+05	1.7E-03
	88	1.7E+01	150	5.2E+05	5.0E-03
	88	1.7E+01	300	5.2E+05	1.0E-02
	88	1.7E+01	600	5.2E+05	2.0E-02
	88	1.7E+01	1800	5.2E+05	6.0E-02
157	88	1.1E+02	1	5.2E+05	2.1E-04
	88	1.1E+02	10	5.2E+05	2.1E-03
	88	1.1E+02	50	5.2E+05	1.1E-02
	88	1.1E+02	150	5.2E+05	3.2E-02
	88	1.1E+02	300	5.2E+05	6.3E-02
	88	1.1E+02	600	5.2E+05	1.3E-01
	88	1.1E+02	1800	5.2E+05	3.8E-01

Table B.2: Total energy input per cell calculations for all CB nanoparticle concentrations and cell concentrations tested based on Figure 4.7. Asterisks (*) indicate number of cells for a given 520 µL volume in the cuvette, based on a cell concentration of 10^5-10^7 cells/mL. Q_{in} represent the total energy absorbed for the system.

CB (mg/L)	Laser Fluence (mJ/cm^2)	Q_{in} (mJ/pulse)	# pulses	# Cells*	Total energy absorbed per cell (mJ/cell)
0.39	88	3.3E-02	600	5.2E+04	3.8E-04
	88	3.3E-02	600	2.6E+05	7.5E-05
	88	3.3E-02	600	5.2E+05	3.8E-05
	88	3.3E-02	600	1.0E+06	1.9E-05
	88	3.3E-02	600	5.2E+06	3.8E-06
3.1	88	2.2E+00	600	5.2E+04	2.5E-02
	88	2.2E+00	600	2.6E+05	5.0E-03
	88	2.2E+00	600	5.2E+05	2.5E-03
	88	2.2E+00	600	1.0E+06	1.3E-03
	88	2.2E+00	600	5.2E+06	2.5E-04
25	88	1.7E+01	600	5.2E+04	2.0E-01
	88	1.7E+01	600	2.6E+05	4.0E-02
	88	1.7E+01	600	5.2E+05	2.0E-02
	88	1.7E+01	600	1.0E+06	1.0E-02
	88	1.7E+01	600	5.2E+06	2.0E-03

REFERENCES

[1] B. P. Timko, K. Whitehead, W. Gao, D. S. Kohane, O. Farokhzad, D. Anderson, and R. Langer, "Advances in Drug Delivery," *Annu. Rev. Mater. Res.*, vol. 41, no. 1, pp. 1–20, Aug. 2011.

[2] R. Langer, "Drug delivery and targeting.," *Nature*, vol. 392, pp. 5–10, 1998.

[3] S. Mitragotri, P. A. Burke, and R. Langer, "Overcoming the challenges in administering biopharmaceuticals: formulation and delivery strategies," *Nat. Rev. Drug Discov.*, vol. 13, no. 9, pp. 655–672, Aug. 2014.

[4] R. Langer and N. Peppas, "Advances in biomaterials, drug delivery, and bionanotechnology," *AIChE J.*, vol. 49, no. 12, 2003.

[5] D. D. Breimer, "Future challenges for drug delivery.," *J. Control. Release*, vol. 62, no. 1–2, pp. 3–6, Nov. 1999.

[6] B. Alberts, A. Johnson, J. Lewis, M. Raff, K. Roberts, and P. Walter, "Membrane Transport of Small Molecules and the Electrical Properties of Membranes." Garland Science, 2002.

[7] L. Illum, "Nasal drug delivery—possibilities, problems and solutions," *J. Control. Release*, vol. 87, no. 1–3, pp. 187–198, Feb. 2003.

[8] A. K. Varkouhi, M. Scholte, G. Storm, and H. J. Haisma, "Endosomal escape pathways for delivery of biologicals.," *J. Control. Release*, vol. 151, no. 3, pp. 220–8, May 2011.

[9] M. Kay, J. Glorioso, and L. Naldini, "Viral vectors for gene therapy: the art of turning infectious agents into vehicles of therapeutics," *Nat. Med.*, vol. 7, no. 1, pp. 33–40, 2001.

[10] X. Guo and F. Szoka, "Chemical approaches to triggerable lipid vesicles for drug and gene delivery," *Acc. Chem. Res.*, vol. 34, no. 32, pp. 335–341, Aug. 2003.

[11] N. Desai, "Challenges in Development of Nanoparticle-Based Therapeutics," *AAPS*

J., vol. 14, no. 2, pp. 282–295, Mar. 2012.

[12] W. H. De Jong, P. J. A. P. Borm, and W. De Jong, "Drug delivery and nanoparticles: applications and hazards," *Int. J. Nanomedicine*, vol. 3, no. 2, pp. 133–149, Jan. 2008.

[13] P. Chakravarty, W. Qian, M. a El-Sayed, and M. R. Prausnitz, "Delivery of molecules into cells using carbon nanoparticles activated by femtosecond laser pulses.," *Nat. Nanotechnol.*, vol. 5, no. 8, pp. 607–11, Aug. 2010.

[14] A. Sengupta, S. C. Kelly, N. Dwivedi, N. N. Thadhani, and M. R. Prausnitz, "Efficient Intracellular Delivery of Molecules with High Cell Viability Using Nanosecond-Pulsed Laser-Activated Carbon Nanoparticles," *ACS Nano*, vol. 8, no. 3, pp. 2889–2899, 2014.

[15] H. Chen and G. Diebold, "Chemical Generation of Acoustic Waves: A Giant Photoacoustic Effect," *Science (80-.).*, vol. 270, no. 5238, pp. 963–966, Nov. 1995.

[16] H. R. Guzmán, A. J. McNamara, D. X. Nguyen, and M. R. Prausnitz, "Bioeffects caused by changes in acoustic cavitation bubble density and cell concentration: a unified explanation based on cell-to-bubble ratio and blast radius," *Ultrasound Med. Biol.*, vol. 29, no. 8, pp. 1211–1222, Aug. 2003.

[17] P. Prentice, A. Cuschieri, K. Dholakia, M. Prausnitz, and P. Campbell, "Membrane disruption by optically controlled microbubble cavitation," *Nat. Phys.*, vol. 1, no. 2, pp. 107–110, Oct. 2005.

[18] D. M. Hallow, A. D. Mahajan, T. E. McCutchen, and M. R. Prausnitz, "Measurement and correlation of acoustic cavitation with cellular bioeffects.," *Ultrasound Med. Biol.*, vol. 32, no. 7, pp. 1111–22, Jul. 2006.

[19] J. D. Hutcheson, R. K. Schlicher, H. K. Hicks, and M. R. Prausnitz, "Saving cells from ultrasound-induced apoptosis: quantification of cell death and uptake following sonication and effects of targeted calcium chelation.," *Ultrasound Med. Biol.*, vol. 36, no. 6, pp. 1008–21, Jun. 2010.

[20] R. K. Schlicher, J. D. Hutcheson, H. Radhakrishna, R. P. Apkarian, and M. R. Prausnitz, "Changes in cell morphology due to plasma membrane wounding by acoustic cavitation.," *Ultrasound Med. Biol.*, vol. 36, no. 4, pp. 677–92, Apr. 2010.

[21] R. K. Schlicher, H. Radhakrishna, T. P. Tolentino, R. P. Apkarian, V. Zarnitsyn, and M. R. Prausnitz, "Mechanism of intracellular delivery by acoustic cavitation.," *Ultrasound Med. Biol.*, vol. 32, no. 6, pp. 915–24, Jun. 2006.

[22] Y. Liu, J. Yan, and M. R. Prausnitz, "Can ultrasound enable efficient intracellular uptake of molecules? A retrospective literature review and analysis.," *Ultrasound Med. Biol.*, vol. 38, no. 5, pp. 876–88, May 2012.

[23] A. Sengupta, M. Gray, S. C. Kelly, S. Y. Holguin, N. N. Thadhani, and M. R. Prausnitz, "Energy transfer mechanisms during molecular delivery to cells by laser-activated carbon nanoparticles," *Biophys. J.*, vol. 112, pp. 1258–1269, 2017.

[24] R. Langer, "Drug delivery. Drugs on target.," *Science*, vol. 293, no. 5527, pp. 58–9, Jul. 2001.

[25] V. P. Torchilin, "Recent approaches to intracellular delivery of drugs and DNA and organelle targeting.," *Annu. Rev. Biomed. Eng.*, vol. 8, pp. 343–75, Jan. 2006.

[26] A. H. Faraji and P. Wipf, "Nanoparticles in cellular drug delivery.," *Bioorg. Med. Chem.*, vol. 17, no. 8, pp. 2950–62, Apr. 2009.

[27] B. O. T. Project, "Anatomy and Physiology: The Cell Membrane," *BCcampus*. .

[28] G. Cooper, "Cell Membranes," in *The Cell: A Molecular Approach*, 2nd ed., Sunderland (MA): Sinauer Associates, 2000.

[29] B. Alberts, A. Johnson, J. Lewis, M. Raff, K. Roberts, and P. Walter, *Molecular Biology of the Cell*, 4th ed. Garland Science, 2002.

[30] L. M. B. and P. W. Swaan, "Endocytic Mechanisms for Targeted Drug Delivery," *Adv. Drug Deliv. Rev.*, vol. 59, no. 8, pp. 748–758, 2007.

[31] J. M. Meacham, K. Durvasula, F. L. Degertekin, and A. G. Fedorov, "Physical methods for intracellular delivery: practical aspects from laboratory use to industrial-scale processing.," *J. Lab. Autom.*, vol. 19, pp. 1–18, 2014.

[32] P. K. Deshmukh, K. P. Ramani, S. S. Singh, A. R. Tekade, V. K. Chatap, G. B. Patil, and S. B. Bari, "Stimuli-sensitive layer-by-layer (LbL) self-assembly systems:

targeting and biosensory applications.," *J. Control. Release*, vol. 166, no. 3, pp. 294–306, Mar. 2013.

[33] C. E. Mora-Huertas, H. Fessi, and A. Elaissari, "Polymer-based nanocapsules for drug delivery.," *Int. J. Pharm.*, vol. 385, no. 1–2, pp. 113–42, Jan. 2010.

[34] G.-Y. Liu, C.-J. Chen, and J. Ji, "Biocompatible and biodegradable polymersomes as delivery vehicles in biomedical applications," *Soft Matter*, vol. 8, no. 34, p. 8811, 2012.

[35] M. Liong, J. Lu, M. Kovochich, T. Xia, S. G. Ruehm, A. E. Nel, F. Tamanoi, and J. I. Zink, "Multifunctional inorganic nanoparticles for imaging, targeting, and drug delivery.," *ACS Nano*, vol. 2, no. 5, pp. 889–96, May 2008.

[36] A. Kumari, S. K. Yadav, and S. C. Yadav, "Biodegradable polymeric nanoparticles based drug delivery systems.," *Colloids Surf. B. Biointerfaces*, vol. 75, no. 1, pp. 1–18, Jan. 2010.

[37] T. M. Allen and P. R. Cullis, "Liposomal drug delivery systems: from concept to clinical applications.," *Adv. Drug Deliv. Rev.*, vol. 65, no. 1, pp. 36–48, Jan. 2013.

[38] P. Kesharwani, K. Jain, and N. K. Jain, "Dendrimer as nanocarrier for drug delivery," *Prog. Polym. Sci.*, vol. 39, no. 2, pp. 268–307, Feb. 2014.

[39] J.-U. a H. Junghanns and R. H. Müller, "Nanocrystal technology, drug delivery and clinical applications.," *Int. J. Nanomedicine*, vol. 3, no. 3, pp. 295–309, Jan. 2008.

[40] P. L. Felgner, T. R. Gadek, M. Holm, R. Roman, H. W. Chan, M. Wenz, J. P. Northrop, G. M. Ringold, and M. Danielsen, "Lipofection: a highly efficient, lipid-mediated DNA-transfection procedure.," *Proc. Natl. Acad. Sci. U. S. A.*, vol. 84, no. 21, pp. 7413–7417, 1987.

[41] V. L. C. Peetla, A. Stine, "Biophysical interactions with model lipid membranes: applications in drug discovery and drug delivery," *Mol Pharm.*, vol. 6, no. 5, pp. 1264–1276, 2009.

[42] D. Bouard, D. Alazard-Dany, and F.-L. Cosset, "Viral vectors: from virology to transgene expression.," *Br. J. Pharmacol.*, vol. 157, no. 2, pp. 153–65, May 2009.

[43] S. Mehier-Humbert and R. H. Guy, “Physical methods for gene transfer: improving the kinetics of gene delivery into cells.,” *Adv. Drug Deliv. Rev.*, vol. 57, no. 5, pp. 733–53, Apr. 2005.

[44] H. R. Guzmán, D. X. Nguyen, S. Khan, and M. R. Prausnitz, “Ultrasound-mediated disruption of cell membranes. II. Heterogeneous effects on cells,” *J. Acoust. Soc. Am.*, vol. 110, no. 1, p. 597, 2001.

[45] R. A. Steinhardt, “The mechanisms of cell membrane repair: A tutorial guide to key experiments.,” *Ann. N. Y. Acad. Sci.*, vol. 1066, pp. 152–165, 2005.

[46] M. L. Yarmush, A. Golberg, G. Serša, T. Kotnik, and D. Miklavčič, “Electroporation-Based Technologies for Medicine: Principles, Applications, and Challenges.,” *Annu. Rev. Biomed. Eng.*, vol. 16, pp. 295–320, 2014.

[47] J. Gehl, “Electroporation: theory and methods, perspectives for drug delivery, gene therapy and research,” *Acta Physiol. Scand.*, vol. 177, no. 4, pp. 437–47, Apr. 2003.

[48] H. R. Azencott, “Influence of the cell wall on intracellular delivery by electroporation and acoustic cavitation,” no. January, 2003.

[49] D. J. Wells, “Gene therapy progress and prospects: electroporation and other physical methods.,” *Gene Ther.*, vol. 11, no. 18, pp. 1363–9, Sep. 2004.

[50] T. Saito and N. Nakatsuji, “Efficient Gene Transfer into the Embryonic Mouse Brain Using in Vivo Electroporation,” *Dev. Biol.*, vol. 240, no. 1, pp. 237–246, 2001.

[51] I. Lentacker, I. De Cock, R. Deckers, S. C. De Smedt, and C. T. W. Moonen, “Understanding ultrasound induced sonoporation: Definitions and underlying mechanisms,” *Adv. Drug Deliv. Rev.*, vol. 72, pp. 49–64, 2014.

[52] Y. Zhang and L.-C. Yu, “Microinjection as a tool of mechanical delivery.,” *Curr. Opin. Biotechnol.*, vol. 19, no. 5, pp. 506–10, Oct. 2008.

[53] T. Dostálová and H. Jelínková, *Lasers for Medical Applications*. Elsevier, 2013.

[54] M. L. Geiges, “History of lasers in dermatology.,” *Curr. Probl. Dermatol.*, vol. 42, pp. 1–6, Jan. 2011.

[55] H. Jelínková, *Lasers for Medical Applications*. Elsevier, 2013.

[56] M. Waleed, S.-U. Hwang, J.-D. Kim, I. Shabbir, S.-M. Shin, and Y.-G. Lee, "Single-cell optoporation and transfection using femtosecond laser and optical tweezers.," *Biomed. Opt. Express*, vol. 4, no. 9, pp. 1533–47, Jan. 2013.

[57] M. Antkowiak, M. L. Torres-Mapa, D. J. Stevenson, K. Dholakia, and F. J. Gunn-Moore, "Femtosecond optical transfection of individual mammalian cells.," *Nat. Protoc.*, vol. 8, no. 6, pp. 1216–33, Jun. 2013.

[58] I. B. Clark, E. G. Hanania, J. Stevens, M. Gallina, A. Fieck, R. Brandes, B. O. Palsson, and M. R. Koller, "Optoinjection for efficient targeted delivery of a broad range of compounds and macromolecules into diverse cell types.," *J. Biomed. Opt.*, vol. 11, no. 1, p. 14034, 2014.

[59] A. G. Doukas and T. J. Flotte, "Physical characteristics and biological effects of laser-induced stress waves," *Ultrasound Med. Biol.*, vol. 22, no. 2, pp. 151–164, Jan. 1996.

[60] T. Kodama, M. R. Hamblin, and A. G. Doukas, "Cytoplasmic molecular delivery with shock waves: importance of impulse.," *Biophys. J.*, vol. 79, no. 4, pp. 1821–32, Oct. 2000.

[61] A. G. Doukas and N. Kollias, "Transdermal drug delivery with a pressure wave.," *Adv. Drug Deliv. Rev.*, vol. 56, no. 5, pp. 559–79, Mar. 2004.

[62] C. M. Cobley, J. Chen, E. C. Cho, L. V Wang, and Y. Xia, "Gold nanostructures: a class of multifunctional materials for biomedical applications.," *Chem. Soc. Rev.*, vol. 40, no. 1, pp. 44–56, Jan. 2011.

[63] S. Hashimoto, D. Werner, and T. Uwada, "Studies on the interaction of pulsed lasers with plasmonic gold nanoparticles toward light manipulation, heat management, and nanofabrication," *J. Photochem. Photobiol. C Photochem. Rev.*, vol. 13, no. 1, pp. 28–54, Mar. 2012.

[64] J. Chen, B. Wiley, Z.-Y. Li, D. Campbell, F. Saeki, H. Cang, L. Au, J. Lee, X. Li, and Y. Xia, "Gold Nanocages: Engineering Their Structure for Biomedical Applications," *Adv. Mater.*, vol. 17, no. 18, pp. 2255–2261, Sep. 2005.

[65] R. Zhang and H. Olin, “Carbon nanomaterials as drug carriers: Real time drug release investigation,” *Mater. Sci. Eng. C*, vol. 32, no. 5, pp. 1247–1252, Jul. 2012.

[66] C. Allen, A. Paquet, and M. Charlebois, “Detection method based on whispering gallery modes in microspheres floating in a solution under test,” *US Pat. App. 13/157,413*, vol. 8779389, pp. 1–17, 2011.

[67] B. Gandhi, “Reassessment of one Exemption from the Requirement of a Tolerance for Carbon Black,” 2005.

[68] H. J. Park, B. Wu, and G. J. Diebold, “Effects of exothermic chemical reaction on the photoacoustic effect from particulate suspensions.,” *J. Chem. Phys.*, vol. 134, no. 12, p. 124513, Mar. 2011.

[69] T. E. McGrath, G. J. Diebold, D. M. Bartels, and R. A. Crowell, “Laser-Initiated Chemical Reactions in Carbon Suspensions,” *J. Phys. Chem. A*, vol. 106, no. 43, pp. 10072–10078, Oct. 2002.

[70] C. Frez and G. J. Diebold, “Laser generation of gas bubbles: Photoacoustic and photothermal effects recorded in transient grating experiments.,” *J. Chem. Phys.*, vol. 129, no. 18, p. 184506, Nov. 2008.

[71] H. Jung Park and G. J. Diebold, “Generation of cavitation luminescence by laser-induced exothermic chemical reaction,” *J. Appl. Phys.*, vol. 114, no. 6, p. 64913, 2013.

[72] P. Chakravarty, C. D. Lane, T. M. Orlando, and M. R. Prausnitz, “Parameters affecting intracellular delivery of molecules using laser-activated carbon nanoparticles,” *Nanomedicine Nanotechnology, Biol. Med.*, vol. 12, no. 4, pp. 1003–1011, 2016.

[73] A. Sengupta, R. Mezencev, J. F. McDonald, and M. R. Prausnitz, “Delivery of siRNA to ovarian cancer cells using laser-activated carbon nanoparticles,” *Nanomedicine (Lond).*, vol. 10, no. 11, pp. 1775–84, 2015.

[74] C. Rotsch and M. Radmacher, “Drug-induced changes of cytoskeletal structure and mechanics in fibroblasts: an atomic force microscopy study.,” *Biophys. J.*, vol. 78, no. 1, pp. 520–35, Jan. 2000.

[75] M. Coué, S. L. Brenner, I. Spector, and E. D. Korn, “Inhibition of actin polymerization by latrunculin A,” *FEBS Lett.*, vol. 213, no. 2, pp. 316–318, Mar. 1987.

[76] N. Khatibzadeh, A. A. Spector, W. E. Brownell, and B. Anvari, “Effects of plasma membrane cholesterol level and cytoskeleton F-actin on cell protrusion mechanics.,” *PLoS One*, vol. 8, no. 2, p. e57147, Jan. 2013.

[77] H. C. Yalcin, K. M. Hallow, J. Wang, M. T. Wei, H. D. Ou-Yang, and S. N. Ghadiali, “Influence of cytoskeletal structure and mechanics on epithelial cell injury during cyclic airway reopening.,” *Am. J. Physiol. Lung Cell. Mol. Physiol.*, vol. 297, no. 5, pp. L881–L891, 2009.

[78] F. Braet, R. De Zanger, D. Jans, I. Spector, and E. Wisse, “Microfilament-disrupting agent latrunculin A induces an increased number of fenestrae in rat liver sinusoidal endothelial cells: Comparison with cytochalasin B,” *Hepatology*, vol. 24, no. 3, pp. 627–635, 1996.

[79] M. Swaroop, N. Thorne, M. S. Rao, C. P. Austin, J. C. McKew, and W. Zheng, “Evaluation of cholesterol reduction activity of methyl-β-cyclodextrin using differentiated human neurons and astrocytes.,” *J. Biomol. Screen.*, vol. 17, no. 9, pp. 1243–51, Oct. 2012.

[80] A. Sengupta, N. Dwivedi, S. C. Kelly, L. Tucci, N. N. Thadhani, and M. R. Prausnitz, “Poloxamer surfactant preserves cell viability during photoacoustic delivery of molecules into cells,” *Biotechnol. Bioeng.*, vol. 112, no. 2, pp. 405–415, 2015.

[81] L. Harvath, “Assay for filamentous actin.,” in *Methods in molecular biology (Clifton, N.J.) Immunocytochemical Methods and Protocols*, vol. 115, no. 3, L. C. Javois, Ed. Totowa, NJ: Humana Press Inc, 1999, pp. 291–8.

[82] S. V Verstraeten, G. G. Mackenzie, and P. I. Oteiza, “The plasma membrane plays a central role in cells response to mechanical stress.,” *Biochim. Biophys. Acta*, vol. 1798, no. 9, pp. 1739–49, Sep. 2010.

[83] P. Brulet and H. M. McConnell, “Lateral hapten mobility and immunochemistry of model membranes.,” *Proc. Natl. Acad. Sci. U. S. A.*, vol. 73, no. 9, pp. 2977–2981, 1976.

[84] R. A. Cooper, “Influence of increased membrane cholesterol on membrane fluidity and cell function in human red blood cells,” *J. Supramol. Struct.*, vol. 8, no. 4, pp. 413–430, 1978.

[85] R. Zidovetzki and I. Levitan, “Use of cyclodextrins to manipulate plasma membrane cholesterol content: evidence, misconceptions and control strategies.,” *Biochim. Biophys. Acta*, vol. 1768, no. 6, pp. 1311–24, Jun. 2007.

[86] S. K. Rodal, G. Skretting, O. Garred, F. Vilhardt, B. van Deurs, and K. Sandvig, “Extraction of cholesterol with methyl-beta-cyclodextrin perturbs formation of clathrin-coated endocytic vesicles.,” *Mol. Biol. Cell*, vol. 10, no. 4, pp. 961–74, Apr. 1999.

[87] P. H. Purdy, M. H. Fox, and J. K. Graham, “The fluidity of Chinese hamster ovary cell and bull sperm membranes after cholesterol addition,” *Cryobiology*, vol. 51, no. 1, pp. 102–112, 2005.

[88] S. Härtel, H. a Diehl, and F. Ojeda, “Methyl-beta-cyclodextrins and liposomes as water-soluble carriers for cholesterol incorporation into membranes and its evaluation by a microenzymatic fluorescence assay and membrane fluidity-sensitive dyes.,” *Anal. Biochem.*, vol. 258, pp. 277–284, 1998.

[89] L. Rajagopalan, J. N. Greeson, A. Xia, H. Liu, A. Sturm, R. M. Raphael, A. L. Davidson, J. S. Oghalai, F. a. Pereira, and W. E. Brownell, “Tuning of the outer hair cell motor by membrane cholesterol,” *J. Biol. Chem.*, vol. 282, no. 50, pp. 36659–36670, 2007.

[90] B. Alberts, A. Johnson, J. Lewis, M. Raff, K. Roberts, and P. Walter, *Molecular Biology of the Cell*, 4th ed. Garland Science, 2002.

[91] D. A. Fletcher and R. D. Mullins, “Cell mechanics and the cytoskeleton.,” *Nature*, vol. 463, no. 7280, pp. 485–92, 2010.

[92] X. Chen, R. S. Leow, Y. Hu, J. M. F. Wan, and A. C. H. Yu, “Single-site sonoporation disrupts actin cytoskeleton organization.,” *J. R. Soc. Interface*, vol. 11, no. 95, p. 20140071, Jun. 2014.

[93] K. Miyake, P. L. McNeil, K. Suzuki, R. Tsunoda, and N. Sugai, “An actin barrier to resealing.,” *J. Cell Sci.*, vol. 114, no. Pt 19, pp. 3487–3494, 2001.

[94] A. P. Atanassoff, H. Wolfmeier, R. Schoenauer, A. Hostettler, A. Ring, A. Draeger, and E. B. Babiychuk, "Microvesicle shedding and lysosomal repair fulfill divergent cellular needs during the repair of streptolysin O-induced plasmalemmal damage," *PLoS One*, vol. 9, no. 2, 2014.

[95] M. T. Abreu-Blanco, J. M. Verboon, and S. M. Parkhurst, "Single cell wound repair: Dealing with life's little traumas," *Bioarchitecture*, vol. 1, no. 3, pp. 114–121, 2011.

[96] R. McClean, C. MacCallum, D. Blyde, W. Holt, and S. Johnston, "Actin localisation and the effect of cytochalasin D on the osmotic tolerance of cauda epididymidal kangaroo spermatozoa," *Cryo-Letters*, vol. 27, no. 4, pp. 253–260, 2006.

[97] L. M. Fujimoto, R. Roth, J. E. Heuser, and S. L. Schmid, "Actin assembly plays a variable, but not obligatory role in receptor-mediated endocytosis in mammalian cells.," *Traffic*, vol. 1, no. 2, pp. 161–171, 2000.

[98] M. Trendowski, "Exploiting the cytoskeletal filaments of neoplastic cells to potentiate a novel therapeutic approach.," *Biochim. Biophys. Acta*, vol. 1846, no. 2, pp. 599–616, Dec. 2014.

[99] M. D. Duncan, J. W. Harmon, and L. K. Duncan, "Actin disruption inhibits bombesin stimulation of focal adhesion kinase (pp125FAK) in prostate carcinoma," *J Surg Res*, vol. 63, no. 1, pp. 359–363, 1996.

[100] F. Braet, I. Spector, R. De Zanger, and E. Wisse, "A novel structure involved in the formation of liver endothelial cell fenestrae revealed by using the actin inhibitor misakinolide.," *Proc. Natl. Acad. Sci. U. S. A.*, vol. 95, no. 23, pp. 13635–13640, 1998.

[101] M. Sun, N. Northup, F. Marga, T. Huber, F. J. Byfield, I. Levitan, and G. Forgacs, "The effect of cellular cholesterol on membrane-cytoskeleton adhesion.," *J. Cell Sci.*, vol. 120, no. Pt 13, pp. 2223–31, Jul. 2007.

[102] I. Titushkin and M. Cho, "Distinct membrane mechanical properties of human mesenchymal stem cells determined using laser optical tweezers.," *Biophys. J.*, vol. 90, no. 7, pp. 2582–91, Apr. 2006.

[103] B. Hissa, B. Pontes, P. M. S. Roma, A. P. Alves, C. D. Rocha, T. M. Valverde, P. H. N. Aguiar, F. P. Almeida, A. J. Guimarães, C. Guatimosim, A. M. Silva, M. C. Fernandes, N. W. Andrews, N. B. Viana, O. N. Mesquita, U. Agero, and L. O.

Andrade, “Membrane cholesterol removal changes mechanical properties of cells and induces secretion of a specific pool of lysosomes.,” *PLoS One*, vol. 8, no. 12, p. e82988, Jan. 2013.

[104] M. Delcea, N. Sternberg, and A. M. Yashchenok, “Nanoplasmonics for Dual Molecule Release through Nanopores in the Membrane of Red Blood Cells,” *ACS Nano*, vol. 6, no. 5, pp. 1–4, 2012.

[105] R. Xiong, S. K. Samal, J. Demeester, A. G. Skirtach, S. C. De Smedt, and K. Braeckmans, “Laser-assisted photoporation: fundamentals, technological advances and applications,” *Adv. Phys. X*, vol. 1, no. 4, pp. 596–620, 2016.

[106] T. C. Bond and R. W. Bergstrom, “Light Absorption by Carbonaceous Particles: An Investigative Review,” *Aerosol Sci. Technol.*, vol. 40, no. 1, pp. 27–67, Jan. 2006.

[107] K. Mansour and E. W. Van Stryland, “Nonlinear optical properties of carbon-black suspensions (ink),” *J. Opt. Soc. Am. B*, vol. 9, no. 7, pp. 1100–1109, 1992.

[108] Y. I. Cho and J. P. Hartnett, “Non-Newtonian Fluids in Circular Pipe Flow,” in *Advances in Heat Transfer*, 15th ed., J. P. Hartnett and T. F. Irvine, Eds. San Diego: Academic Press, 1982, p. 351.

[109] R. Sadighi-Bonabi, F. Alijan Farzad Lahiji, and F. Razeghi, “The effect of viscosity, applied frequency and driven pressure on the laser induced bubble luminescence in water–sulfuric acid mixtures,” *Phys. Lett. A*, vol. 380, no. 27–28, pp. 2219–2226, Jun. 2016.

[110] I. M. Kislyakov and C. S. Yelleswarapu, “Nonlinear scattering studies of carbon black suspensions using photoacoustic Z-scan technique,” *Appl. Phys. Lett.*, vol. 103, no. 15, p. 151104, 2013.

[111] D. Vincent, S. Petit, and S. L. S. Chin, “Optical Limiting Studies in a Carbon-Black Suspension for Subnanosecond and Subpicosecond Laser Pulses,” *Appl. Opt.*, vol. 41, no. 15, p. 2944, May 2002.

[112] I. M. Belousova, N. G. Mironova, A. G. Scobelev, and M. S. Yur’ev, “The investigation of nonlinear optical limiting by aqueous suspensions of carbon nanoparticles,” *Opt. Commun.*, vol. 235, no. 4–6, pp. 445–452, May 2004.

[113] X. Wang, T. Xia, S. A. Ntim, Z. Ji, S. George, H. Meng, H. Zhang, V. Castranova, S. Mitra, and A. E. Nel, "Quantitative techniques for assessing and controlling the dispersion and biological effects of multiwalled carbon nanotubes in mammalian tissue culture cells," *ACS Nano*, vol. 4, no. 12, pp. 7241–7252, 2010.

[114] A. Fraczek-Szczypta, E. Menaszek, T. B. Syeda, A. Misra, M. Alavijeh, J. Adu, and S. Blazewicz, "Effect of MWCNT surface and chemical modification on in vitro cellular response.," *J. Nanopart. Res.*, vol. 14, no. 10, p. 1181, Oct. 2012.

[115] A. a Bhirde, S. Patel, A. a Sousa, V. Patel, A. a Molinolo, Y. Ji, R. D. Leapman, J. S. Gutkind, and J. F. Rusling, "Distribution and clearance of PEG-single-walled carbon nanotube cancer drug delivery vehicles in mice.," *Nanomedicine (Lond).*, vol. 5, no. 10, pp. 1535–1546, 2010.

[116] P. Chakravarty, R. Marches, N. S. Zimmerman, A. D.-E. Swafford, P. Bajaj, I. H. Musselman, P. Pantano, R. K. Draper, and E. S. Vietta, "Thermal ablation of tumor cells with antibody-functionalized single-walled carbon nanotubes," *Proc. Natl. Acad. Sci.*, vol. 105, no. 25, pp. 8697–8702, 2008.

[117] N. W. S. Kam, M. O'Connell, J. a Wisdom, and H. Dai, "Carbon nanotubes as multifunctional biological transporters and near-infrared agents for selective cancer cell destruction.," *Proc. Natl. Acad. Sci. U. S. A.*, vol. 102, no. 33, pp. 11600–11605, 2005.

[118] R. Singh and S. V. Torti, "Carbon nanotubes in hyperthermia therapy," *Adv. Drug Deliv. Rev.*, vol. 65, no. 15, pp. 2045–2060, 2013.

[119] B. S. Wong, S. L. Yoong, A. Jagusiak, T. Panczyk, H. K. Ho, W. H. Ang, and G. Pastorin, "Carbon nanotubes for delivery of small molecule drugs," *Adv. Drug Deliv. Rev.*, vol. 65, no. 15, pp. 1964–2015, 2013.

[120] S. K. Vashist, D. Zheng, G. Pastorin, K. Al-Rubeaan, J. H. T. Luong, and F. S. Sheu, "Delivery of drugs and biomolecules using carbon nanotubes," *Carbon N. Y.*, vol. 49, no. 13, pp. 4077–4097, 2011.

[121] S. Peretz and O. Regev, "Carbon nanotubes as nanocarriers in medicine," *Curr. Opin. Colloid Interface Sci.*, vol. 17, no. 6, pp. 360–368, 2012.

[122] M. Foldvari and M. Bagonluri, "Carbon nanotubes as functional excipients for nanomedicines: II. Drug delivery and biocompatibility issues," *Nanomedicine*

Nanotechnology, Biol. Med., vol. 4, no. 3, pp. 183–200, 2008.

[123] T. L. Moore, J. E. Pitzer, R. Podila, X. Wang, R. L. Lewis, S. W. Grimes, J. R. Wilson, E. Skjervold, J. M. Brown, A. Rao, and F. Alexis, "Multifunctional polymer-coated carbon nanotubes for safe drug delivery," *Part. Part. Syst. Charact.*, vol. 30, no. 4, pp. 365–373, 2013.

[124] H. K. Moon, S. H. Lee, and H. C. Choi, "In vivo near-infrared mediated tumor destruction by photothermal effect of carbon nanotubes," *ACS Nano*, vol. 3, no. 11, pp. 3707–3713, 2009.

[125] X. Liu, H. Tao, K. Yang, S. Zhang, S. T. Lee, and Z. Liu, "Optimization of surface chemistry on single-walled carbon nanotubes for in vivo photothermal ablation of tumors," *Biomaterials*, vol. 32, no. 1, pp. 144–151, 2011.

[126] L. E. Kinsler, A. R. Frey, A. B. Coppens, and J. V. Sanders, *Fundamentals of Acoustics*, 4th ed. Hoboken, NJ: John Wiley & Sons, 2000.

[127] M. C. Junger and D. Feit, *Sound, Structures, and Their Interaction*, 2nd ed., vol. 82, no. 4. 1987.

[128] S. Moosavi Nejad, S. H. R. Hosseini, H. Akiyama, and K. Tachibana, "Optical observation of cell sonoporation with low intensity ultrasound.," *Biochem. Biophys. Res. Commun.*, vol. 413, no. 2, pp. 218–23, Sep. 2011.

[129] Y. Zhou, K. Yang, J. Cui, J. Y. Ye, and C. X. Deng, "Controlled permeation of cell membrane by single bubble acoustic cavitation.," *J. Control. Release*, vol. 157, no. 1, pp. 103–11, Jan. 2012.

[130] K. Koshiyama, T. Kodama, T. Yano, and S. Fujikawa, "Molecular dynamics simulation of structural changes of lipid bilayers induced by shock waves: Effects of incident angles.," *Biochim. Biophys. Acta*, vol. 1778, no. 6, pp. 1423–8, Jun. 2008.

[131] K. Koshiyama, T. Kodama, T. Yano, and S. Fujikawa, "Structural change in lipid bilayers and water penetration induced by shock waves: molecular dynamics simulations.," *Biophys. J.*, vol. 91, no. 6, pp. 2198–205, Sep. 2006.

[132] A. Choubey, M. Vedadi, K. I. Nomura, R. K. Kalia, A. Nakano, and P. Vashishta, "Poration of lipid bilayers by shock-induced nanobubble collapse," *Appl. Phys.*

Lett., vol. 98, no. 2, pp. 26–29, 2011.

[133] K. P. Santo and M. L. Berkowitz, "Shock wave interaction with a phospholipid membrane: coarse-grained computer simulations.," *J. Chem. Phys.*, vol. 140, no. 5, p. 54906, Feb. 2014.

[134] R. N. a H. Lewis and R. N. McElhaney, "Membrane lipid phase transitions and phase organization studied by Fourier transform infrared spectroscopy.," *Biochim. Biophys. Acta*, vol. 1828, no. 10, pp. 2347–58, 2013.

[135] P. Fuchs, A. Parolat, P. W. Robbins, and E. R. Bloutt, "Fluorescence polarization and viscosities of membrane lipids of 3T3 cells," *Biochemistry*, vol. 72, no. 9, pp. 3351–354, 1975.

[136] M. H. Fox and T. M. Delohery, "Membrane fluidity measured by fluorescence polarization using an EPICS V cell sorter.," *Cytometry*, vol. 8, no. 1, pp. 20–25, 1987.

[137] B. M. Stott, M. P. Vu, C. O. McLemore, M. S. Lund, E. Gibbons, T. J. Brueseke, H. a Wilson-Ashworth, and J. D. Bell, "Use of fluorescence to determine the effects of cholesterol on lipid behavior in sphingomyelin liposomes and erythrocyte membranes.," *J. Lipid Res.*, vol. 49, no. October 2015, pp. 1202–1215, 2008.

[138] M. S. Clarke and P. L. McNeil, "Syringe loading introduces macromolecules into living mammalian cell cytosol," *J. Cell Sci.*, vol. 102, no. 3, pp. 533–541, 1992.

[139] D. M. Hallow, R. A. Seeger, P. P. Kamaev, G. R. Prado, M. C. LaPlaca, and M. R. Prausnitz, "Shear-Induced Intracellular Loading of Cells with Molecules by Controlled Microfluidics," *Biotechnol. Bioeng.*, vol. 99, no. 4, pp. 846–854, 2008.

[140] K. T. Powell and J. C. Weaver, "Gel Microdroplets and Flow Cytometry: Rapid Determination of Antibody Secretion by Individual Cells within a Cell Population," *Nat. Biotechnol.*, vol. 8, pp. 330–337, 1990.

[141] A. Krueger, "New carbon materials: biological applications of functionalized nanodiamond materials.," *Chemistry*, vol. 14, no. 5, pp. 1382–90, Jan. 2008.

[142] Y. Talukdar, J. T. Rashkow, G. Lalwani, S. Kanakia, and B. Sitharaman, "The effects of graphene nanostructures on mesenchymal stem cells.," *Biomaterials*, vol.

35, no. 18, pp. 4863–77, Jun. 2014.

[143] R. Tenne, “Inorganic nanotubes and fullerene-like nanoparticles.,” *Nat. Nanotechnol.*, vol. 1, no. 2, pp. 103–11, Nov. 2006.

[144] A. Montellano, T. Da Ros, A. Bianco, and M. Prato, “Fullerene C_{60} as a multifunctional system for drug and gene delivery.,” *Nanoscale*, vol. 3, no. 10, pp. 4035–41, Oct. 2011.

[145] A. Sengupta, “INTRACELLULAR DRUG DELIVERY USING LASER ACTIVATED CARBON NANOPARTICLES,” Georgia Institute of Technology, 2014.

[146] J. Liu, M. Yu, C. Zhou, and J. Zheng, “Renal clearable inorganic nanoparticles: A new frontier of bionanotechnology,” *Mater. Today*, vol. 16, no. 12, pp. 477–486, 2013.

[147] E. Roduner, “Size matters: why nanomaterials are different,” *Chem. Soc. Rev.*, vol. 35, no. 7, p. 583, 2006.

[148] E. Blanco, H. Shen, and M. Ferrari, “Principles of nanoparticle design for overcoming biological barriers to drug delivery.,” *Nat. Biotechnol.*, vol. 33, no. 9, pp. 941–951, 2015.

[149] S. K. Smart, A. I. Cassady, G. Q. Lu, and D. J. Martin, “The biocompatibility of carbon nanotubes,” *Carbon N. Y.*, vol. 44, no. 6, pp. 1034–1047, May 2006.

[150] H. Tong, J. K. McGee, R. K. Saxena, U. P. Kodavanti, R. B. Devlin, and M. I. Gilmour, “Influence of acid functionalization on the cardiopulmonary toxicity of carbon nanotubes and carbon black particles in mice.,” *Toxicol. Appl. Pharmacol.*, vol. 239, no. 3, pp. 224–32, Sep. 2009.

[151] S. K. Lai, Y. Y. Wang, and J. Hanes, “Mucus-penetrating nanoparticles for drug and gene delivery to mucosal tissues,” *Adv. Drug Deliv. Rev.*, vol. 61, no. 2, pp. 158–171, 2009.

[152] E. a Nance, G. F. Woodworth, K. a Sailor, T.-Y. Shih, Q. Xu, G. Swaminathan, D. Xiang, C. Eberhart, and J. Hanes, “A dense poly(ethylene glycol) coating improves penetration of large polymeric nanoparticles within brain tissue.,” *Sci. Transl. Med.*,

vol. 4, no. 149, p. 149ra119, 2012.

[153] L. M. Ensign, C. Schneider, J. S. Suk, R. Cone, and J. Hanes, "Mucus penetrating nanoparticles: Biophysical tool and method of drug and gene delivery," *Adv. Mater.*, vol. 24, no. 28, pp. 3887–3894, 2012.

[154] S. Prahl, "Mie Scattering Calculator. Version 2-3-3," *Oregon Medical Laser Center.* [Online]. Available: http://omlc.org/calc/mie_calc.html.

[155] A. Grigonis, Z. Rutkuniene, and V. Vinciunaite, "Different wavelength laser irradiation of amorphous carbon," *Acta Phys. Pol. A*, vol. 120, no. 1, pp. 26–29, 2011.